

Stability of Flows Over Stretching Surfaces

Niall Hanevy
Doctor of Philosophy

Aston University
September 2024

©Niall Hanevy, 2024

Niall Hanevy asserts their moral right to be identified as the author of this thesis

This copy of the thesis has been supplied on condition that anyone who consults it is understood to recognise that its copyright belongs to its author and that no quotation from the thesis and no information derived from it may be published without appropriate permission or acknowledgement.

Abstract

Extrusion flows are common in industry and have received considerable attention in the literature. Work in this area began with the experimental results of Trouton [111], who developed an empirical formula relating the applied tension to the stretching rate. Trouton's model has since been validated by numerous authors through the application of asymptotic arguments based on small thickness-to-length ratios in the sheet (or fibre) being drawn ([51],[84],[75],[98]).

In addition to the work on modelling the drawn sheet or fibre, the boundary layers induced by such flows have also been extensively studied. A notable early contribution is the work of Crane [23], who found exact analytical solutions of the steady Navier-Stokes equations under the assumptions of a flat sheet undergoing a linear rate of stretching. Until recently, Crane's flow has been thought to be linearly stable. However, recent analysis by Griffiths *et al.* [39] shows that this flow is actually susceptible to travelling wave instabilities in the form of Tollmien-Schlichting (TS) waves, possibly leading to defects in industrial extrusion processes.

Despite these advances, a significant gap remains between the models used to describe the induced boundary layer and the physics of the underlying industrial extrusion processes. In this thesis, we address several of these issues by independently accounting for large temperature gradients and the curvature of the sheet. We demonstrate that failing to incorporate these additional physical effects leads to poor quantitative descriptions of the basic flow profiles in the boundary layer.

We also explore the implications of temperature dependence on flow stability, using a highly accurate numerical spectral method and complementary large Reynolds number asymptotic analysis. Additionally, we show that in the isothermal case, non-modal instability mechanisms present a more likely transition scenario, with significant energy amplification occurring at Reynolds numbers that are orders of magnitude smaller than the critical values reported in [39]. This was achieved using an adjoint based power iteration method, first introduced by Corbett and Bottaro [22].

Preliminary numerical investigations using the parabolised stability equations (PSE) indicate that non-parallel effects are destabilising in the isothermal case. While we have not performed a full parametric analysis to account for non-parallel effects in Crane's flow, such an approach could be readily adapted to model the stability of our new basic flow solutions that account for the curvature of the sheet.

Contents

Abstract	i
Table of contents	ii
List of Figures	vi
1 Introduction	1
1.1 Motivation	1
1.2 Basic Flow Solutions	3
1.3 Flow Stability	5
1.4 Thesis Outline	6
2 Problem Formulation	9
2.1 Motivation	9
2.2 General Formulation	10
2.2.1 Temperature Dependence	11
2.2.2 Surface Deformation	12
3 Basic Flow Solutions	16
N.Hanevy, PhD Thesis, Aston University 2024	ii

3.1	Introduction	16
3.2	Temperature Dependence	18
3.2.1	Similarity Solutions	18
3.2.2	Constant Viscosity, No Dissipation	19
3.2.3	Viscothermal Flow	20
3.3	Deforming Sheet	28
3.3.1	Self-similar Flows	29
3.3.2	Numerical Validation	37
3.4	Discussion and Conclusions	39
4	Numerical LSA	42
4.1	Introduction	42
4.2	Numerical Formulation	44
4.2.1	Numerical Linear Disturbance Equations	44
4.3	Energy Analysis	49
4.4	Orr-Sommerfeld Comparison	54
4.4.1	Orr-Sommerfeld Formulation	55
4.4.2	Nektar++	56
4.5	Discussions and Conclusions	57
5	Asymptotic LSA	62
5.1	Introduction	62
5.2	Asymptotic Analysis	64
5.2.1	Derivation of the Scaling on the Lower Branch	64

5.2.2	Triple Deck Structure	67
5.3	Discussions and Conclusions	79
6	Non Modal Stability	81
6.1	Introduction	81
6.2	Isothermal Stretching Sheet	83
6.3	Non-Model Analysis	86
6.3.1	Derivation of the Adjoint	87
6.3.2	Numerical Scheme	89
6.4	Numerical Results	91
6.4.1	Validation	91
6.4.2	Crane OSSQ	92
6.4.3	Crane EST	95
6.5	Discussion and Conclusions	97
7	Summary of Results	100
8	Future Works	105
8.1	Alternative Flow Stability Approaches	105
8.1.1	BiGlobal	106
8.1.2	PSE	107
8.1.3	Absolute Instability	109
8.1.4	Görtler Vortices	113
8.2	The Coupled Sheet Fluid Problem	115

Bibliography	118
A Numerical Validation of Basic Flow Solutions	127
A.1 Crane's Flow	127
A.1.1 Shooting Scheme	127
A.1.2 Keller-Box Method	129
A.1.3 TDMA Scheme	134
B Derivation of Deforming Boundary Layer Solutions	136
B.1 Self-similar solutions in the limit as $c_i \rightarrow 0$	136
B.2 Derivation of the exact solutions	138
C Numerical Solution of Linear Disturbance Equation	140
C.1 Chebychev Spectral Scheme	140
D PSE	143

List of Figures

- 1.1 Industrial examples of stretching surface flows. In a) we have a Schematic of the glass sheet redraw process, reproduced with permission from O’Kiely [82] and b) is a simple schematic of polymer extrusion. This thesis aims to more accurately model the flow induced by the production of these thin sheets of glass and plastic. 2
- 1.2 Schematic of the flow induced by a two-dimensional stretching sheet. The flow of the outer fluid is driven by the shape s and stretching velocity U_w of the sheet. . 4
- 3.1 Comparison of numerical and analytical solutions of Crane’s problem for the case of constant viscosity, with $Pr = 1$. a) shows u , b) shows v , c) shows T and d) shows the difference between the numerical and analytical solutions. Note that the pressure was omitted as it is a derived quantity and does not effect the performance of our numerical scheme. 21
- 3.2 Numerical Solution of Crane’s problem (3.2) for the inverse viscosity distribution μ_1 for a range of values of the sensitivity parameter m_1 from -0.4 to 0.4 in steps of 0.2 22
- 3.3 Numerical Solution of Crane’s problem (3.2) comparing inverse and exponential viscosity distributions μ_1 and μ_2 for $m_1 = -0.75$, $m_2 = -1.06437$. a) shows the difference in the streamwise velocity, b) the wall normal velocity, c) the pressure and d) the temperature profiles. 23
- 3.4 Numerical Solution of the Crane’s Problem (3.2) for a range of x values for $Ec = 0.01$ using a pseudo similarity approach whereby $Ec x^2$ is treated as a parameter and the boundary layer equations are solved at different x locations. 25

- 3.5 Absolute value of the difference between our numerical and approximate, near wall stream wise velocity solutions in a) and b) the absolute value of the errors for the wall shear stress and boundary layer thickness 26
- 3.6 KellerBox solution at different streamwise locations compared to the self similar solution in the nondissipative regime, $Ec = 0$, $m = -0.4$. a) Shows the streamwise solutions scaled by the sheets' speed, b) the wall normal and c) the temperature profiles. 27
- 3.7 a) The difference between the shear at the wall predicted by the Keller-Box and psuedo similarity solutions and b) The overestimation of viscothermal heating for $Ec = 0.01$, $m = 0$ of the similarity solutions. The subscripts FD, SH, and KB denote the finite difference, shooting (pseudo-similarity), and Keller box results respectively. 28
- 3.8 Plots of the streamwise and wall-normal velocity components for the case when $\gamma = 2$ and $U_w = \sqrt{0U_w^2 + 2\xi/3} = \sigma$. In this case both u_0 and v_0 are independent of ξ . Given that no exact analytical solution for \hat{f} exists in the case when $\gamma = 2$, a shooting method that makes use of a fourth-order Runge-Kutta integrator, twinned with a secant root finding scheme, was employed to solve (3.17). As part of this solution process we determine that $\hat{f}''_{ZZ}(Z = 0) \approx 0.8300$, and that $\hat{f}(Z \rightarrow \infty) = \hat{f}_\infty \approx 1.0625$. In the limit as $Z \rightarrow \infty$, then $v_0 \rightarrow -\sqrt{2/3}\hat{f}_\infty$ 31
- 3.9 In (a) the wall velocity U_w , the approximate wall velocity $U_w^{\text{approx}} = \xi + 0.2260$, and the exponentially thinning sheet profile: $s(\xi) = e^{-\xi}$, are plotted against ξ . In (b) the wall velocity, given an identical thinning sheet profile, is plotted for a range of γ values. In both plots the dashed black line corresponds to the wall velocity result for a sheet undergoing linear stretching. 33
- 3.10 Plots of the streamwise (a), and wall-normal (b), velocity components for a range of ξ values. In this case the sheet is thinning exponentially: $s(\xi) = e^{-\xi}$. Crane's flat plate solutions are given by the dashed black curves. 34
- 3.11 In (a) the wall velocity U_w , the approximate wall velocity $U_w^{\text{approx}} = (\xi + 1.1819)^{-\frac{1}{3}}$, and the logarithmically thickening sheet profile: $s(\xi) = \ln(e + \xi)$, are plotted against ξ . In (b) & (c), respectively, solutions for the streamwise velocity u_0 , and wall-normal velocity $v_0 + s'_\xi u_0$, are mapped back to the unscaled boundary-layer coordinate system $(\xi, \eta + s)$. The solid black line indicates the surface of the thickening decelerating sheet. 35

3.12 In (a) we plot the absolute value of the difference between the numerical solutions for the streamwise velocity component at $\xi = 2.5$, with the corresponding boundary-layer solution at the same point, for a range of values of the small parameter $Re^{-1/2}$. In (b) we plot an identical comparison for the wall-normal velocity component. 38

3.13 Comparison between the finite element and boundary-layer solutions across the computational domain for (a) $Re^{-1/2} = 0.05$, and (b) $Re^{-1/2} = 0.04$. The same colourbar scale is used in both instances so that the reduction in error may be easily observed. 40

4.1 a) Neutral stability curve plotted against the frequency ω and b) the corresponding plot for the real part of the streamwise wavenumber α , for a range of values of the sensitivity parameter m . In c) the variation of the critical Reynolds number with m is shown. The shaded region indicates the range of values of m for which the flow is stabilised. d) shows the growth rates for each value of m at $R_{crit} + 5000$. 48

4.2 Plots of the eigenfunctions of (4.5), evaluated at $R = R_{crit} + 5000$ and $\min(\alpha_i)$. Each of the eigenfunctions have been scaled such that $\max |Q|_{m=0} = 1$, where $Q = \mathbf{Q} = (u, v, T, p)^T$ 52

4.3 a) Plots of the energy contributions for each of the integrals on the right hand side of in equation (4.8). In b) we separate the energy dissipation due to viscosity term III_a into Newtonian and temperature dependent contributions. 53

4.4 Plots derivative of I and II_a with respect to m . From the inset we see that the increase in EPRS occurs before the corresponding increase in EDV, causing the flow to be destabilised for $m > 0.34$ 54

4.5 Comparison of the frequency and growth rates in b) calculated along the red curve marked on the neutral stability curve in a), for the isothermal stretching sheet. c) shows the corresponding plot of wavenumber versus temporal growth rate. . . 58

4.6 Two dimensional structure of the dominant TS eigenmodes for the streamwise, wall normal and pressure perturbations for $\alpha = 0.14$ and $Re = 10^4$, computed using Nektar++. 59

5.1	Plot of $\ln(1-\omega/\alpha)$ against $\ln R$. The numerical solutions are the neutral solutions along the lower branch. These compared to a fitted line $y = mx + c$, with slope $m = -0.25$ and intercept $c \approx 1$	67
5.2	Schematic depicting the triple deck scaling used for the asymptotic analysis, with small parameter $\epsilon = R^{-1/8}$. Note that this Figure is not to scale.	68
5.3	Comparison of the asymptotic prediction (5.22) and the numerical solution of (4.5) of the neutral curves for different values of the sensitivity parameter m . In $m = -0.4, -0.2, 0.2$ and 0.4 in a), b), c) and d) respectively.	78
6.1	Maximum optimum for the Blasius boundary layer for $R_\theta = 166, \beta_\theta = 0.25144$. Initial conditions a) & b) and final perturbations c) & d). Note the wall normal coordinate is scaled such that $Y = y/\theta$	93
6.2	Quiver plot of the wall-normal and spanwise optimum perturbation for Crane's flow at $R = 500$, with colours indicating the magnitude of the streamwise velocity component. Scalings correspond to those in Figure 6.1, with different colour schemes used to indicate the different scalings used at the initial and final times. a) The initial condition and b) the maximum optimum evaluated at $t = t_\Gamma$	95
6.3	Local optima of the OSSQ a) and EST b) systems determined via power iteration for different time intervals. In both instances we fix $R = 200, \beta = 0.51$ and $\alpha=0$	96
6.4	Maximum optima for different Reynolds numbers for a) OSSQ and b) EST. Parameter values correspond to those reported in table 6.2.	97
8.1	Comparison of local and PSE results for the isothermal stretching sheet. The scheme is initialised using the eigenfunctions calculated from the spatial modal analysis for $R = 48499.1, \omega = 0.1364$	109
8.2	Schematic depicting the impulse response of a) convective and b) absolute instabilities in an $x-t$ -plane diagram.	111
8.3	Diagram illustrating Briggs' method for locating absolute instabilities in the rotating disk. In each plot the direction of the markers indicate the direction of the evolution branch for increases in the real part of the spanwise wavenumber and frequency.	112

8.4 Schematic illustrating combinations of base flows and surface curvatures to induce centrifugal instabilities. According to the Rayleigh circulation criterion a) and d) are stable, whereas b) and c) are unstable. This Figure is reproduced from the review of Saric *et al.* [95]. 114

A.1 Diagram outlining how the Keller-Box scheme is discretised. 130

Chapter 1

Introduction

1.1 Motivation

Throughout this thesis we will analyse flows induced by the motion of stretching surfaces. Such flows are commonplace in industry for a range of different materials, with two primary examples being polymer extrusion and glass sheet drawing. In polymer extrusion plastic resin is placed in a heated barrel known as an extruder where it is heated and melts. The extruder contains a rotating screw which pumps the molten polymer through a wide ($\sim 1 - 10$ m), narrow (~ 1 mm) slit called a die which determines the shape of the final product which typically has a large aspect ratio. Upon exiting the die, the molten polymer rapidly cools, and uniform cooling is essential to prevent deformities. This is accomplished by winding the sheet around a series of cooled rollers, which can also be used to control the final dimensions of the polymer by adjusting their respective speeds. Furthermore, these rollers serve to apply a finish to the sheet, as the polymer is often soft enough upon exiting the die to mirror the surface of the rollers, which can have both aesthetic and functional purposes. The surface's roughness can be controlled by using different grades and patterns of roughness on the rollers, as illustrated in Figure 1.1. Coextrusion is an extension of this process where multi-layered films are drawn simultaneously allowing desirable traits of the constituent polymers to be combined. This can both enhance structural properties and reduce manufacturing costs. The ultimate use of the finished product depends on its gauge with thinner sheets being thermoformed for use in packaging and thicker sheets often used as protective layer or liner for the storage and transportation of goods. A similar type of extrusion is evident in glass sheet drawing, where molten glass is fed through a die, falling under the influence of gravity onto a sequence of rollers where it is stretched as it cools and solidifies. Different approaches are sometimes taken based on the thickness or properties of the required glass. For instance, float glass is used in manufacturing plate glass for doors and windows. This process involves floating a thin sheet of molten glass on a bed of denser molten tin. The glass

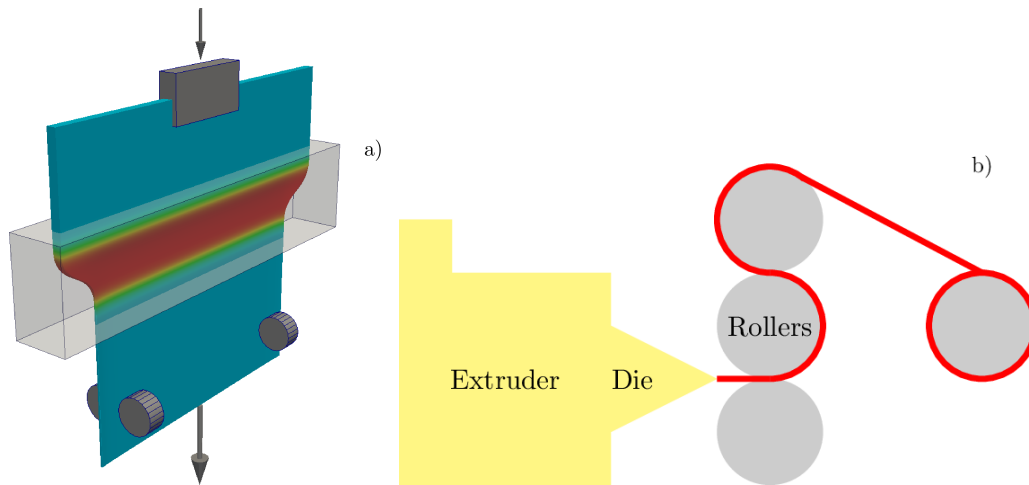


Figure 1.1: Industrial examples of stretching surface flows. In a) we have a Schematic of the glass sheet redraw process, reproduced with permission from O’Kiely [82] and b) is a simple schematic of polymer extrusion. This thesis aims to more accurately model the flow induced by the production of these thin sheets of glass and plastic.

then spreads due to gravity until it reaches an equilibrium thickness of $\sim 5\text{mm}$ when surface tension balances with the force of gravity. Further thickness reduction is achieved by stretching the glass using rollers, resulting in smooth, transparent sheets that can be bent after production for use in windshields and curved mirrors. Alternatively, the glass can be redrawn to produce longer, thinner sheets used in applications such as fingerprint sensors and mobile phone screens. This involves feeding the plate glass, now referred to as a preform, into a furnace, where the glass is stretched via the application of a uniform axial tension at a fixed distance downstream, as depicted in Figure 1.1.

Fibre drawing is a process where a cylindrical material is stretched in the axial direction to create a longer, thinner cylinder of material. In industry, this process is employed to produce glass fibre optic cables used in telecommunications and nylon or terylene fibres for textiles. The process follows a similar fashion to sheet extrusion or glass sheet redraw, as discussed earlier, with the primary difference lying in the geometry of the die and preform. These processes can be adapted to produce holey fibres with internal air pressure, often used to control the structure of the fibre. They are constructed by stacking multiple preforms together or by drilling holes in a preform, leading to the creation of complex structures with a range of applications. For example in Martelli *et al.* [74], it is found that fractal fibre optic cables significantly reduce signal loss when travelling around a bend.

The majority of studies in the literature consider either the dynamics of the sheet or fibre, or on simplified models for the flow of the ambient fluid which is driven by the motion of the sheet. In the remainder of this Chapter we will briefly highlight some results relevant to the analyses

which follows before outlining the contents of each Chapter in the remainder of this thesis.

1.2 Basic Flow Solutions

The drawing of a thin sheet or fibre is an example of an extensional flow problem. Analysis of these flows dates back to the experimental work of Trouton [111], where an empirical formula was derived for the stretching of viscous fibre using a tensile force. This Trouton model estimates both the velocity and thickness of the sheet/fibre. This work has since been extended by numerous authors. Asymptotic analyses of such flows is predicated on the assumption of small thickness to length scales for both sheets, as seen in Howell [51], and fibres, as explored by Matovich and Pearson [75] and Schultz and Davis [98]. In the isothermal viscous case this leads to a reduced system of governing equations, in which simple analytic approximations can be attained at leading order. It is found that the velocity in the direction of drawing is independent of the vertical y -coordinate in sheets and the radial coordinate for fibres. The implications of this for the induced boundary layer is depicted in Figure 1.2. Matovich and Pearson [75] considered the effects of inertia, gravity and surface tension in their analysis of the steady state drawing of an isothermal, axisymmetric viscous fibre obtaining leading order solutions. Schultz and Davis [98] proposed corrections to the leading order solutions of order aspect ratio squared. However, recent analysis by Hanevy and O’Kiely [44] suggests that the size of the correction terms depends on whether stress or plug boundary conditions are imposed at the ends of the fibre. Given that a materials properties such as viscosity in glass are highly temperature dependent, further investigations have sought to explain the effect of temperature in the drawing process. In Taroni *et al.* [103] conduction, convection and radiative heating are incorporated within their model allowing for analytic solutions in limiting cases of the relevant dimensionless parameters. This enables the authors to predict the observed characteristics of the flow profile such as the sharp reduction in fibre thickness and the temperature profile within the fibre.

Similarly, extensive work has been carried out to model the drawing of thin sheets in various industrial contexts. A model for the drawing of two-dimensional, viscous sheets in the absence of inertial forces was developed in Buckmaster *et al.* [13]. This model enabled the authors to predict the stretching of a sheet under tension, as well as the straightening and buckling of slightly curved sheets under tension and compression, respectively. In Howell [50], it was observed that this model broke down when inertia was introduced, even for small values of the sheet Reynolds number. However, this issue was addressed by introducing new length and time scales, resulting in a well-posed problem. Sheets, unlike fibres, do not maintain their shape during the drawing process. O’Kiely *et al.* [84] demonstrated that edge thickening occurs, where an initially rectangular sheet is redrawn to a nonuniform sheet which is thinner near the centre

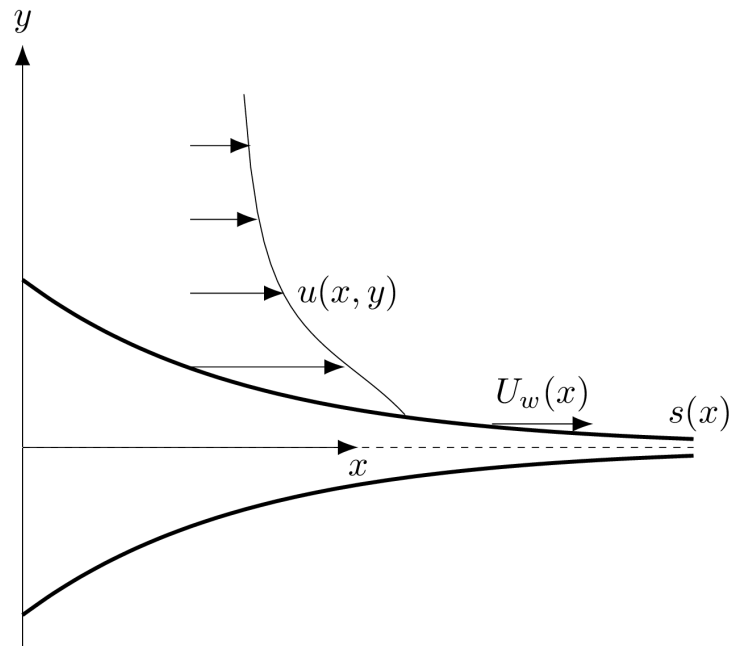


Figure 1.2: Schematic of the flow induced by a two-dimensional stretching sheet. The flow of the outer fluid is driven by the shape s and stretching velocity U_w of the sheet.

and thicker at the edges. Corrections to the leading-order solution previously obtained account for this behaviour and provide a means to model the production of thin glass sheets with as uniform a cross-section as possible. Surface tension was found to have a quantitative effect on the edge-thickening behaviour and was also included in the model.

Boundary layer theory has provided insight into the flow induced by the motion of stretching sheets. However, many of the studies in the literature treat the sheet as a flat solid object and prescribe the velocity within the sheet as a function of position in the streamwise direction. The first study of this type was that of Sakiadis [94], in which similarity solutions for viscous flow over a flat surface of constant velocity were discovered. This analysis has been extended and modified by numerous authors to incorporate different velocity profiles at the surface of the sheet. For example, in Vlegaar [114] a power law type sheet velocity was imposed and Magyari and Keller [72] used an exponential sheet velocity profile. Other authors have considered non-Newtonian effects such as Rajagopal *et al.* [89] which studied the flow of a power law fluid and Chakrabarti and Gupta [20] considered magnetohydrodynamic effects. Later in this thesis we will expand upon the analysis of Crane [23] who investigated the flow over a flat sheet with velocity proportional to distance along the stretching axis, and found an exact analytical solution to the full Navier Stokes equations.

In an analogous study Crane [24] models the flow induced by the linear stretching of a fibre whose radius decreases in the streamwise direction. The fibre's dynamics are determined using

a conservation of mass argument, enabling the discovery of similarity solutions that remain valid at large axial distances from the inlet. While this accounts for the deformation observed in industrial processes, it overlooks the dynamics of the fibre itself. In Al-Housseiny and Stone [2] an attempt is made to couple the dynamics of both the sheet and ambient fluid for viscous and elastic sheets. While the problem is not non-dimensionalised, it is assumed that both the sheet's thickness varies slowly and the velocity within the sheet is independent of the vertical y -coordinate. These assumptions allow the authors to couple the respective momentum equations. While they obtain similarity solutions that match the velocities at the interface, the stresses at the free surface do not align. Moreover, the velocity profiles within the sheet deviate from those obtained using the Trouton model in the Newtonian case. Although we have been unable to modify the analysis to address these shortcomings, as using Trouton's solutions for the sheet still result in a stress discontinuity, a proper asymptotic expansion may enable the derivation of higher-order correction terms to match the stresses in each fluid. This topic is discussed further in Chapter 8 and likely involves the introduction of a thin layer near the surface of the sheet whose thickness equals to viscosity ratio between the sheet and boundary layer to match the stresses in the respective fluid mediums.

Brady and Acrivos [11] examined the flow of a viscous fluid inside a tube and channel with linearly stretching walls, and they discovered exact similarity solutions to the Navier-Stokes equations. The primary difference in their analysis is the presence of an axial pressure gradient. The authors identify multiple solutions for different ranges of the Reynolds number and axial pressure gradient, applicable to both tubes and channels. Some of these solutions exhibit intriguing behaviour, such as flow reversal, where the sign of the streamwise velocity component changes as one moves from the core to the surface of the tube or channel.

Despite the limitations of some studies in this Section, they will serve as a foundation for us develop improved basic solutions in future Chapters which take both the deformation of the sheet and influence of temperature on the viscothermal behaviour of the ambient fluid. This in turn should yield results which are more relevant to the underlying industrial processes.

1.3 Flow Stability

Both fibres and sheets are susceptible to draw resonance, which manifests as a periodic variation in the cross-sectional thickness of a sheet or fibre. Draw resonance occurs when the ratio of inlet and outlet velocities exceeds a critical threshold, known as the draw ratio. Pearson and Matovich [87] predicted this ratio to be approximately 20.2 for a long, thin viscous fibre in the absence of inertia, surface tension and gravity. Subsequent work has extended these predictions to include the effects of temperature variation. In Shah and Pearson [99] the cooling of a fibre as it is being drawn was found to increase the draw ratio required to induce the instability. Additionally,

Myers [80] demonstrated that radiative heat transfer between the fibre and the furnace also acts to stabilise the flow. More recently, Scheid *et al.* [96] conducted an analysis of the stability of coupled temperature and fluid flow in the drawdown of viscous sheets. Qualitatively different behaviours are observed in regimes dominated by advection and heat transfer. Cooling is found to be stabilizing in advective regimes, whereas when the heat transfer coefficient is sufficiently large, the critical draw ratio is reduced. However, such high values of the heat transfer coefficient are not typically observed in industrial settings, which partly explains why draw resonance is not commonly observed in industry despite draw ratios in the range of 20 – 100 being common.

Less is known about the stability of the ambient fluid in such regimes and its impact on the sheet or fibre during drawing. This lack of knowledge is partly due to the difficulty in coupling the flow in the sheet/fibre and the surrounding fluid. One approach has been to take simplified models, such as Crane’s flow, discussed earlier, and examine its linear stability. In Bhattacharyya and Gupta [7], Crane’s flow was found to be stable to infinitesimal periodic perturbations normal to the stretching surface (Görtler disturbances). While the authors acknowledged that the flow may be unstable to other types of disturbances, it was not until Griffiths *et al.* (2021) that the flow was found to be unstable to travelling wave disturbances (Tollmien–Schlichting waves). However, incorporating curvature, interfacial, and additional physical effects may give rise to previously unconsidered instabilities. This is the central question which shapes the analysis that follows.

1.4 Thesis Outline

The main objective of this thesis is to revise the models presented in this Chapter to more accurately model flows induced by stretching surfaces and examine their stability using a combination of numerical and asymptotic approaches. This will enable the implementation of control flow techniques to suppress the onset of these instabilities and prevent defects from forming in an industrial setting.

In Chapter 2, we introduce two such new formulations. The first being the imposition of a temperature gradient between the sheet and the free stream, where the energy and momentum equations are coupled via a temperature-dependent viscosity. The stretching sheet is fixed at a temperature greater than that of the free stream. While this neglects streamwise variations in temperature, it is consistent with the local linear analysis in Griffiths *et al.* [39], allowing us to quantify temperature effects by comparison. In this formulation we are also assuming the sheet is flat and stretched at a rate proportional to the distance from the inlet. As such this assumption, according to Vlegaar [114], is valid only with about half a meter from the inlet, provided of course the magnitude of the reduction of cross-sectional thickness remains small. Beyond this point significant cooling occurs at a rate which increases as the sheet accelerates

further. This does not contradict the predictions of the Trouton model which state that the sheet accelerates exponentially, rather it can be thought of as a near inlet expansion of the sheet velocity profile.

The second novel formulation enables the modelling of flows induced by deforming surfaces. This approach is warranted in situations where the reduction in thickness of the sheet is proportional to the boundary layer length scale so that our flat sheet assumption is no longer applicable. In addition, this formulation has the added advantage of being able to describe a greater proportion of the drawing region. It would be straightforward to impose a temperature gradient between the sheet and the freestream with either a fixed sheet temperature or a sheet temperature which decreases as the sheet moves downstream. However, here our goal is to quantify the errors incurred from neglecting the curvature of the sheet. This is readily accomplished by focusing on the isothermal case and treating the sheet as a boundary condition, similar to the approach in Crane [23], with its velocity and shape prescribed in a manner that permits the existence of self-similar solutions. In both cases, self-similarity implies that the downstream basic flow solutions are scaled by the velocity of the sheet under some suitable transformation of the associated boundary layer equations. These are referred to as self-similar solutions of the first kind.

Basic flow solutions for the two new cases are presented in Chapter 3. For both the temperature dependent and deforming extension of Crane's problem we show that self similar solutions may be obtained. For the flat, heated sheet, this involves the numerical solution of an ordinary differential boundary layer equation, although near wall, weakly temperature-dependent, analytical solutions are also presented. These are validated by the numerical solution of the parabolic, boundary layer PDE's using a Keller-Box scheme where excellent agreement is found. In the deforming case we demonstrate that for particular sheet shapes and velocities, analytical approximations may be derived which mimic the exact solutions found by Crane. This allows us to quantify errors associated with neglecting surface deformation and is validated by the numerical solution of the full Navier-Stokes equations using the finite element software FEniCS. Note that the deforming analysis presented in Section 3.3 appears in the publication Hanevy *et al.* [45].

Chapters 4 and 5 contain the complimentary numerical and asymptotic analysis of the modal stability of the temperature dependent extension of Crane's problem respectively. The numerical analysis is performed at a local Reynolds number equivalent to the dimensionless streamwise location. This allows us to parallelise the flow in a similar manner as for both the isothermal problem [39], and the rotating disk [67], by removing the streamwise dependence of our basic flow solutions replacing the x terms in our linear stability equations with their definition in terms of the local Reynolds number. Although the flow is not strictly homogeneous in the streamwise direction it is reasonable to make this parallel-flow-type approximation given that we expect the onset of linear instability to occur sufficiently far enough downstream. As a result

of our parallelisation, a number of higher order basic flow terms appear in our linearised Navier-Stokes equations. The relative importance of these terms is assessed using an integral energy analysis, as well as through comparison to a standard Orr-Sommerfeld formulation. Numerical solutions are subsequently validated by a large Reynolds number, lower branch asymptotic stability analysis. Using only the leading order term in our expansion, excellent agreement between the two approaches is shown. Sections 3.2, 4.2, 4.3 and 5.2 have been submitted as Hanevy *et al.* [46] and are currently under review.

In Chapter 6, we conclude by seeking alternative energy growth mechanisms in the form of optimal perturbations. This analysis aims to determine initial disturbances which produce the greatest transient increase in perturbation kinetic energy over much shorter time scales than the modal analysis of Chapters 4 and 5. This is motivated by the large critical Reynolds numbers for Crane's flow, particularly in the isothermal case, which raises the question of whether the flow would remain laminar at such high Reynolds numbers in practice. Here we demonstrate, in contrast to the modal analysis, that the higher order basic flow terms lead to fundamentally different behaviour and act to stabilise the system. This is also observed in the rotating disk, where the inclusion of higher order basic flow terms associated with streamline curvature and Coriolis forces, increases the critical Reynolds number in the modal analysis and improves the agreement between theory and experiment [73]. Whether this is the case for the non-modal stability of the stretching case remains an open question and warrants further investigation.

We summarise our findings in Chapter 7 and outline ways in which our analysis may be extended in Chapter 8. In particular we demonstrate the promise of the parabolised stability equations (PSE), as a means to quantify not only non-parallel effects for Crane's flow, but also the impact of surface curvature on convective instabilities induced by extrusion processes. Furthermore, we comment on several existing studies which have addressed the coupled sheet-fluid system. These studies have typically focused on regimes which are not relevant to extrusion flows which are the focus of this thesis. However, many of the ideas used show promise and we suggest a number of ways in which they may be adapted to model the boundary layer flow induced by the stretching of a highly viscous sheet.

Chapter 2

Problem Formulation

In this Chapter we introduce two new formulations which extend previously proposed models of the flow induced by the motion of stretching sheets. As stated in the previous Chapter, many of the existing models have considered simplified versions of the sheets dynamics by assuming that the sheet is flat and that temperature variations do not affect the material properties of the ambient fluid. Here we address these shortcomings to explore the influence of these additional physical effects. The formulations presented in this Chapter are general in that we don't impose a particular shape or temperature dependent viscosity function. This will be addressed in the following Chapter where we present basic flow solutions for a range of specific cases.

2.1 Motivation

The goal of any drawing process is to produce a sheet with a narrow cross-sectional area. Regardless of the material being used, two key phenomena typically occur to achieve this. First, the sheet must accelerate. Due to the conservation of mass, this acceleration will cause the sheet to deform and reduce its cross-sectional area in the drawing direction. Secondly, the sheet typically undergoes a change in state. For polymer extrusion, this means that molten polymer is stretched as it cools before solidifying at the outlet. For glass sheet redrawing, a solid sheet of glass is fed into a heater or furnace where it melts and is stretched before solidifying at the outlet. These are the effects that we will account for in the following analysis. Note that while one or more changes of state are typically observed during drawing processes, many polymers can undergo plastic deformation, whereby the material may permanently deform when subjected to sufficient forces. As a result, we will independently consider the roles of both temperature variations and the sheet's deformation.

Temperature effects are accounted for by coupling the Navier Stokes equations to an energy equation. In modelling the behaviour of the fluid, we follow the analysis of Miller *et al.* [77], who examined the stability of the Blasius boundary layer over a heated flat plate. We assume that the sheet is at a constant temperature which is greater than the free-stream ambient temperature. This constant temperature approximation aligns with observations regarding polymer extrusion, wherein the majority of the stretching occurs near the vicinity of the die before the molten polymer has significantly cooled [114]. The Navier Stokes and energy equations are then coupled by imposing a temperature dependent viscosity. The motion of the sheet is prescribed in the same manner as Crane [23], where the sheet is assumed to accelerate at a rate proportional to the distance from the inlet. As stated in the previous Chapter, the way we have incorporated temperature dependence into our model assumes that we are within half a meter of the inlet and that the overall reduction in cross-sectional area of the sheet is small. While this represents a simplification of the physics underlying such processes, it allows us in subsequent Chapters to directly compare our results to those in Griffiths *et al.* [39], regarding the role of temperature in the stability of the system. The implications of these assumptions, as regards to the stability results we obtain in subsequent Chapters will be revisited in due course. Additionally, we further investigate the role of viscous dissipation, which is the energy lost to heat via viscosity. While dissipative effects are typically only observed for compressible flows, we include them here due to the action of the stretching sheet.

When considering surface deformation, we treat the sheet as a solid object and prescribe its shape. The curved geometry is handled by performing a coordinate system transformation to “flatten” the sheet. A simplified system of boundary layer equations is then derived by using the usual large Reynolds number based boundary layer approximation. This allows us to explore a wider range of extrusion processes by covering both cases where the reduction in cross-sectional area of the sheet is large, and by allowing us to more realistically model the boundary layer further downstream from the inlet. The sheet itself would usually be modelled as a low Reynolds number fluid, whereas the large Reynolds number approximation in the boundary layer is easily justified by considering the large discrepancy in the viscosities between the sheet and the surrounding air. This significant difference in Reynolds numbers between the two phases provides a challenge in properly coupling the two fluids. This is discussed further in Chapter 8.

2.2 General Formulation

Consider the steady flow of an incompressible, Newtonian fluid over an impermeable, semi-infinite plate with velocity $\mathbf{U}^* = (u^*, v^*)$. The streamwise coordinate is x^* , and the wall-normal coordinate is y^* with asterisks denoting dimensional quantities. The temperature of the fluid is T^* and the sheet is held fixed at a temperature T_w^* . This flow is governed by the continuity and

the Navier-Stokes and heat equations,

$$\nabla^* \cdot \mathbf{U}^* = 0, \quad (2.1a)$$

$$\rho^* \frac{D\mathbf{U}^*}{Dt^*} = -\nabla^* p^* + \nabla^* \cdot \boldsymbol{\tau}^*, \quad (2.1b)$$

$$\rho^* c_\nu^* \frac{DT^*}{Dt^*} = \kappa^* \nabla^{*2} T^* + \Phi^*. \quad (2.1c)$$

The fluid density is ρ^* , thermal conductivity κ^* , and specific heat capacity c_ν^* . The Newtonian viscous stress tensor is given by $\boldsymbol{\tau}^* = \mu^*(T^*)\dot{\boldsymbol{\gamma}}^*$, where $\dot{\boldsymbol{\gamma}}^* = \nabla^* \mathbf{U}^* + (\nabla^* \mathbf{U}^*)^T$ is the rate of strain tensor and $\mu^*(T^*)$ is the dynamic viscosity. The viscous dissipation function Φ^* is defined as such

$$\Phi^* = \mu^* \left\{ 2 \left[\left(\frac{\partial u^*}{\partial x^*} \right)^2 + \left(\frac{\partial v^*}{\partial y^*} \right)^2 \right] + \left(\frac{\partial v^*}{\partial x^*} + \frac{\partial u^*}{\partial y^*} \right)^2 \right\},$$

and the boundary conditions are as follows

$$\mathbf{U}^* \cdot \hat{\mathbf{t}} - U_w^*(x^*) = \mathbf{U}^* \cdot \hat{\mathbf{n}} = T^* - T_w^* = 0 \quad \text{at } y^* = s^*(x^*), \quad (2.1d)$$

$$u^* \rightarrow T^* - T_\infty^* \rightarrow 0 \quad \text{as } y^* \rightarrow \infty, \quad (2.1e)$$

with T_∞^* being the free stream temperature, U_w^* being the velocity of the sheet, and $\hat{\mathbf{n}}$, and $\hat{\mathbf{t}}$ being unit vectors normal and tangential to the surface of the sheet whose shape is defined by the function $s^*(x^*)$. Here we have retained the time-dependant form of the equations so as to maintain generality. This is since the unsteady, non-dimensional temperature dependant equations are required for the associated linear stability analysis. In the remainder of this Chapter we will look at different combinations of shapes, wall velocities and viscosity distributions to more accurately describe flows observed in extrusion processes.

2.2.1 Temperature Dependence

To model a temperature gradient between the sheet and the free stream, we follow the isothermal analysis of Crane and prescribe the sheet to be flat, such that $s^*(x^*) = 0$. We further assume that the sheet stretches at a rate $a^* x^*$ so that the dimensional boundary conditions become

$$u^* - a^* x^* = v^* = T^* - T_w^* = 0 \quad \text{at } y^* = 0,$$

$$u^* \rightarrow T^* - T_\infty^* \rightarrow 0 \quad \text{as } y^* \rightarrow \infty.$$

To nondimensionalise the system (2.1) we consider the following set of scales

$$\begin{aligned} \mathbf{U}^* &= a^* l^* \mathbf{U}, & (x^*, y^*) &= l^*(x, y) & t^* &= \frac{t}{a^*}, \\ p^* &= \rho^* a^{*2} l^{*2} p, & \mu^* &= \mu_\infty^* \mu, & T^* - T_\infty^* &= T \Delta T^*, \end{aligned}$$

where the non-dimensionalising length scale is l^* , μ_∞^* is the free stream value of the dynamic viscosity and $\Delta T^* = T_w^* - T_\infty^*$. This leads to the following dimensionless system of equations

$$\nabla \cdot \mathbf{U} = 0, \quad (2.2a)$$

$$\frac{D\mathbf{U}}{Dt} = -\nabla p + \text{R}^{-1} \nabla \cdot \boldsymbol{\tau}, \quad (2.2b)$$

$$\frac{DT}{Dt} = \text{R}^{-1} \text{Pr}^{-1} \nabla^2 T + \text{R}^{-1} \text{Ec} \Phi, \quad (2.2c)$$

where $\text{R} = \rho^* a^* l^{*2} / \mu_\infty^*$ is the Reynolds number, $\text{Pr} = c_v^* \mu_\infty^* / \kappa^*$ is the Prandtl number and $\text{Ec} = (a^* l^*)^2 / c_v^* \Delta T^*$ is the Eckert number. The boundary conditions are now

$$u = x, \quad v = 0, \quad T = 1 \quad \text{at } y = 0, \quad (2.2d)$$

$$u \rightarrow 0, \quad T \rightarrow 0 \quad \text{as } y \rightarrow \infty. \quad (2.2e)$$

2.2.2 Surface Deformation

The widespread use of flat Cartesian boundary layers in the literature is primarily due to their mathematical convenience. This, however, obscures the importance of curvature in the flow domain for a number of instabilities observed in practice. One such example in boundary layer flows is the development of Görtler vortices over concave surfaces. The classical description of this instability is found by examining the stability of a Blasius flow past a concave sheet of constant curvature. The instability is governed by a system of boundary layer equations in which an additional centrifugal forcing term arises due to the change in geometry, as described by Saric *et al.* [95]. The instability can be qualitatively described by using the standard parallel flow type arguments as used for the Tollmein-Schlichting instability. However Hall [43] shows that this leads to quantitatively poor predictions and that a streamwise marching solution of the full system of boundary layer equations is required to accurately capture to disturbance evolution.

In the classical treatment of the Görtler problem, the basic flow is assumed not to change to leading order as a result of the curvature, (*i.e.* the curvature is assumed to be small). Here we derive a modified system of boundary layer equations for the basic flow that fully account for streamwise variations in both shape and sheet velocity. The implications of this change in

geometry with respect to the Görtler instability is revisited in Chapter 8.

In what follows we consider boundary-layer flows over non-flat surfaces for $x^* \in [0, \infty)$. As such, it proves useful to introduce a change in coordinate system with $\xi^* = x^*$, and $\eta^* = y^* - s^*$. We further simplify our analysis by focussing on the steady state solutions as we have yet to analyse the stability of our new basic flow solutions. Note that here we impose that the viscosity is constant in order to simplify the derivation that follows. However, the influence of a temperature dependent viscosity distribution could easily be incorporated. The transformed governing equations are then

$$\frac{\partial u^*}{\partial \xi^*} + \frac{\partial \tilde{v}^*}{\partial \eta^*} = 0, \quad (2.3a)$$

$$u^* \frac{\partial u^*}{\partial \xi^*} + \tilde{v}^* \frac{\partial u^*}{\partial \eta^*} = -\frac{1}{\rho^*} \frac{\partial p^*}{\partial \xi^*} + \nu^* \mathcal{L}_1^* u^* + \frac{1}{\rho^*} \frac{ds^*}{d\xi^*} \frac{\partial p^*}{\partial \eta^*}, \quad (2.3b)$$

$$u^* \frac{\partial \tilde{v}^*}{\partial \xi^*} + \tilde{v}^* \frac{\partial \tilde{v}^*}{\partial \eta^*} + \frac{d^2 s^*}{d\xi^{*2}} u^{*2} = -\frac{\sigma^{*2}}{\rho^*} \frac{\partial p^*}{\partial \eta^*} + \nu^* \mathcal{L}_1^* \tilde{v}^* + \frac{1}{\rho^*} \frac{ds^*}{d\xi^*} \frac{\partial p^*}{\partial \xi^*} + \nu^* \mathcal{L}_2^* u^*, \quad (2.3c)$$

where $\nu^* = \mu^*/\rho^*$ is the kinematic viscosity, and the differential operators are

$$\mathcal{L}_1^* = \frac{\partial^2}{\partial \xi^{*2}} - \frac{d^2 s^*}{d\xi^{*2}} \frac{\partial}{\partial \eta^*} - 2 \frac{ds^*}{d\xi^*} \frac{\partial^2}{\partial \xi^* \partial \eta^*} + \sigma^{*2} \frac{\partial^2}{\partial \eta^{*2}}, \quad (2.3d)$$

$$\mathcal{L}_2^* = 2 \frac{d^2 s^*}{d\xi^{*2}} \left(\frac{\partial}{\partial \xi^*} - \frac{ds^*}{d\xi^*} \frac{\partial}{\partial \eta^*} \right) + \frac{d^3 s^*}{d\xi^{*3}}. \quad (2.3e)$$

In the $\xi - \eta$ coordinate system the wall-normal velocity is defined as such

$$\tilde{v}^* = v^* - \frac{ds^*}{d\xi^*} u^*, \quad (2.3f)$$

and the function σ^* , which represents a measure of the surface curvature, is expressed like so

$$\sigma^{*2} = 1 + \left(\frac{ds^*}{d\xi^*} \right)^2. \quad (2.3g)$$

System (2.3) is solved subject to the wall conditions $\mathbf{u}^* \cdot \hat{\mathbf{t}} = U_w^*(\xi^*)$, and $\mathbf{u}^* \cdot \hat{\mathbf{n}} = 0$, where $U_w^* \geq 0$, is the dimensional wall velocity. In this transformed coordinate system, in the absence of any oncoming flow, the relevant boundary conditions for this problem are then

$$u^*(\eta^* = 0) = U_w^*(\xi^*)/\sigma^*(\xi^*), \quad \tilde{v}^*(\eta^* = 0) = 0, \quad u^*(\eta^* \rightarrow \infty) \rightarrow 0. \quad (2.4)$$

These conditions ensure that there is always no flow normal to the surface (no penetration), and that the surface moves tangentially to itself with velocity U_w^* . We consider the development of a boundary-layer due to the non-constant wall velocity ($U_w^* = U_w^*(\xi^*)$) of the plate. For example, the case when $U_w^* = C^* \xi^*$, corresponds to linear stretching of the surface with the constant C^*

having units s^{-1} . This problem, in the non-deformed frame of reference, has been well studied and was first considered by Crane [23]. The problem is non-dimensionalised like so

$$(\xi, Y, s) = \frac{(\xi^*, \eta^*, s^*)}{L^*}, \quad (u, \tilde{v}, U_w) = \frac{(u^*, \tilde{v}^*, U_w^*)}{U^*}, \quad p = \frac{p^*}{\rho^* U^{*2}},$$

where U^* , and L^* , are reference velocity and length scales, respectively. Note that the reference velocity and length scales in the deforming case differ from the flat, temperature dependent case and are not explicitly defined as they depend on the exact shape and velocity of the sheet. This is discussed further in the next Chapter when specific case studies are examined. In order to then arrive at the relevant boundary-layer equations the following scalings are introduced $\eta = \text{Re}^{1/2} Y$, and $v = \text{Re}^{1/2} \tilde{v}$, where $\text{Re} = U^* L^* / \nu^*$. This change in notation for the definition of the Reynolds number is chosen to highlight the difference in scaling between the deforming and temperature dependent cases. As a result of this scaling system (2.3) reduces to

$$\frac{\partial u}{\partial \xi} + \frac{\partial v}{\partial \eta} = 0, \quad (2.5a)$$

$$u \frac{\partial u}{\partial \xi} + v \frac{\partial u}{\partial \eta} = s'_\xi \text{Re}^{1/2} \frac{\partial p}{\partial \eta} - \frac{\partial p}{\partial \xi} + \sigma^2 \frac{\partial^2 u}{\partial \eta^2} - \frac{1}{\text{Re}^{1/2}} \left(s''_{\xi\xi} \frac{\partial u}{\partial \eta} + 2s'_\xi \frac{\partial^2 u}{\partial \xi \partial \eta} \right) + \frac{1}{\text{Re}} \frac{\partial^2 u}{\partial \xi^2}, \quad (2.5b)$$

$$\begin{aligned} \frac{1}{\text{Re}} \left(u \frac{\partial v}{\partial \xi} + v \frac{\partial v}{\partial \eta} \right) + \frac{s''_{\xi\xi} u^2}{\text{Re}^{1/2}} &= \frac{s'_\xi}{\text{Re}^{1/2}} \frac{\partial p}{\partial \xi} - \sigma^2 \frac{\partial p}{\partial \eta} + \frac{\sigma^2}{\text{Re}} \frac{\partial^2 v}{\partial \eta^2} \\ &- \frac{1}{\text{Re}^{3/2}} \left(s''_{\xi\xi} \frac{\partial v}{\partial \eta} + 2s'_\xi \frac{\partial^2 v}{\partial \xi \partial \eta} \right) + \frac{1}{\text{Re}^2} \frac{\partial^2 v}{\partial \xi^2} \\ &+ \frac{1}{\text{Re}} \left[2s''_{\xi\xi} \left(\frac{1}{\text{Re}^{1/2}} \frac{\partial u}{\partial \xi} - s'_\xi \frac{\partial u}{\partial \eta} \right) + \frac{s'''_{\xi\xi\xi} u}{\text{Re}^{1/2}} \right], \end{aligned} \quad (2.5c)$$

where the primes with associated subscripts denote differentiation with respect to the subscript variable and $\sigma^2 = 1 + (s'_\xi)^2$. In order to determine the correct leading order balance the following expansions are introduced

$$\begin{aligned} u(\xi, \eta) &= u_0(\xi, \eta) + \text{Re}^{-1/2} u_1(\xi, \eta) + \dots, \\ v(\xi, \eta) &= v_0(\xi, \eta) + \text{Re}^{-1/2} v_1(\xi, \eta) + \dots, \\ p(\xi, \eta) &= p_0(\xi) + \text{Re}^{-1/2} p_1(\xi, \eta) + \dots, \end{aligned}$$

where, to leading order, the pressure is a function of ξ only (this can be directly inferred from (2.5c)). Thus, the leading order boundary-layer equations for these classes of problems are as

follows

$$\frac{\partial u_0}{\partial \xi} + \frac{\partial v_0}{\partial \eta} = 0, \quad (2.6a)$$

$$u_0 \frac{\partial u_0}{\partial \xi} + v_0 \frac{\partial u_0}{\partial \eta} + \sigma^{-1} \sigma'_\xi u_0^2 = -\sigma^{-2} (p_0)'_\xi + \sigma^2 \frac{\partial^2 u_0}{\partial \eta^2}. \quad (2.6b)$$

This system is the Newtonian equivalent of the non-Newtonian equations derived, for example, by Pop and Nakamura [88]. In the case when the plate is flat, i.e. s is constant, the above reduces to the familiar 2D boundary-layer equations. Outside the boundary layer the flow must match with the far-field stationary flow, $U_\infty = 0$. By considering the behaviour of equation (2.6b) at a large distance from the surface of the plate the pressure, to leading order, is determined to be constant. Thus

$$\frac{\partial u_0}{\partial \xi} + \frac{\partial v_0}{\partial \eta} = 0, \quad (2.7a)$$

$$u_0 \frac{\partial u_0}{\partial \xi} + v_0 \frac{\partial u_0}{\partial \eta} + \sigma^{-1} \sigma'_\xi u_0^2 = \sigma^2 \frac{\partial^2 u_0}{\partial \eta^2}. \quad (2.7b)$$

The above system is then closed subject to the following conditions

$$u_0(\eta = 0) = U_w(\xi)/\sigma(\xi), \quad v_0(\eta = 0) = 0, \quad u_0(\eta \rightarrow \infty) \rightarrow 0. \quad (2.7c)$$

This system of boundary-layer equations is general in the sense that one is not restricted by any of the dynamics of the deforming surface. In what follows we seek to extend previous analyses and wish to determine self-similar solutions of (2.7) without *a priori* knowledge of either the deforming surface profile or the wall velocity.

Chapter 3

Basic Flow Solutions

In this Chapter we derive basic flow solutions for the flat temperature dependent and deforming sheet cases outlined in the previous Chapter using a combination of analytical and numerical approaches. Our analytical solutions exploit the self similarity of the respective boundary layers, while our numerical schemes include a Keller-Box method, which utilises the parabolic nature of the boundary layer equations in the flat temperature dependent case to iteratively march downstream in the coupled nonlinear case, as well as a finite element solution of the full Navier-Stokes equations when considering the role of deformation. In doing so we will show that failing to account for these additional physical effects leads to quantitatively incorrect predictions for a number of flow variables of interest. Note that the analysis in Section 3.3 appears in the publication Hanevy *et al.* [45], while 3.2 has been submitted as part of the publication Hanevy *et al.* [46], which is under review.

3.1 Introduction

To determine the most important physical effects in determining the linear stability of the flow induced by a stretching sheet which were omitted in Griffiths *et al.* [39], we first have to evaluate the basic flow solutions in these more physically realistic regimes. There are a number of features of Crane's basic flow profile which makes it an attractive model to perform a linear stability analysis about. First is the fact that we have analytical basic flow solutions. Given that eigenvalue calculations in a hydrodynamic stability context are very sensitive to the accuracy of the basic flow, this removes a potential source of error from their calculation. Second is the fact that the wall velocity accelerates at a constant rate, proportional to distance along the stretching axis. One would assume that the stretching of the sheet would cause issues for stability calculations, however the constant rate of acceleration allows one to make a parallel

flow approximation similar to that employed in the rotating disk boundary layer. As such the majority of the solutions that are presented in the remainder of this Chapter will be chosen to mimic those of Crane to facilitate the comparison of both the basic flow and the flow stability in the Chapters which follow.

The objective therefore, is to identify the mechanisms which contribute to the overall stability of the systems under consideration. The models we propose are intended to improve models which have appeared in the literature, while also being amenable to analysis using the tools of hydrodynamic stability theory. In this sense our approach mirrors the use of the rotating disk boundary layer to model crossflow instabilities on a swept wing. This approach has resulted in a number of control flow strategies being proposed such as surface compliance, suction and porosity ([21],[76],[17]).

Here we are extending the near inlet, small deformation, constant sheet temperature analysis of Vleggaar [114]. Vleggaar's work focused on quantifying the additional heat transferred from the sheet to the boundary layer due to the sheet's acceleration, assuming constant viscosity. He demonstrated that heat transfer increases with the sheet's acceleration, aligning qualitatively with experimental results. In this study, we allow the viscosity of the induced boundary layer to vary with temperature, providing a more realistic model of the near-inlet, small-deformation regime. To broaden the range of scenarios considered, we also examine the role of sheet deformation. This approach enables us to investigate both the character of the basic flow further from the inlet and cases where the sheet's thickness varies significantly.

The remainder of this Chapter is structured as follows. In Section 3.2 we evaluate the basic flow profiles for Crane's flow with a temperature gradient. We start by looking at the temperature independent case where the viscosity is constant to validate the secant shooting scheme used in the remainder of this Chapter. We then assess the role of a varying viscosity distribution, firstly by comparing two different viscosity distributions in the absence of viscous dissipation, before including dissipation using a pseudo self-similar approach. Finally in Section 3.2.3 we solve the governing boundary layer PDEs using a Keller-Box scheme, where we show that the effects of viscous dissipation prevent the basic flow profiles from being self similar in this regime.

In Section 3.3 we look at particular combinations of surface shapes and wall velocities. While we are primarily interested in the thinning profiles observed in extrusion processes, we also demonstrate how our formulation may be adapted to model thickening processes, such as those observed in textile compaction. Such a process is essentially the converse of the sheet-thinning processes discussed previously, whereby a material is fed into a compactor at a greater speed than it is extracted. These types of processes exploit the fact that fibrous materials exhibit viscoelastic behaviour [8]. Here this is manifested as an increase in stress within the fibre after

a compaction-relaxation cycle which prevents the fibre from recovering to its initial volume. There is a wealth of literature attempting to explain this phenomenon and an overview of different modelling approaches is provided in Kelly [62]. We show that, under certain limiting assumptions, analytical boundary-layer solutions may be derived. As one would expect, these results depend on the physics of the system being considered, specifically the exact profile of the deforming surface and the wall velocity of said surface. The analysis we present is generalised. However, all the solutions can be tailored to model flows observed in practice, given sufficient knowledge of the aforementioned physical constraints. In Section 3.3.2 we validate our analytical approximations by using the finite element software FEniCs [68], where we find excellent agreement between both approaches.

3.2 Temperature Dependence

In this Section we investigate the flow induced by a linearly stretched flat surface by extending the analysis of Crane [23], adding both a temperature gradient and viscous dissipation to Crane's model. Although the model presented has its limitations as it does not consider the deformation of the sheet during stretching, the flat surface approximation remains valid when assuming a small rate of deformation. Furthermore, the availability of simple analytic solutions for the basic flow equations has made the flat surface approximation a prominent feature in the literature. This enables us to validate our extended analysis by comparing it with existing results in the literature. We will demonstrate that due to the accelerating nature of the flow, the role of viscous dissipation becomes more pronounced near the surface of the plate as we progress in the streamwise direction.

3.2.1 Similarity Solutions

To solve the steady, coupled momentum and energy equations (2.2), we proceed by introducing the following similarity transformation

$$u = xu_B = xf'(\eta), \quad v = v_B = -R^{-\frac{1}{2}}f(\eta), \quad p = p_0 + R^{-1}p_B(\eta), \quad (3.1a)$$

$$T_B = T(\eta), \quad \mu_B = \mu(\eta), \quad \eta = R^{\frac{1}{2}}y, \quad (3.1b)$$

where η is our boundary layer coordinate. Gathering the leading order terms, the governing boundary layer equation become

$$\mu f''' + \mu' f'' + f f'' - f'^2 = 0, \quad (3.2a)$$

$$-f f' - \mu f'' - 2\mu' f' = p', \quad (3.2b)$$

$$T'' + \text{Pr}(f T' + \text{Ec } x^2 \mu (f'')^2) = 0. \quad (3.2c)$$

The largest term in Φ for $R \gg 1$ is $\left(\frac{\partial u}{\partial y}\right)^2$. This leads to the x^2 term in equation (3.2c) which means that our self similar approach is no longer valid. This will be discussed below when we compare numerical solutions of the full governing system of PDEs to a self similar approximation where we treat $\text{Ec } x^2$ as a parameter and solve the ODEs above at different values of x . Such an approach may be justified provided that the Eckert number is sufficiently small leading to the variation in x being much slower than the variation in y . The boundary conditions are

$$f = f' - 1 = T - 1 = 0 \quad \text{at } \eta = 0, \quad (3.2d)$$

$$f' \rightarrow 0, \quad T \rightarrow 0 \quad \text{as } \eta \rightarrow \infty. \quad (3.2e)$$

3.2.2 Constant Viscosity, No Dissipation

The Eckert phenomena in the context of extrusion processes would be the heating of the stretching sheet in spite of the temperature of the sheet being significantly greater than the heat of the ambient fluid. It was first proposed by Geropp [36] in the context of a boundary layer induced by a rotating cylinder. This effect was predicted to occur with an Eckert number of order one, which required a rotational Reynolds number of approximately 6.9×10^6 . This rotational Reynolds number is an order of magnitude larger than the critical Reynolds number observed for the isothermal stretching sheet. Therefore, as an initial approximation we will assume $\text{Ec} = 0$ and ignore the role of viscous dissipation. Setting $\mu = 1$ uncouples the momentum and energy equations and allows us to attain analytic solutions for the boundary layer equations (3.2), where we find

$$f = 1 - e^{-\eta}, \quad u_B = e^{-\eta}, \quad (3.3)$$

$$p_B = p_0 + \frac{1}{2}(1 - e^{-2\eta}), \quad v_B = e^{-\eta} - 1, \quad (3.4)$$

as originally found in Crane [23]. Using our solutions for f above (3.2c) simplifies

$$\text{Pr}(e^{-\eta} - 1)T' = T'', \quad (3.5)$$

which can be solved using the upper incomplete gamma function defined $\Gamma(s, x) = \int_x^\infty t^{s-1} e^{-t} dt$, so that

$$T_B = \frac{\Gamma(\text{Pr}, \text{Pr} e^{-\eta}) - \Gamma(\text{Pr}, 0)}{\Gamma(\text{Pr}, \text{Pr}) - \Gamma(\text{Pr}, 0)} \quad (3.6)$$

or

$$T_B = \frac{e}{1-e} \left(e^{-e^{-\eta}} - 1 \right) \quad (3.7)$$

when $\text{Pr} = 1$. The boundary layer equations were solved numerically using a shooting method where the boundary value problem is solved as an initial value problem. The missing initial conditions $f''(0)$ and $T'(0)$ are guessed, and the problem is solved using a fourth order Runge-Kutta method. Newtons method is then used to find the initial conditions which satisfy the free stream conditions $f' \rightarrow T \rightarrow 0$, as $\eta \rightarrow \infty$ where the domain is truncated at $\eta_{max} = 40$ to facilitate the numerical solution. This relatively large value of η_{max} was chosen as the spectral method used in the numerical solution of the linear disturbance equations (4.5) requires highly accurate basic flow solutions for convergence. Full details of the calculation are provided in Appendix A.1.1. The availability of analytic solutions allows us to validate our numerical solution for the constant viscosity case before solving the coupled problem. In Figure 3.1 we see that the numerical and analytic solutions are indistinguishable on the scale of the plot. Though we could have imposed the analytic initial conditions, they were perturbed to ensure that the numerical scheme converged. Note that we used $\text{Pr} = 1$ in Figure 3.1 to validate our numerical scheme since we have closed form solutions for the basic flow profiles in this case. For the remainder of this thesis we use $\text{Pr} = 0.72$, which models heat transfer in air, the ambient fluid medium in extrusion processes. This value has been used in a number of related studies ([77], [92],[78]).

3.2.3 Viscothermal Flow

For the case of temperature dependent viscosity we chose to compare two different viscosity distributions commonly seen in the literature; an inverse distribution $\mu_1 = (1 + m_1 T)^{-1}$, and an exponential viscosity distribution $\mu_2 = e^{-m_2 T}$, used in Miller *et al.* [77] and Wall and Wilson [116], respectively. Both μ_1 and μ_2 have the important property that $\mu \rightarrow 1$ in the free stream owing to the boundary conditions for T . First, we examine the behaviour of the flow for different values of the sensitivity parameter m_i , taking the inverse viscosity distribution μ_1 . The boundary layer equations (3.2), were solved using the shooting method outlined above for $m_1 = -0.4$ to 0.4 in steps of 0.2 and can be seen in Figure 3.2. Here we observe entrainment of the streamwise velocity profiles as the value of the sensitivity parameter increases. This is interpreted as a

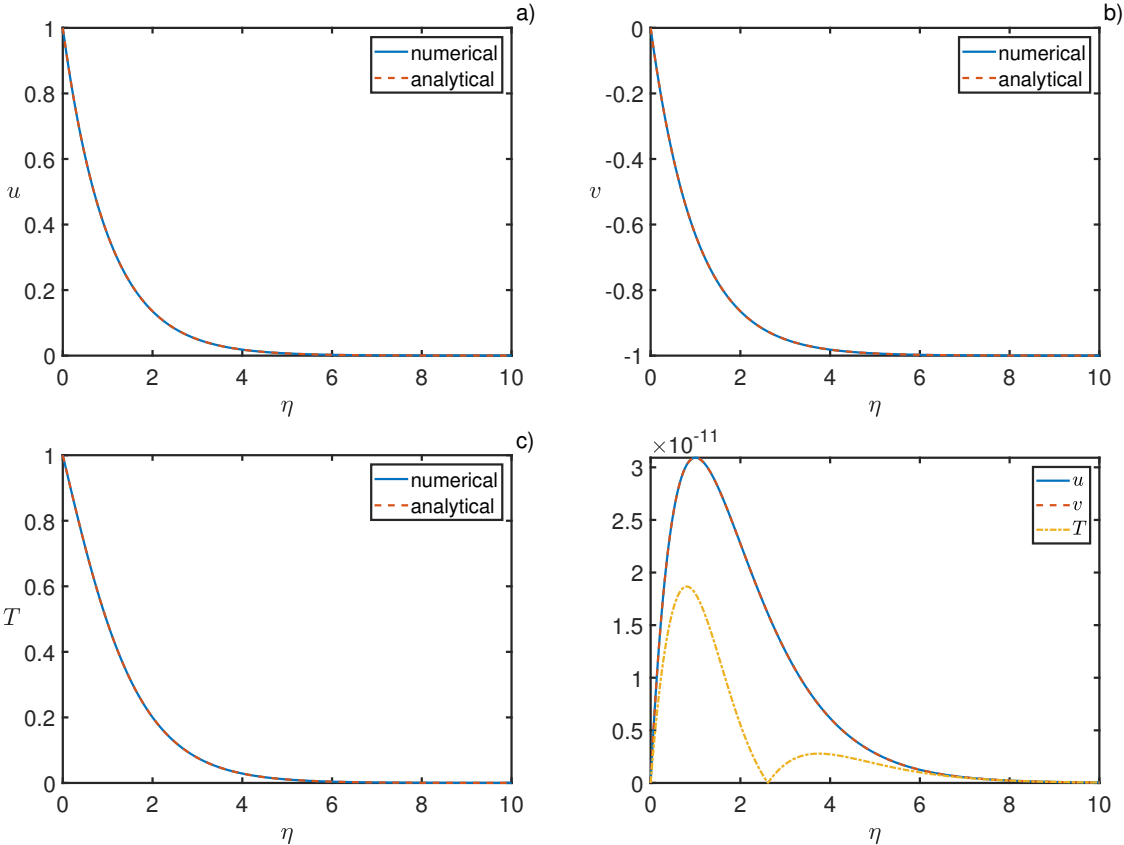


Figure 3.1: Comparison of numerical and analytical solutions of Crane’s problem for the case of constant viscosity, with $Pr = 1$. a) shows u , b) shows v , c) shows T and d) shows the difference between the numerical and analytical solutions. Note that the pressure was omitted as it is a derived quantity and does not effect the performance of our numerical scheme.

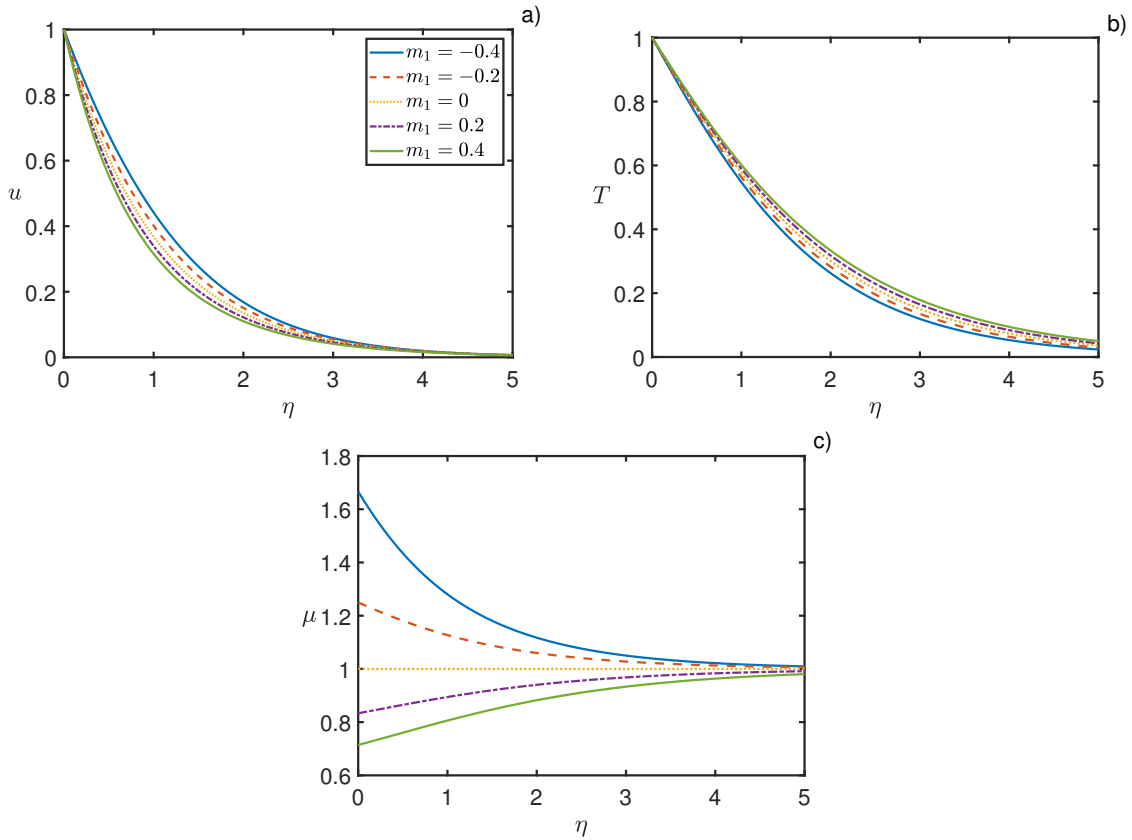


Figure 3.2: Numerical Solution of Crane's problem (3.2) for the inverse viscosity distribution μ_1 for a range of values of the sensitivity parameter m_1 from -0.4 to 0.4 in steps of 0.2 .

reduction in the boundary layer thickness and has important implications for the numerical linear stability analysis in the Chapter which follows. As can be seen, increasing m_1 reduces the viscosity at the wall, reducing the wall shear stress and therefore causing a less impactful viscous interaction between the sheet and the fluid. The thermal boundary layer on the other hand thickens with increasing values of m_1 . This implies that increasing the value of m_1 leads to greater heat transfer between the sheet and the ambient fluid allowing the sheet to be more rapidly cooled.

While it is clear that both μ_1 and μ_2 exhibit similar behaviour for $|m_i| \ll 1$, we will show that the use of either distribution can result in similar base flow solutions. There are a number of ways in which these flows could be compared. The simplest way to compare the flows would be to use one of the initial conditions determined for the other case ($f''(0)$ or $T'(0)$) and use the sensitivity parameter and the other initial condition as shooting parameters to satisfy the boundary conditions. Alternatively the solution to the second problem could be found by imposing that $f(\infty)$ be the same for both flows. The addition of this constraint means that the three parameters $f''(0)$, $T'(0)$ and m_i have to be adjusted in the shooting method to match the

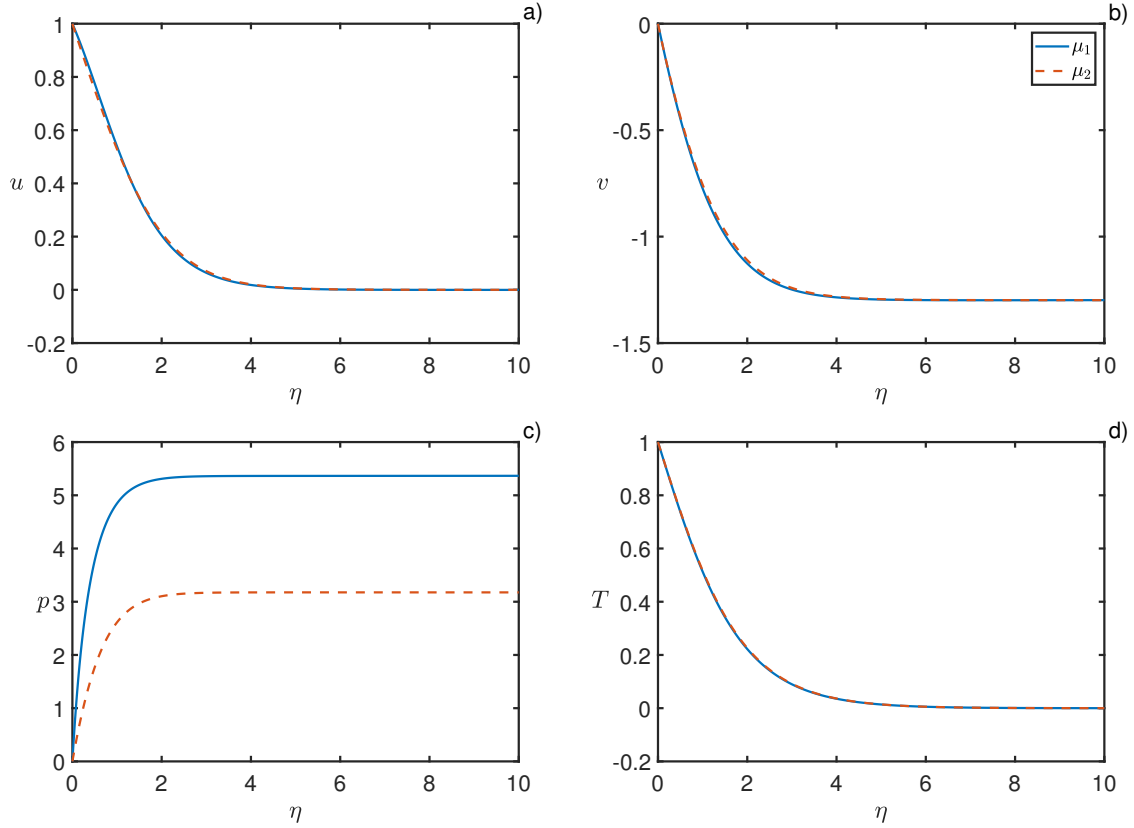


Figure 3.3: Numerical Solution of Crane's problem (3.2) comparing inverse and exponential viscosity distributions μ_1 and μ_2 for $m_1 = -0.75$, $m_2 = -1.06437$. a) shows the difference in the streamwise velocity, b) the wall normal velocity, c) the pressure and d) the temperature profiles.

solutions as shown in Table 3.1. This result of this calculation is shown in Figure 3.3 where the velocity and temperature profiles are almost identical while the pressure, which does not affect the flow since f is determined independently of p , varies substantially. These values are given in Table 3.1. Where $m_1 = -0.75$ was initially chosen for the inverse case as the two distributions are similar for $|m_i| \ll 1$. While the plots do look similar in both cases the initial condition for $f''(0)$ and the sensitivity parameter had to be significantly adjusted to satisfy all of the imposed conditions.

The inclusion of the dissipation term for $Ec \neq 0$, does not change the solution scheme outlined previously provided we treat x as a parameter since the coupled system of nonlinear ordinary differential equations (ODE's) depend only on x and not its derivatives. In this case the unknown initial conditions are a function of x but can be solved for in the same manner for any value of x for $x \in [0, \infty)$. The solution of which is shown using $Ec = 0.01$, $\mu_1(T, m_1 = 0.25)$ in Figure 3.4. It can be clearly seen that the sign of the initial condition $T'(0)$ changes from positive to negative as x grows. Despite the smallness of the Eckert number, the acceleration of the sheet

Table 3.1: The change in boundary conditions and the sensitivity parameter required in order for f_∞ match for the inverse and exponential viscosity distributions.

	Inverse	Exponential
$f''(0)$	-0.384654	-0.513757
$T'(0)$	-0.539522	-0.533796
m	-0.75	-1.06437

as it stretched causes more energy to be lost to heat. This effect is especially pronounced at the surface of the sheet where the streamwise velocity gradient reaches its maximum value. However, we shall see that this approximation does not quantitatively model the numerical solution of the full partial differential equation (2.2).

Near Wall Approximation

A reasonable approximation of the near wall behaviour of the nonlinear coupled system of boundary layer ODE's can be made by taking a first order Taylor expansion of the viscosity in equation (3.1) for $|m| \ll 1$. For the remainder of this thesis we set $\mu_B(T) = (1 + mT)^{-1}$ where we drop the subscript '1' for convenience. If we further set $\mu_B = \mu_B(T)|_{\eta=0} = \mu_{B0} = (1 + m)^{-1}$, and taking inspiration from the isothermal case look for solutions of the form

$$\bar{u}_B \approx e^{-\beta\eta}, \quad \bar{v}_B \approx \frac{1}{\beta} (e^{-\beta\eta} - 1),$$

using bars to denote our approximate solutions, where β is a constant to be determined. Note that these approximations ensure that both the continuity and velocity boundary conditions are satisfied. From the x -momentum equation (3.2a) we have $\mu_{B0}\beta^2 = 1$, using the y momentum and energy equations we recover the following approximations for the pressure and temperature

$$\bar{p}_B \approx -\frac{1}{2\beta} e^{-2\beta\eta} + p_\infty, \quad (3.8)$$

$$\bar{T}_B \approx \frac{\Gamma\left(\frac{Pr}{\beta^2}, \frac{Pr}{\beta^2} e^{-\beta\eta}\right) - \Gamma\left(\frac{Pr}{\beta^2}, 0\right)}{\Gamma\left(\frac{Pr}{\beta^2}, \frac{Pr}{\beta^2}\right) - \Gamma\left(\frac{Pr}{\beta^2}, 0\right)}. \quad (3.9)$$

Note that as $m \rightarrow 0$ we recover the isothermal solutions of Crane. With our approximate solutions we are able to predict a number of flow quantities of interest for the stability analysis

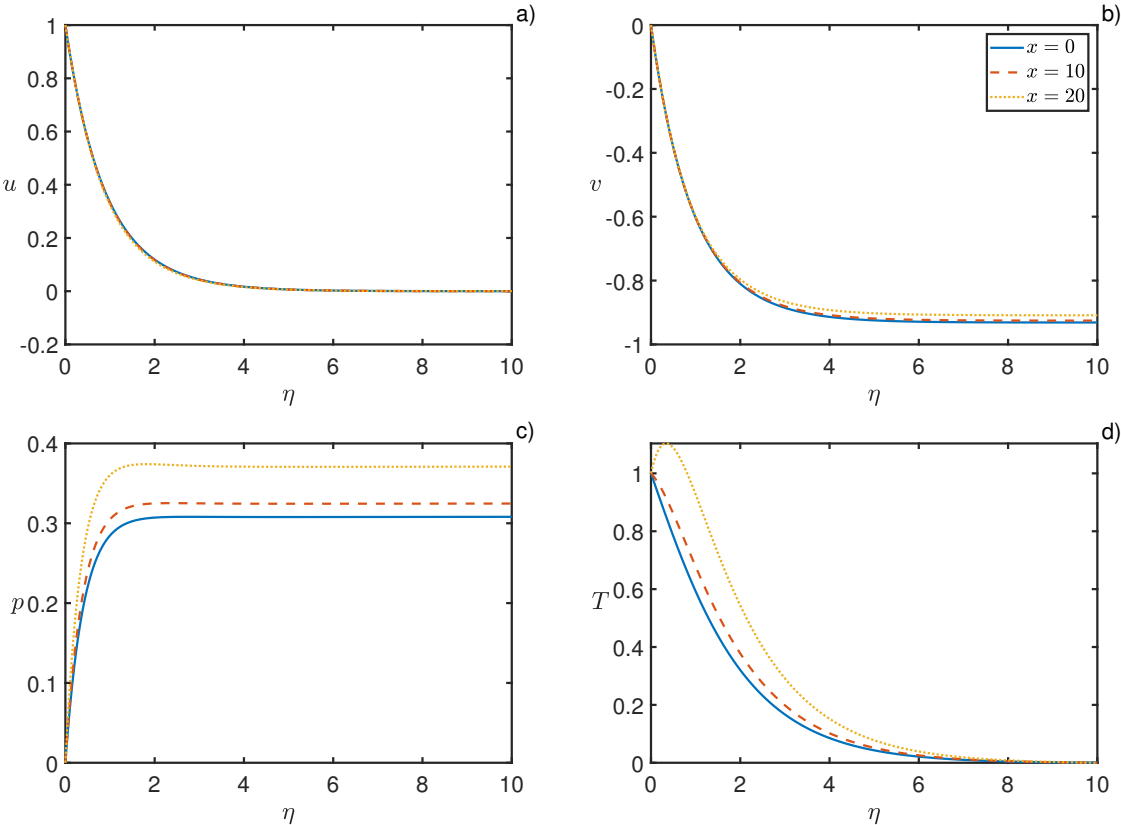


Figure 3.4: Numerical Solution of the Crane’s Problem (3.2) for a range of x values for $Ec = 0.01$ using a pseudo similarity approach whereby $Ec x^2$ is treated as a parameter and the boundary layer equations are solved at different x locations.

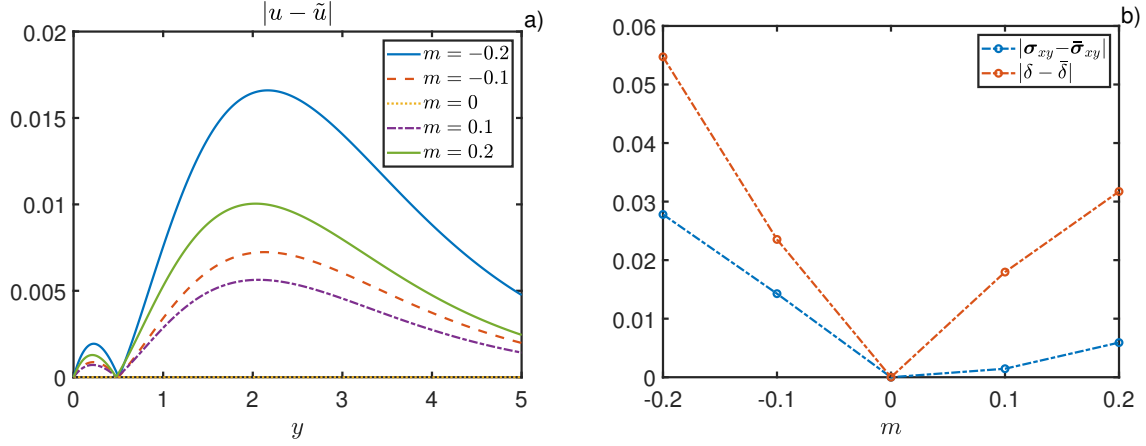


Figure 3.5: Absolute value of the difference between our numerical and approximate, near wall stream wise velocity solutions in a) and b) the absolute value of the errors for the wall shear stress and boundary layer thickness

which follows, namely the wall shear stress and the boundary layer thickness

$$\sigma_{xy} = \mu_{B0} \left. \frac{\partial u}{\partial y} \right|_{y=0}, \quad \sigma_{xy} \approx \bar{\sigma}_{xy} = (1+m)^{-1/2}$$

$$\delta = - \int_0^{\infty} u_B dy = \delta^* \sqrt{\rho^* a^* / \mu_{\infty}^*}, \quad \delta \approx \bar{\delta} = (1+m)^{-1/2}.$$

Plots showing $|u_B - \bar{u}_B|$, $|\sigma_{xy} - \bar{\sigma}_{xy}|$ and $|\delta - \bar{\delta}|$ are shown in Figure 3.5. This simple approximation breaks down as $|1 - \mu_{B0}|$ increases as the further the wall viscosity is from the free stream viscosity the less appropriate it is to approximate the viscosity as being constant. In principle the approximation could be improved by taking more terms in the Taylor series expansion of μ , using \bar{T}_B to compute the derivatives of μ in the expansion. However, inclusion of polynomial terms in y leads to a system of equations which is not analytically solvable.

Numerical Validation

In Figure 3.7 b) we compare our shooting method solutions for $Ec = 0.01$ to the solution of the PDEs (2.2). Here we see that although the pseudo similarity approximation does qualitatively predict the increase in temperature at the wall due to viscous dissipation, it significantly overestimates this effect. This is verified by comparing the approximation to a numerical solution using a Keller-Box scheme and a finite difference scheme for $m = 0$. Details of the numerical schemes are provided in Appendix A. The two schemes were used to verify that the discrepancy is due to the pseudo similarity approach and that the PDE schemes are in fact correct since each corroborates the others results. The finite difference scheme uses the TDMA algorithm

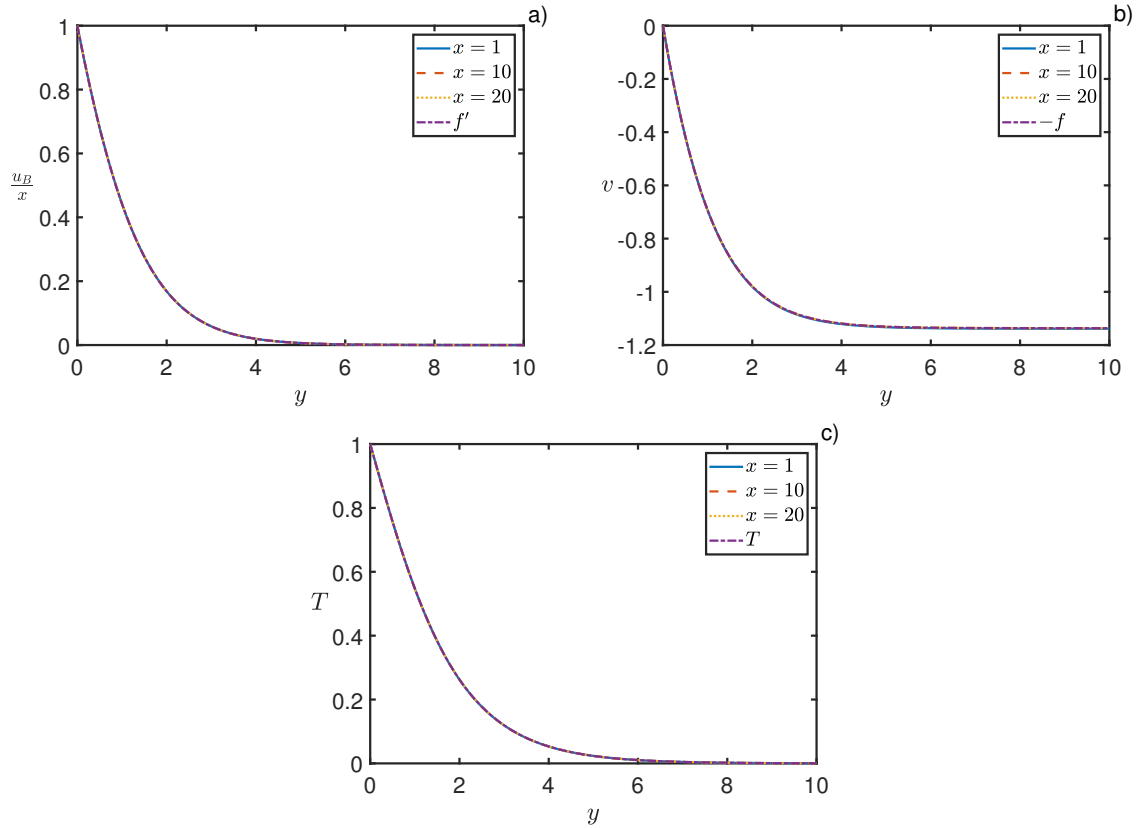


Figure 3.6: KellerBox solution at different streamwise locations compared to the self similar solution in the nondissipative regime, $Ec = 0$, $m = -0.4$. a) Shows the streamwise solutions scaled by the sheets' speed, b) the wall normal and c) the temperature profiles.

and is incapable of handling the nonlinearity introduced when the temperature and velocities are coupled. When $m = 0$, this is not the case, and it verifies the results of the Keller-Box scheme which agrees with our similarity solutions for all values of m when $Ec = 0$. This can be seen in Figure 3.6, where a value $m = -0.4$ was taken as an example. Lastly, we compare the shear at the wall predicted by the Keller-Box method and the pseudo similarity solutions for $Ec = 0.01$ and a range of values of the sensitivity parameter. While it is clear at this stage that the shooting method solutions are incorrect, the value of the shear at the wall becomes important in the asymptotic stability analysis which follows. In Figure 3.7 we see that for all values of m the efficacy of this approximation deteriorates as the distance along the stretching sheet is increased, showing that while this approximation procedure is convenient due to the ease at which base flow solutions can be calculated, it fails to accurately capture the dynamics of the system.

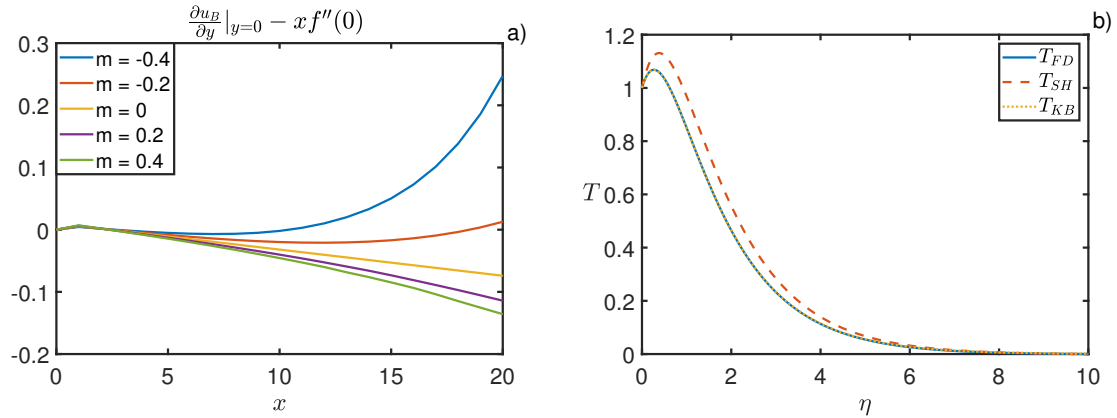


Figure 3.7: a) The difference between the shear at the wall predicted by the Keller-Box and pseudo similarity solutions and b) The overestimation of viscothermal heating for $Ec = 0.01$, $m = 0$ of the similarity solutions. The subscripts FD, SH, and KB denote the finite difference, shooting (pseudo-similarity), and Keller box results respectively.

3.3 Deforming Sheet

In this Section we attain similarity solutions for flow over a deforming surface by modifying the analysis of Rees and Pop [92] who examined boundary layer flow and heat transfer over a wavy moving surface. In the paper a sinusoidal surface profile was imposed with spatially stationary surface waves. The resulting boundary layer equations were solved numerically and physical quantities such as the local skin friction coefficient were reported for a range of different amplitudes and frequencies. While we derive the same governing equations, our analysis differs in that we consider flow over a monotonically thinning or thickening surface whose shape resembles that of a glass sheet undergoing redraw. We then show that for particular sheet profiles, self similar solutions can be obtained provided we impose appropriate velocity profiles within the sheet. This analysis attempts to generalise the results of the previous Section, bridging the gap between analysis of flows induced by flat stretching surfaces, such as Crane's flow discussed in the previous Chapter, and the coupled sheet fluid system proposed in Al-Housseiny and Stone [2]. While we have been unable to resolve the discrepancy between the stresses at the sheet/fluid interface for the coupled problem, we overcome this difficulty by effectively treating the sheet as a solid object with both its shape and velocity being prescribed in a manner that permit the existence of self similar flow profiles.

3.3.1 Self-similar Flows

Assuming that (2.7) admits self-similar solutions we introduce the similarity coordinate

$$\zeta = \frac{\eta}{g(\xi)} \sqrt{\frac{U_w}{\xi\sigma}},$$

and the streamfunction $\psi = g(\xi)\sqrt{U_w\xi/\sigma}f(\zeta)$, where g is a yet to be determined function of ξ . These expressions for ζ and ψ are informed by standard boundary-layer scalings [112] and also the need to ensure that u_0 is proportional to both the wall velocity and the inverse of the function σ . We note that in the case when the wall velocity is constant and the surface is flat the unknown quantity g can be removed from these expressions and the analysis follows identically that of Tsou *et al.* [112].

Given the preceding definitions it follows immediately that

$$\begin{aligned} u_0 &= \frac{\partial\psi}{\partial\eta} = (U_w/\sigma)f'_\zeta, \\ v_0 &= -\frac{\partial\psi}{\partial\xi} = g\sqrt{U_w\xi/\sigma}(\zeta f'_\zeta X_- - f X_+), \end{aligned}$$

where

$$X_\pm = \frac{g'_\xi}{g} + \frac{1}{2\xi} \pm \frac{1}{2} \left[\frac{(U_w)'_\xi}{U_w} - \frac{\sigma'_\xi}{\sigma} \right].$$

Therefore (2.7b) reduces to

$$\xi g^2 [-X_+ f f''_{\zeta\zeta} + U_w^{-1} (U_w)'_\xi (f'_\zeta)^2] = \sigma^2 f'''_{\zeta\zeta\zeta}.$$

In order to be able to determine similarity solutions it must then be the case that

$$\xi g^2 X_+ = c_1 \sigma^2, \quad (3.10a)$$

$$\xi g^2 U_w^{-1} (U_w)'_\xi = c_2 \sigma^2, \quad (3.10b)$$

where c_1 and c_2 are arbitrary constants that ensure self-similarity. The instances when one of these constants is set equal to zero, with the other being non-zero, are considered in Appendix B.1. Rearranging (3.10b) gives $g^2 = c_2 \sigma^2 U_w [\xi (U_w)'_\xi]^{-1}$. Substituting this form for g^2 into (3.10a) one then removes the unknown function g from the problem and arrives at the following second order ODE

$$U_w \frac{d^2 U_w}{d\xi^2} + \gamma \left(\frac{dU_w}{d\xi} \right)^2 - \mathcal{S} U_w \frac{dU_w}{d\xi} = 0, \quad (3.11)$$

where $\mathcal{S} = [\ln(\sigma)]'_\xi$, and $\gamma = 2(c_1 - c_2)/c_2$. We note that the above equation is identically

satisfied when $U_w = \text{constant}$. However, (3.10b) would then imply that $c_2 = 0$. This special case is considered in Appendix B.1. Given the form of (3.11) there are two distinct cases to consider, when $\gamma = -1$, and when $\gamma \neq -1$. In the first case, the substitution $R = [\ln(U_w)]'_\xi$, reduces the order of (3.11) such that

$$\frac{dR}{d\xi} - \mathcal{S}R = 0.$$

Therefore $R = K\sigma$, where K is a constant of integration, and it follows immediately that

$$(U_w)'_\xi = KU_w\sigma. \quad (3.12)$$

In the second case, when $\gamma \neq -1$, the substitution $R = (1 + \gamma)U_w^{1+\gamma}[\ln(U_w)]'_\xi$, leads to the same first order ODE. Therefore, in these cases

$$(U_w)'_\xi = \frac{K\sigma}{(1 + \gamma)U_w^\gamma}. \quad (3.13)$$

This ODE can be rewritten as such

$$W'_\xi = K\sigma, \quad (3.14)$$

where $W = U_w^{1+\gamma}$. Thus, irrespective of the value of γ , in order to be able to determine similarity solutions, one may choose either to specify the wall velocity, U_w , and calculate the variation of the height of the plate, s , or specify s and determine the required form for U_w . With s fixed the determination of U_w transpires to be a relatively simple procedure. Integrating (3.12) and (3.14) respectively we have that

$$U_w = \begin{cases} C e^{K\mathcal{I}} & \text{when } \gamma = -1, \\ (C + K\mathcal{I})^{\frac{1}{1+\gamma}} & \text{when } \gamma \neq -1, \end{cases} \quad (3.15)$$

where C is a constant of integration and \mathcal{I} is simply the arc length of the surface,

$$\mathcal{I}(\xi) = \int \sigma(\bar{\xi}) d\bar{\xi} = \int \sqrt{1 + (s'_\xi)^2} d\bar{\xi}. \quad (3.16)$$

Therefore, for any fixed s it is possible to determine U_w , for any value of γ , simply by integrating the function σ . It is clear from the above analysis that the value of the constant γ dictates the form of the wall velocity. In cases when $\gamma \geq -1$ the deforming surface will be accelerating whilst the inverse is true when $\gamma < -1$. As an example, a deforming surface that is being thinned as it is being stretched would, by mass conservation, have to be accelerating.

Now, by writing $\hat{f}(Z) = \sqrt{c_1}f(\zeta)$, where $Z = \sqrt{c_1}\zeta$, then $\hat{f}'_Z = f'_\zeta$, and the ODE that governs

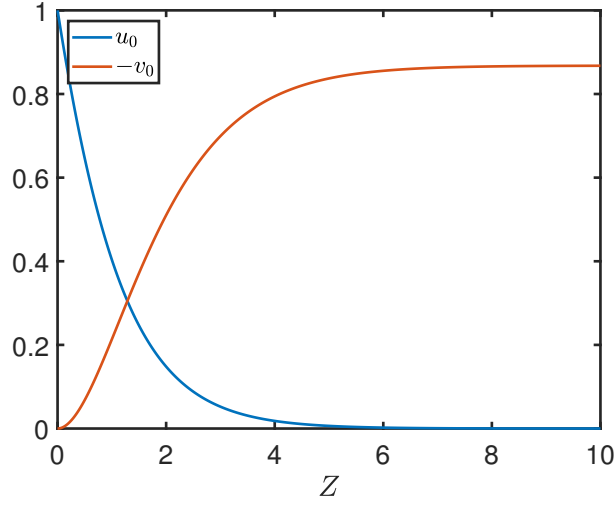


Figure 3.8: Plots of the streamwise and wall-normal velocity components for the case when $\gamma = 2$ and $U_w = \sqrt{{}_0U_w^2 + 2\xi/3} = \sigma$. In this case both u_0 and v_0 are independent of ξ . Given that no exact analytical solution for \hat{f} exists in the case when $\gamma = 2$, a shooting method that makes use of a fourth-order Runge-Kutta integrator, twinned with a secant root finding scheme, was employed to solve (3.17). As part of this solution process we determine that $\hat{f}''_{ZZ}(Z = 0) \approx 0.8300$, and that $\hat{f}(Z \rightarrow \infty) = \hat{f}_\infty \approx 1.0625$. In the limit as $Z \rightarrow \infty$, then $v_0 \rightarrow -\sqrt{2/3}\hat{f}_\infty$.

the base flow is then given by

$$\hat{f}'''_{ZZZ} + \hat{f}\hat{f}''_{ZZ} - \left(\frac{2}{2+\gamma}\right)(\hat{f}'_Z)^2 = 0. \quad (3.17a)$$

The case when $\gamma = -2$ is considered separately in Appendix B.2. The preceding ODE must be solved subject to

$$\hat{f}(Z = 0) = 0, \quad \hat{f}'_Z(Z = 0) = 1, \quad \hat{f}'_Z(Z \rightarrow \infty) \rightarrow 0. \quad (3.17b)$$

It is worth noting that (3.17) admits exact analytical solutions for two specific γ values. In the case when $\gamma = 0$, then $\hat{f} = 1 - e^{-Z}$, whilst when $\gamma = -4$, then $\hat{f} = \sqrt{2} \tanh(Z/\sqrt{2})$. A derivation of these solutions using a similar approach to those employed in Ackroyd [1] and Sachdev *et al.* [93] may be found in Appendix B.2. In what follows we will highlight three specific case studies that make use of these exact solutions and a numerical solution of (3.17), although we note that the choice of the value of the constant γ would, in practice, be informed by experimental conditions.

In order to verify the previous analysis we consider Crane's problem. Crane's problem corresponds to the linear stretching of a flat plate, as such, s is a constant and (3.14) reduces simply to $(U_w)'_\xi = K$. Thus when $K = 1$, and stipulating that $U_w(\xi = 0) = {}_0U_w = 0$, we recover the expected linear stretching result; $U_w = \xi$. In order to be able to visualise the solutions for both

u_0 and v_0 one needs to recall the unknown function g such that the similarity coordinate Z , and streamfunction ψ , can be written in terms of known functions. Irrespective of the value of γ we have that

$$g = \sqrt{\frac{2c_1\alpha\sigma U_w^{1+\gamma}}{K\xi}},$$

where

$$\alpha = \begin{cases} 1 & \text{when } \gamma = -1, \\ (1 + \gamma)(2 + \gamma)^{-1} & \text{when } \gamma \neq -1. \end{cases}$$

In order to ensure that g is solely real then, given that $c_1 > 0$, the constant K would have to be negative in the cases when $-2 < \gamma < -1$. Given the form of (3.15), with γ in this range and K being less than zero, one would then determine complex solutions for the wall velocity. Therefore, physical solutions are derived only in the cases when $\gamma < -2$, and $\gamma \geq -1$. For convenience we now fix K equal to unity but note that the following analysis holds for any $K > 0$. Having done so we determine that $\psi = \varsigma U_w \hat{f}(Z)$, where $Z = \eta/(\varsigma\sigma)$, and $\varsigma = \sqrt{2\alpha U_w^\gamma}$. Thus

$$\begin{aligned} u_0 &= \frac{\partial\psi}{\partial\eta} = \left(\frac{U_w}{\sigma}\right) \hat{f}'_Z, \\ v_0 &= -\frac{\partial\psi}{\partial\xi} = \frac{\varsigma}{2} \left\{ \left[\frac{2U_w\sigma'_\xi}{\sigma} + \gamma(U_w)'_\xi \right] Z \hat{f}'_Z - (2 + \gamma)(U_w)'_\xi \hat{f} \right\}. \end{aligned}$$

There is clearly a special case to consider when U_w is directly proportional to σ . In this case then both u_0 , and v_0/ς are functions of Z only. In addition to this, setting $\gamma = 2$, and fixing $U_w = \sigma$ ensures that $u_0 = \hat{f}'_Z$, and $v_0 = \sqrt{2/3}(Z\hat{f}'_Z - \hat{f})$, i.e., the wall-normal velocity is then identically independent of the streamwise coordinate ξ (see Fig. 3.8). Recalling (3.14) it must then transpire that $(U_w)'_\xi = 1/(3U_w)$. Thus, imposing the condition that the initial wall velocity is equal to ${}_0U_w$, then $U_w = \sqrt{{}_0U_w^2 + 2\xi/3} = \sigma$. Given this form for σ , and stipulating that $s(\xi = 0) = s_0$, it must therefore be the case that $s(\xi) = s_0 - ({}_0U_w^2 - 1)^{3/2} + ({}_0U_w^2 - 1 + 2\xi/3)^{3/2}$. Practically, it is perhaps unphysical to consider a case whereby the variation of the surface height of the plate is increasing in such a manner. However, given the preceding analysis we are now in a position to consider a number of cases that closely resemble physical boundary layer flows.

Surface Thinning

In order to capture the realistic thinning nature of a sheet that is being extruded from a cast die we fix s such that

$$s^*(\xi^*) = a_1^* e^{\xi^* - a_2^*}.$$

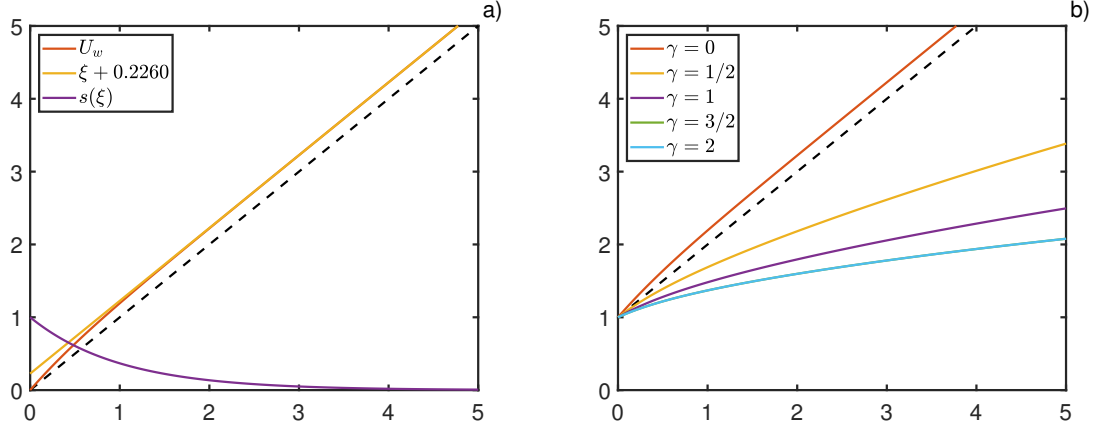


Figure 3.9: In (a) the wall velocity U_w , the approximate wall velocity $U_w^{\text{approx}} = \xi + 0.2260$, and the exponentially thinning sheet profile: $s(\xi) = e^{-\xi}$, are plotted against ξ . In (b) the wall velocity, given an identical thinning sheet profile, is plotted for a range of γ values. In both plots the dashed black line corresponds to the wall velocity result for a sheet undergoing linear stretching.

Given this form for s^* , we define our non-dimensionalising length scale L^* as the inlet height a_1^* , so that $s(\xi) = e^{a\xi}$, where $a = a_1^*/a_2^*$, and $\sigma = \sqrt{1 + a^2 e^{-2a\xi}}$, and

$$\mathcal{I} = \frac{\text{arcsinh}(a^{-1}e^{a\xi}) - \sigma}{a}.$$

Thus an analytical expression for U_w can be determined directly from (3.15). In practice one would choose the free constants (a, γ) such that the wall velocity profile matched closely with physical observations. In the absence of experimental data we are free to choose mathematically convenient values for these constants. If we set $a_1 = a_2 = \gamma + 1 = 1$, and stipulate that $U_w(\xi = 0) = {}_0U_w = 0$, then it follows that

$$U_w = \xi + \ln\left(\frac{1 + \sigma}{1 + \sigma_0}\right) + \sigma_0 - \sigma,$$

where, in this case, $\sigma_0 = \sigma(\xi = 0) = \sqrt{2}$. This expression for U_w is reasonably close to the result owing from Crane's linear stretching problem ($U_w = \xi$). Aside from the region close to $\xi = 0$, we find that U_w can be approximated in the following fashion

$$U_w^{\text{approx}} = \xi + \ln\left(\frac{2}{1 + \sigma_0}\right) + \sigma_0 - 1 \approx \xi + 0.2260.$$

This result, presented graphically in Fig. 3.9, is perhaps not surprising given that the sheet is thinning exponentially. As such, we would expect to recover a result for the wall velocity similar to that of Crane [23] in all regions where the plate is locally flat. However, we note

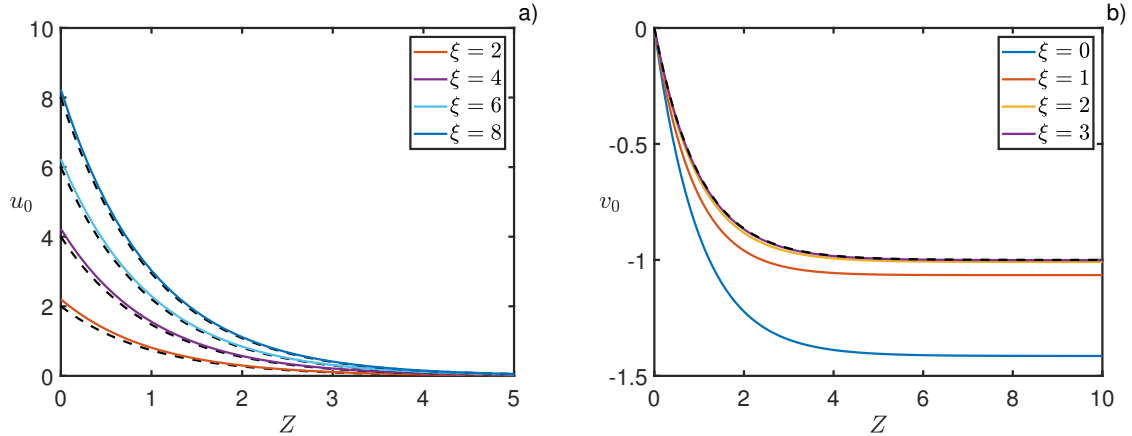


Figure 3.10: Plots of the streamwise (a), and wall-normal (b), velocity components for a range of ξ values. In this case the sheet is thinning exponentially: $s(\xi) = e^{-\xi}$. Crane's flat plate solutions are given by the dashed black curves.

that the analysis presented here is general enough that one could consider a plethora of different thinning sheet profiles dependent on the values of the constants a_1 and a_2 , or the rate of sheet acceleration depending on the value of γ .

The results presented in Fig. 3.10 show the discrepancy between the solutions obtained under the assumption of a flat stretching sheet when compared to those obtained under the correct assumption that the sheet will thin as it is accelerated and stretched. We observe that the streamwise velocity component is always under-predicted by Crane's model. Furthermore, near to the point where the sheet is being extruded, when $\xi = 0$, we observe that the gradient of the wall-normal velocity component is significantly shallower under assumption that the surface does not deform as it stretches. The disparity of these results at the surface of the sheet leads to a significant under-prediction of the magnitude of the flow that, via mass conservation, is directed towards the stretching surface. We note that these effects are exacerbated when the constant a_1 is held fixed and a_2 decreases in value, or, conversely, the constant a_2 is held fixed and a_1 increases in value. Similar qualitative results are obtained if one assumes that the sheet deforms in either a polynomial or a logarithmic manner.

Surface Thickening

Theoretical studies of textile compaction processes [61] have sought to model the stress within a fibre over a compaction relaxation-cycle. Here our aim is to propose a shape which captures the resulting reduction in volume fraction and hence determine a sheet velocity profile which facilitates a self-similar boundary layer solution for the ambient fluid. While this approach

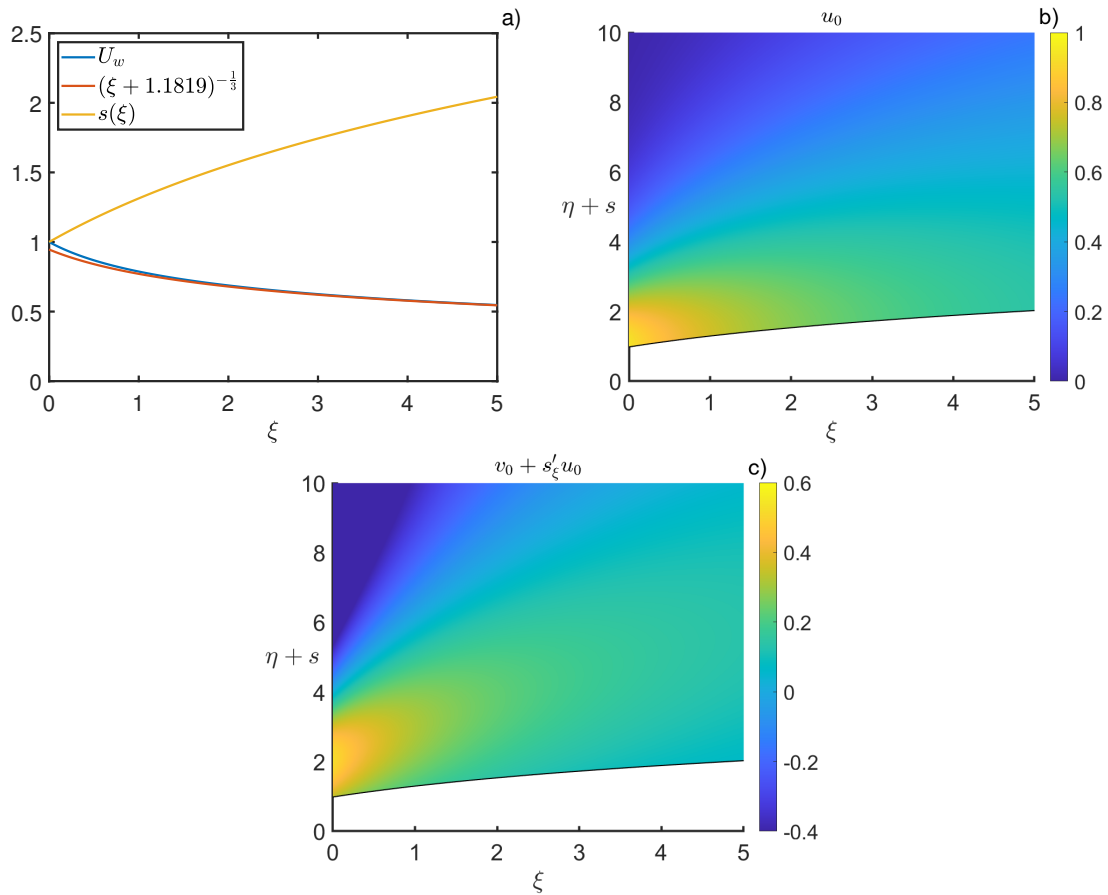


Figure 3.11: In (a) the wall velocity U_w , the approximate wall velocity $U_w^{\text{approx}} = (\xi + 1.1819)^{-\frac{1}{3}}$, and the logarithmically thickening sheet profile: $s(\xi) = \ln(e + \xi)$, are plotted against ξ . In (b) & (c), respectively, solutions for the streamwise velocity u_0 , and wall-normal velocity $v_0 + s'_\xi u_0$, are mapped back to the unscaled boundary-layer coordinate system $(\xi, \eta + s)$. The solid black line indicates the surface of the thickening decelerating sheet.

represents a simplification of the underlying physics governing such processes, it is warranted by the observed tendency of compaction-induced defects to manifest in textile manufacturing. These defects are commonly ascribed to micro-mechanical phenomena arising from the closure of interstitial gaps between individual fibres in a composite sheet, as described in Thompson *et al.* [106]. However, an examination of the stability characteristics of the induced boundary layer might provide insights into the potential mitigation of such defects.

If we consider a deforming surface with a profile defined as such, $s^*(\xi^*) = b_1^* \ln(e + \xi^*/b_2^*)$, where e is the exponential constant chosen such that $s^*(\xi^* = 0) = b_1^*$, then such a profile could be used to a thickening, decelerating surface such as those observed in compaction processes. We again set $L^* = b_1^*$, the initial sheet thickness, so that $s(\xi) = \ln(e + b\xi)$, with $b = b_1^*/b_2^*$. Irrespective of the value of b , in order to determine similarity solutions we first compute

$$\mathcal{I} = \frac{(e + b\xi)}{b} \sigma - \operatorname{arcsinh}(s'_\xi).$$

Here we choose the convenient parameter values $b = 1$, such that via (3.15) we have, for $\gamma \neq -1$, that

$$U_w = [C + (e + \xi)\sigma - \operatorname{arcsinh}(s'_\xi)]^{\frac{1}{1+\gamma}}.$$

Setting $\gamma = -4$, to ensure that the sheet is decelerating, and fixing the value of C such that ${}_0U_w = 1$, we have that

$$U_w = \left[\xi\sigma + \ln\left(\frac{1 + e\sigma_0}{s'_\xi + \sigma}\right) + e(\sigma - \sigma_0) \right]^{-\frac{1}{3}},$$

where, in this case, $\sigma_0 = \sigma(\xi = 0) = \sqrt{1 + e^{-2}}$. At first inspection, this expression for the wall velocity appears to be reasonably intricate. However, away from the region of the sheet inlet, this expression can be well approximated as follows

$$U_w^{\text{approx}} = [\xi + \ln(1 + e\sigma_0) + e(1 - \sigma_0)]^{-\frac{1}{3}} \approx (\xi + 1.1819)^{-\frac{1}{3}}.$$

Given that, in the case when $\gamma = -4$, we have an analytical solution for (3.17), with U_w calculated as above, we are then able to use our stream function definitions for u_0 and v_0 to visualise the flow in terms of the unscaled boundary-layer coordinate, $\zeta\sigma Z + s = \eta + s$. These results are depicted in Fig. 3.11 where we observe that both the streamwise and wall-normal fluid velocities are at a maximum in the vicinity of the inlet ($\xi = 0$). As one would expect, as both the curvature of the sheet and the velocity of the sheet decrease, the magnitude of these velocities also decreases.

3.3.2 Numerical Validation

The primary motivation for this study is the determination of boundary-layer flows induced by stretching surfaces, as presented in Section 3.3.1. As such, we chose to validate the analytical solutions presented in Figure 3.10 for the case of an exponentially thinning sheet against a suitable numerical scheme. To solve the governing system of PDEs numerically we use the finite element software FEniCS (Logg *et al.* [68]). It is convenient to rewrite our equations in terms of the divergence of the stress tensor $\boldsymbol{\tau}^*$, such that

$$\nabla^* \cdot \mathbf{u}^* = 0, \quad (3.18a)$$

$$\rho^*(\mathbf{u}^* \cdot \nabla^*)\mathbf{u}^* = \nabla^* \cdot \boldsymbol{\tau}^*. \quad (3.18b)$$

We apply the same coordinate system transformation and nondimensionalisation as before, with the exception that we scale the pressure by a factor of $\text{Re}^{1/2}$. This difference in the pressure scale can be attained by referring to (2.5c), where it is seen that the pressure term is $\mathcal{O}(\text{Re}^{1/2})$ larger than the next largest term in the η -momentum equation. This fact, twinned with the free stream boundary condition, $U_\infty = 0$, allowed us to deduce that pressure in the boundary layer was constant to leading order. However, rescaling our pressure as $p \sim \text{Re}^{-1/2}$, allows the pressure to vary and results in us being able to numerically determine the non-constant pressure correction. Note that this is in contrast to the corresponding flat stretching sheet analysis of Crane [23] where $p \sim \text{Re}^{-1}$, which would be the case in (2.5c) if $s'_\xi = 0$. Thus, we have that

$$\frac{\partial u}{\partial \xi} + \frac{\partial v}{\partial \eta} = 0, \quad (3.19a)$$

$$u \frac{\partial u}{\partial \xi} + v \frac{\partial u}{\partial \eta} = \left\{ \frac{\partial}{\partial \xi} - \text{Re}^{1/2} s'_\xi \frac{\partial}{\partial \eta} \right\} \tau_{\xi\xi} + \text{Re}^{1/2} \frac{\partial}{\partial \eta} \tau_{\xi\eta}, \quad (3.19b)$$

$$\begin{aligned} \text{Re}^{-1/2} \left(u \frac{\partial v}{\partial \xi} + v \frac{\partial v}{\partial \eta} \right) &= -s'_\xi \left(u \frac{\partial u}{\partial \xi} + v \frac{\partial u}{\partial \eta} \right) - s''_{\xi\xi} u^2 \\ &\quad + \text{Re}^{-1} \left\{ \frac{\partial}{\partial \xi} - \text{Re}^{1/2} s'_\xi \frac{\partial}{\partial \eta} \right\} \tau_{\xi\eta} + \text{Re}^{1/2} \frac{\partial}{\partial \eta} \tau_{\eta\eta}, \end{aligned} \quad (3.19c)$$

where the components of the stress tensor are given by

$$\tau_{\xi\xi} = -\text{Re}^{-1/2} p + 2 \text{Re}^{-1} \left(\frac{\partial u}{\partial \xi} - \text{Re}^{1/2} s'_\xi \frac{\partial u}{\partial \eta} \right), \quad (3.19d)$$

$$\tau_{\xi\eta} = + \text{Re}^{-1} \left\{ \text{Re}^{1/2} [1 - (s'_\xi)^2] \frac{\partial u}{\partial \eta} + \text{Re}^{-1/2} \frac{\partial v}{\partial \xi} + s'_\xi \left(\frac{\partial u}{\partial \xi} - \frac{\partial v}{\partial \eta} \right) + s''_{\xi\xi} u \right\}, \quad (3.19e)$$

$$\tau_{\eta\eta} = -\text{Re}^{-1/2} p + 2 \text{Re}^{-1} \left(\frac{\partial v}{\partial \eta} + \text{Re}^{1/2} s'_\xi \frac{\partial u}{\partial \eta} \right). \quad (3.19f)$$

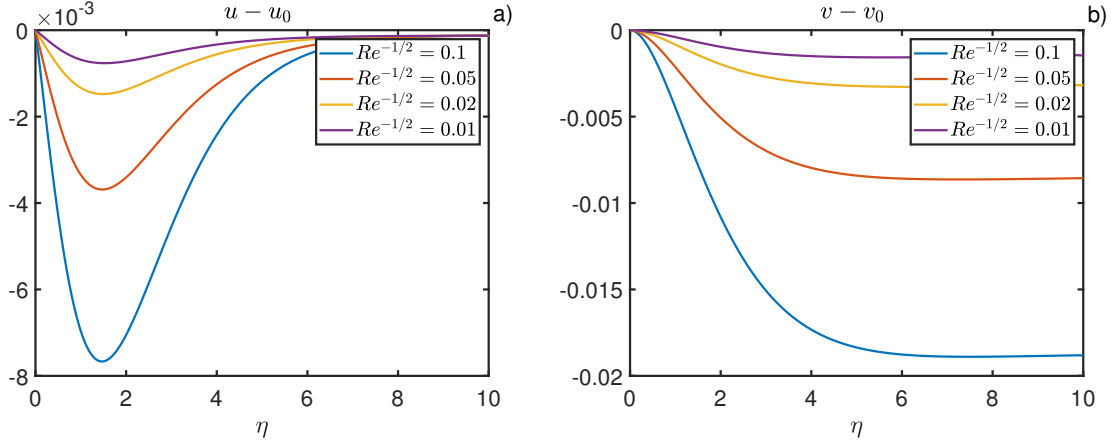


Figure 3.12: In (a) we plot the absolute value of the difference between the numerical solutions for the streamwise velocity component at $\xi = 2.5$, with the corresponding boundary-layer solution at the same point, for a range of values of the small parameter $Re^{-1/2}$. In (b) we plot an identical comparison for the wall-normal velocity component.

System (3.19) is then solved subject to the following boundary conditions

$$u = u_0|_{\xi=0, \xi_\infty}, \quad v = v_0|_{\xi=0, \xi_\infty}, \quad \text{at } \xi = 0 \quad \text{and} \quad \xi = \xi_\infty, \quad (3.20a)$$

$$u = U_w/\sigma, \quad v = 0, \quad \text{at } \eta = 0, \quad (3.20b)$$

$$u = 0, \quad \boldsymbol{\tau} \cdot \mathbf{n} = 0, \quad \text{at } \eta = \eta_\infty. \quad (3.20c)$$

We apply our normal and tangential velocity conditions at the wall and the condition that the streamwise velocity component decays in the far field, as per the solution of our boundary layer equations (2.7). In solving the full Navier-Stokes equations we need to impose additional constraints on the system. Here we use our boundary-layer solutions as inlet and outlet conditions. We also impose a no stress condition at the outlet. This choice of free stream condition allows us to measure convergence by means of evaluation of the wall-normal velocity component at the far-field, $v_0|_{\eta=\eta_\infty}$, for any fixed ξ , since we have not explicitly forced this value. Indeed, this can be seen in Figure 3.12, where the difference in the absolute value between the boundary-layer and numerical wall-normal velocity solutions decrease as the Reynolds number grows larger. In the transformed coordinates our boundary-layer solutions are given by

$$u_0 = \frac{U_w}{\sigma} e^{-\eta/\sigma},$$

$$v_0 = \frac{U_w \sigma'_\xi}{\sigma^2} \eta e^{-\eta/\sigma} - (U_w)'_\xi (1 - e^{-\eta/\sigma}).$$

It is these solutions that we compare, respectively, to the numerical results for u and v . The domain $[\xi, \eta] \in [0, 5] \times [0, 10]$ was triangulated using a 200×200 mesh with the originally

uniformly spaced mesh mapped via

$$\eta_{\text{new}} = \eta \frac{\exp(\eta/\eta_\infty) - 1}{\exp(1) - 1},$$

to accurately resolve the boundary layer near the surface of the sheet. To ensure the mesh was properly resolved the problem was also solved on a 100×100 and 50×50 mesh, with $|v - v_0|_{\eta=\eta_\infty}$, at $\xi = 2.5$, being used to measure the errors for a range of different mesh densities and Reynolds numbers. The errors were determined to be a function of the size of the Reynolds number with the mesh density playing almost no role at all, giving us confidence that our mesh is sufficiently refined.

The choice of η_∞ was further validated by solving the problem on incrementally larger domains, where it was found that $\eta_\infty = 10$, was appropriate provided the Reynolds number was sufficiently large. Plots comparing the difference between our self-similar and finite element solutions are presented in Figure 3.12 for a range of Reynolds numbers. Given that our boundary-layer analysis hinges on an asymptotic expansion with small parameter $\text{Re}^{-1/2}$, it is logical for us to present results for a range of values of this small quantity. As expected we observe that the difference between the large Reynolds number analytical solutions and the numerical solutions decreases as the Reynolds number increases.

In Figure 3.13 we present a comparison of the boundary-layer and finite element solution for the streamwise velocity component across the entire $(\xi, \eta + s)$ domain. It is clear that our analytical boundary-layer solutions provide an excellent approximation to the full numerical solutions. Indeed, upon decreasing our small parameter $\text{Re}^{-1/2}$, one observes a notable decrease in the absolute difference between the two sets of solutions. These values correspond to $\text{Re} = 400, 625$ respectively which is roughly 1.5 times increase in Reynolds number. This allows us to view errors on the same scale so that improved agreement could be readily observed without being "too small" as would be the case in the $\text{Re} \rightarrow \infty$ limit.

3.4 Discussion and Conclusions

We have shown that the inclusion of the effects of a temperature gradient between the sheet and the free stream changes the dynamics for Crane's flow. The most prominent change being that we no longer have exact analytical solutions for the basic flow profiles. For the remainder of this thesis we use the inverse viscosity distribution described above. This is done for two reasons. First it allows us to more readily compare with the stability results of Miller *et al.* [77], and since we can easily interpret the role of the sensitivity parameter m , with positive values of m describing the viscothermal behaviour of a liquid and negative value that of a gas. Here we observed the entrainment of the boundary layer as the value of the sensitivity parameter

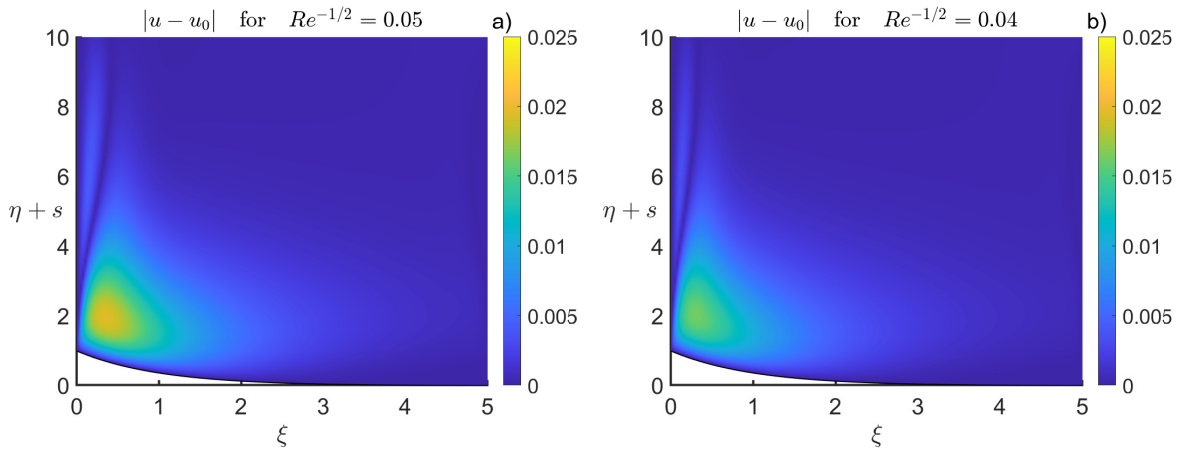


Figure 3.13: Comparison between the finite element and boundary-layer solutions across the computational domain for (a) $Re^{-1/2} = 0.05$, and (b) $Re^{-1/2} = 0.04$. The same colourbar scale is used in both instances so that the reduction in error may be easily observed.

m was increased. In this case we were also able to attain reasonable near wall approximation of the flow quantities of interest for weak temperature dependence ($m \ll 1$). Though similar approximation could be derived for other viscosity distributions. In the stability analysis which follows we will show that this is the most important region for describing the dispersion relation on the lower branch at leading order.

Dissipative effects on the other hand, lead to a change in the structure of the basic flow solutions, wherein we can no longer assume that the temperature field is independent of the streamwise location, and requires a full solution of the system of boundary layer PDEs to be properly resolved. This has important implication for the stability analysis which follows as it prohibits the use of our parallelisation approach when the momentum and energy equations are coupled.

We have also shown that it is possible to obtain self-similar boundary-layer solutions over deforming surfaces and have investigated a number of specific case studies. Our analysis is primarily focused on flows that are generated from extrusion-type processes, whereby surfaces accelerate and thin as they are extruded. The vast majority of studies in the literature fail to account for this surface curvature and instead assume that the sheet is flat, following the analysis of Crane [23]. We show that in order to accurately describe boundary layer flows over stretching surfaces one needs to account for the curvature of the surface. Failing to do so results in incorrect predictions for both the streamwise and wall-normal velocity components. Most notably, near to the extrusion inlet, we find that the magnitude of the wall-normal velocity at the far-field is significantly increased when compared to the corresponding flat-plate results. Our analytical results have been verified numerically using an appropriate finite element scheme and we observe excellent agreement between the two sets of solutions.

Our formulation has been shown to be general enough that it can be extended to consider both flows over thickening, decelerating surfaces and also the development of boundary-layer flows over periodic rough surfaces, (see [45]). Our analysis stipulates that the exact form of the wall velocity is dictated by the shape of the deforming surface. However, we have shown that, at least for the case studies considered here, these expressions for the wall velocity can be very well approximated by simple expressions involving only the streamwise coordinate ξ . In practice, one would measure the velocity of the deforming sheet and stipulate the value of the constant γ to ensure that the predicted wall velocity closely matched experimental observations, and, indeed, our analysis allows for exactly this procedure. This would involve finding the value of γ , along with the integration constants which minimised the difference between experimental data (obtained from say PIV) and the basic flow profiles predicted by our model. Our analysis could easily be extended to consider other types of flows generated from extrusion processes including those over bounded domains. In these cases, one would replace the analytical calculation of the arc length of the surface, \mathcal{I} , with a numerical integration scheme with the limits of integration dictated by the bounds of the domain.

In a sense our deforming analysis is somewhat related to that of Crane [24], where similarity solutions for the boundary-layer flow induced by a stretching cylinder were derived. However, these solutions are only valid when the ratio of cross-sectional areas of the boundary layer to the cylinder is large. Both the velocity and shape of the cylinder are prescribed in a manner that ensures that mass is conserved within the cylinder i.e. the density is constant. In much the same way as the corresponding flat plate study of Crane [23] the cylinder wall is not treated as a deformable quantity. The approach we have presented here would be capable of describing more general boundary-layer solutions in other such non-Cartesian geometries, and, as such, could remove the limitations of the studies relating to flows induced by stretching cylinders.

Chapter 4

Numerical Linear Stability Analysis

In this Chapter, we present solutions to the quadratic eigenvalue problem that arises from the linearised Navier-Stokes and energy equations for the temperature-dependent extension of Crane's problem. We demonstrate that the dependence of viscosity on temperature can significantly alter the stability characteristics of the flow. In the most extreme case considered, the Reynolds number at which instabilities occur is approximately halved compared to the isothermal case. This analysis is complemented by both an integral energy analysis and an Orr-Sommerfeld comparison, where we evaluate the relative importance of the terms arising from surface stretching and the additional terms due to the temperature dependence of viscosity. Note that the analysis in Sections 4.2 and 4.3 has been submitted in the publication Hanevy *et al.* [46], which is under review.

4.1 Introduction

The classical approach in hydrodynamic stability has been to consider the evolution of small perturbations to a two-dimensional parallel basic flow of the form $\mathbf{u} = (u_B(y), 0)$, where u is the streamwise velocity component and y the wall normal spatial coordinate. The two-dimensional problem is chosen as according to Squire's theorem any unstable three-dimensional mode, may be recast as a two-dimensional mode at a lower Reynolds number. Flow quantities are then perturbed assuming a normal mode form for the perturbations such that the streamwise velocity component U , for example may be written as follows

$$U = u_B + \epsilon \tilde{u}, \quad \tilde{u} = \hat{u}(y)e^{i(\alpha x - \omega t)},$$

where α , ω and \hat{u} are in general complex and $\epsilon \ll 1$. Substituting the above Fourier ansatz into the Navier-Stokes equations, and gathering terms of $\mathcal{O}(\epsilon)$ results in an eigenvalue problem

where typically the Reynolds number R , and either the streamwise wavenumber α or temporal wavenumber ω are fixed and assumed to be real. The stability of the flow is determined by the complex eigenvalues of the system. The flow is said to be temporally stable if α is fixed to be real and $\omega_i > 0$ and spatially unstable if ω is fixed to be real and $\alpha_i < 0$. Where the subscripts ‘r’ and ‘i’ are used to denote the real and complex part of the wavenumber and frequency, so that $\alpha = \alpha_r + i\alpha_i$ for example. From a physical standpoint, the distinction between temporal and spatial instabilities comes down to whether the perturbations are imposed through initial or boundary conditions. Temporal instabilities arise when the initial state of the system is perturbed whereas spatial instabilities are forced by the imposition of appropriate boundary conditions. For instance blowing and suction boundary conditions are often used in numerical simulations and experiments to induce the Tollmein-Schlichting instabilities considered later in this Chapter. In imposing the normal mode form for the perturbations we are assuming that the perturbations are periodic either in space or in time. This means that depending on the flow regime in question, either the spatial or temporal formulation may be more physically relevant. It should be noted that this approach is intended to describe only the early stages of transition and breaks down as the perturbations grow sufficiently large and cause distortion of the mean flow.

For parallel flows such as plane Poiseuille or Couette flow, the temporal stability problem has been found to be most relevant as disturbances tend to grow in time and are spatially periodic. In this case we need to solve a generalised eigenvalue problem, for the disturbance frequency ω of the form

$$(\mathbf{A} - \omega\mathbf{B})\hat{\mathbf{q}} = 0.$$

Here \mathbf{A} and \mathbf{B} are the operators which arise through discretisation of the linearised Navier-Stokes equations and $\hat{\mathbf{q}}$ is a vector of the disturbance velocities and pressure. In our case we are interested in a boundary layer problem. Boundary layers emerge in a high Reynolds number flow in the presence of a solid boundary, where viscous effects are required to satisfy no slip conditions on the solid boundary and match with the outer inviscid flow. Boundary layer flows are not parallel and need to be parallelised by exploiting the fact that the flow varies much more rapidly in the wall normal, rather than the streamwise direction to perform the analysis. A consequence of the inhomogeneity in the streamwise direction is that the spatial rather than the temporal problem is more relevant to boundary layer flow since disturbances are found to grow as they are convected downstream. Here we solve a quadratic eigenvalue for the streamwise wavenumber α

$$(\alpha^2\mathbf{A}_2 + \alpha\mathbf{A}_1 + \mathbf{A}_0)\hat{\mathbf{q}} = 0.$$

Here too, \mathbf{A}_i are operators of the discrete linearised Navier-Stokes equations. Regardless of whether the temporal or spatial eigenvalue problem is solved, the goal is to locate the neutral stability curve. That is the curve in the (R, α) or (R, ω) plane, where perturbations neither grow nor decay, *i.e.* $\alpha_i = \omega_i = 0$. Doing so provides an estimate of regions of instability which can be

validated through asymptotic, numerical or experimental means.

For the flow under consideration, namely the temperature dependent extension of Crane’s flow, our analysis lies somewhere between the analysis of a flat plate boundary layer discussed in [77] and the stability of a rotating disk boundary layer as explored in [78]. It resembles the flat plate boundary layer since we are dealing with a two-dimensional Cartesian boundary layer problem, and the rotating disk, as parallelisation is achieved by defining a local Reynolds number R which is equivalent to the dimensionless streamwise location. In the rotating disk problem, the use of this parallel flow approximation results in a system of equations where terms associated with Coriolis forces and streamline curvature are $\mathcal{O}(R^{-1})$. Initially these terms were neglected as they do not appear in the standard Orr-Sommerfeld equation. An example of this is found in the calculations of Cebeci and Stewartson [19], where a critical Reynolds number of approximately 180 was reported. Inclusion of these higher order terms acts to stabilise the flow as evidenced by the calculations in Malik *et al.* [73] and validated by the hot wire experiments of Kobayashi *et al.* [64], both reporting a critical Reynolds number of approximately 290. These “extra” terms which arise through the parallelisation of the base flow also qualitatively change the structure of the neutral curve, introducing a kink appearing on the lower branch when they are accounted for. Due to improved agreement with experimental results in the rotating disk case, we also choose to include them in the analysis of the stretching sheet.

4.2 Numerical Formulation

In this Section, we assess the stability of the boundary layer flow discussed above through the numerical solution of the linearised Navier-Stokes equations. Due to the variations in base flow resulting from changes in the sensitivity parameter, the analysis differs somewhat from the isothermal analysis by Griffiths *et al.* [39]. The primary difference is that the boundary layer thickness is not constant and varies with the sensitivity parameter m . To account for this, we adopt an alternative set of scales compared to the previous Chapter. The outcome of our new set of scales is that the wall-normal coordinate is scaled by the boundary layer thickness. This adjustment will need to be considered in the asymptotic analysis in the next Chapter when comparing our asymptotic and numerical results.

4.2.1 Numerical Linear Disturbance Equations

To derive the linear stability equations we start by taking the dimensional extension of Crane’s model (2.1) in the absence of viscous dissipation. Here we non-dimensionalise by introducing

the following set of scales

$$\mathbf{U}^* = a^* x_s^* \mathbf{U}, \quad t^* = \frac{\delta^*}{x_s^* a^*} t, \quad (4.1)$$

$$p^* = \rho^* a^{*2} x_s^{*2} p \quad (x^*, y^*) = \delta^*(x, y). \quad (4.2)$$

Where the temperature and viscosity scales are as before. The stability analysis is performed at streamwise location x_s^* . This leads to the definition of a local Reynolds number $R = \rho^* x_s^* a^* \delta^* / \mu_\infty^* = x_s^* / \delta^* = x_s$ which is equivalent to the dimensionless streamwise location. Assuming two-dimensional disturbances, mean flow quantities are then perturbed as follows

$$u = \frac{x_s}{R} u_B(y) + \bar{u}(x, y, t), \quad (4.3a)$$

$$v = \frac{1}{R} v_B(y) + \bar{v}(x, y, t), \quad (4.3b)$$

$$p = \frac{1}{R^2} p_B(y) + \bar{p}(x, y, t), \quad (4.3c)$$

$$T = T_B(y) + \bar{T}(x, y, t), \quad (4.3d)$$

$$M = M_B + \bar{M}, \quad (4.3e)$$

where the perturbations are assumed to be small and have normal mode form

$$(\bar{u}, \bar{v}, \bar{w}, \bar{p}, \bar{T}) = [\hat{u}(y), \hat{v}(y), \hat{p}(y), \hat{T}(y)] e^{i(\alpha x - \omega t)},$$

and the wall normal coordinate is scaled to account for the variation of the boundary layer thickness such that $y \sim \delta^{-1}$. The basic solutions satisfy (3.2) for a given value of the sensitivity parameter m . Our viscosity function is perturbed using a binomial expansion as follows

$$\begin{aligned} M &= [1 + m(T_B + \bar{T})]^{-1}, \\ &= \frac{1}{1 + mT_B} \left(1 + \frac{m\bar{T}}{1 + mT_B} \right)^{-1}, \\ \implies M_B &= \frac{1}{1 + mT_B}, \quad \bar{M} = -\frac{m\bar{T}}{(1 + mT_B)^2}. \end{aligned}$$

The linear perturbation equations are

$$i\alpha\hat{u} + \hat{v}' = 0, \quad (4.4a)$$

$$i(\alpha u_B - \omega)\hat{u} + \frac{1}{R}(u_B\hat{u} + v_B\hat{u}') + u'_B\hat{v} + i\alpha\hat{p} - \frac{2i\alpha}{R^2}u_B\hat{M}, \quad (4.4b)$$

$$- \frac{1}{R} \left[M_B(\hat{u}'' - \alpha^2\hat{u}) + (\hat{M}u'_B)' + M'_B(i\alpha\hat{v} + \hat{u}') \right] = 0,$$

$$i(\alpha u_B - \omega)\hat{v} + \frac{1}{R}(v_B\hat{v})' + \hat{p}' - \frac{2}{R} \left(M'_B\hat{v}' + \frac{1}{R}v'_B\hat{M}' \right) - \frac{1}{R} \left[M_B(\hat{v}'' - \alpha^2\hat{v}) + \frac{1}{R}v''_B\hat{M} + i\alpha u'_B\hat{M} \right], \quad (4.4c)$$

$$i(\alpha u_B - \omega)\hat{T} + \frac{1}{R}v_B\hat{T}' + T'_B\hat{v} - \frac{1}{PrR}(\hat{T}'' - \alpha^2\hat{T}) = 0. \quad (4.4d)$$

The above system of coupled ODE's can be written as follows

$$(\alpha^2 \mathbf{A}_2 + \alpha \mathbf{A}_1 + \mathbf{A}_0) \mathbf{Q} = \mathbf{0}, \quad (4.5a)$$

where $\mathbf{Q} = (u, v, T, p)^T$ and is solved subject to the following boundary conditions

$$\hat{u} = \hat{v} = \hat{v}' = \hat{T} = 0 \quad \text{at } y = 0, \quad (4.5b)$$

$$\hat{u} \rightarrow \hat{v} \rightarrow \hat{p} \rightarrow \hat{T} \rightarrow 0 \quad \text{as } y \rightarrow \infty. \quad (4.5c)$$

These boundary conditions ensure that perturbations are zero at the solid boundaries and decay as the free stream is approached as indicated by the arrow notation. The Neumann condition on the wall normal perturbation velocity arises through the continuity equation, while we only have a single boundary condition on the perturbation pressure as it only appears to first order. The system (4.5), was discretised using a chebychev collocation scheme and the associated quadratic eigenvalue problem was solved using Matlab's `polyeig` function. Details of the numerical scheme are given in the appendix C. The definition of the operators in (4.5) is as follows

$$\mathbf{A}_2 = \frac{1}{R} \begin{bmatrix} M_B & 0 & 0 & 0 \\ 0 & M_B & 0 & 0 \\ 0 & 0 & Pr^{-1} & 0 \\ 0 & 0 & 0 & 0 \end{bmatrix} \quad \mathbf{A}_1 = i \begin{bmatrix} u_B & -\frac{M'_B}{R} & -\frac{2}{R^2}u_B\hat{M} & 1 \\ 0 & u_B & -\frac{1}{R}u'_B\hat{M} & 0 \\ 0 & 0 & u_B & 0 \\ 1 & 0 & 0 & 0 \end{bmatrix} \quad \mathbf{A}_0 = \begin{bmatrix} A_{011} & u'_B & A_{013} & 0 \\ 0 & A_{022} & A_{023} & \mathcal{D} \\ 0 & T'_B & A_{033} & 0 \\ 0 & \mathcal{D} & 0 & 0 \end{bmatrix}$$

where \mathcal{D} denotes differentiation with respect to y and the non zero coefficients of \mathbf{A}_0 are

$$\begin{aligned} A_{011} &= -i\omega + \frac{1}{\text{R}} (u_B + v_B \mathcal{D} - M_B \mathcal{D}^2 - M'_B \mathcal{D}), \\ A_{013} &= -\frac{1}{\text{R}} (u'_B \hat{M})', \\ A_{022} &= -i\omega + \frac{1}{\text{R}} (v'_B + v_B \mathcal{D} - 2M'_B \mathcal{D} - M_B \mathcal{D}^2), \\ A_{023} &= -\frac{1}{\text{R}^2} (2v'_B \hat{M}' + v''_B \hat{M}), \\ A_{033} &= -i\omega + \frac{1}{\text{R}} v_B \mathcal{D} - \frac{1}{\text{R Pr}} \mathcal{D}^2. \end{aligned}$$

The results are shown in Figure 4.1. From the plots we can see that reducing the value of the sensitivity parameter reduces the Reynolds number and destabilises the flow. Although the Reynolds numbers remain high, this still suggests potential impacts on industrially relevant flows, as negative values of the sensitivity parameter are characteristic of gas-type viscothermal behaviour. The critical values found at the range of sensitivity values tested are presented in table 4.1. As can be seen from the table, and also in Figure 4.1 c), there is a narrow range of positive values of m which stabilise the flow before the critical Reynolds number again decreases.

In d) we plot the growth rates bounded by the upper and lower branches of the neutral stability curves at $\text{R}_{\text{crit}} + 5000$. The energy analysis of the following Section is performed at the value of ω which maximises this growth rates from this plot. As seen in the plots the maximum growth rates for the $m = -0.4$ is triple that of the other cases. This occurs since our increment represents a larger proportion of the critical Reynolds in this particular case. We could alternatively analyse the energy equations at some multiple of the critical Reynolds number. However, as will be seen, our choice of increment does not effect our energy analysis and allows us to uncover the cause of the destabilisation of the flow for $m > 0.34$.

In an industrial setting our critical Reynolds number would correspond to distance along the stretching axis before instabilities arise. If such instabilities were to lead to manufacturing defects, through coupling with the constitutive equations of the sheet, then any intervention which delays the onset of these instabilities could reduce manufacturing costs. Given the largeness of the Reynolds numbers and the simplicity of the model used, our results are unlikely to directly correspond to any physical system. It is however probable that should additional physical effects be incorporated, the stabilising role of gaseous viscosity distributions could be exploited to suppress instabilities.

In order to validate our numerical scheme we compare our solutions in the uncoupled $m = 0$ case to the isothermal analysis in [39]. These results are shown in the last row of table 4.1. While there is a discrepancy between the two results, there are a number of differences between our

Table 4.1: Critical values for Crane’s viscothermal extension

m	R_{crit}	α_{crit}	ω_{crit}
-0.4	18342	0.17976	0.14161
-0.2	39160	0.16021	0.13299
0	48494	0.1602	0.13541
0.2	49788	0.16424	0.1399
0.4	47681	0.1681	0.14374
Griffiths <i>et al.</i> [39]	48499.1	0.1614	0.1364

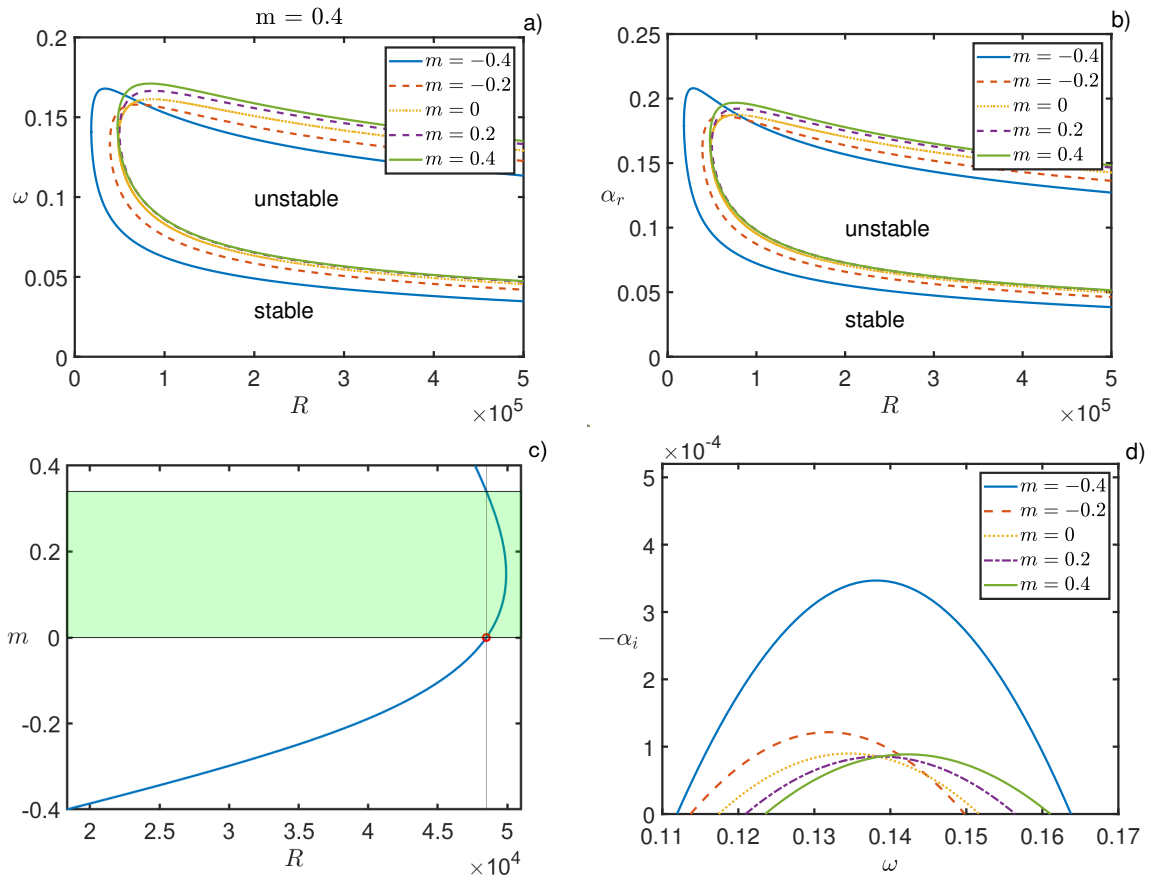


Figure 4.1: a) Neutral stability curve plotted against the frequency ω and b) the corresponding plot for the real part of the streamwise wavenumber α , for a range of values of the sensitivity parameter m . In c) the variation of the critical Reynolds number with m is shown. The shaded region indicates the range of values of m for which the flow is stabilised. d) shows the growth rates for each value of m at $R_{crit} + 5000$.

calculations. The first being that we are using numerical approximations instead of the exact analytical solutions for the isothermal problem. This is done so that our scheme is consistent when $m \neq 0$. The second being the inclusion of the energy equation. This should not impact the stability of the system since the equations are not coupled. The other key difference is the algorithm used to compute the neutral curves. In Griffiths *et al.* [39], the neutral point is found by locating the lowest Reynolds number for which $\alpha_i < 0$. In contrast the current calculations adopt an arclength continuation scheme as detailed in Morgan [79], whereby a point is deemed to be neutrally stable if $|\alpha_i| < 10^{-7}$. This change in stability criterion explains why we predict a slightly smaller critical Reynolds number.

There are also differences in the type of Chebychev scheme employed. In Griffiths *et al.* [39], the scheme was set up to solve for expansion coefficients, whereas the current analysis solves for values at the collocation points. In addition, an algebraic rather than an exponential map was employed to map the Chebychev domain to the physical domain. Full details of the discretisation scheme may be found in Appendix C. The reason the new scheme was adopted is that the eigenvectors calculated for the energy analysis are better behaved. The expansion coefficient scheme led to oscillations in the appearing in the eigenfunctions. With those differences noted, the fact that our critical values are in broad agreement indicates that the our current scheme is properly resolved. This will be further validated by the asymptotic analysis in the next Chapter.

Given the number of assumptions made in deriving these results, any critical Reynolds number quoted is unlikely to directly correlate with a fully nonlinear regime either numerically or experimentally. Therefore the goal of our numerical analysis is to predict trends induced by the variance of the sensitivity parameter rather than indicate the exact location at which transition would be observed. With that goal achieved we now seek to understand cause of these trends via the integral energy analysis.

4.3 Energy Analysis

The aim of this Section is to understand how the addition of temperature effects impacts the stability of the system by considering the system's energy balance. We will also use this analysis to explain the narrow range of stabilising values of the sensitivity parameter. This type of analysis has been used extensively in the literature for a range of different "parallel" boundary layer flows (see ([17],[21],[77])). It is based on the Reynolds-Orr equation for the disturbance kinetic energy as discussed by Schmid and Henningson [97]. The advantage of this analysis is that it allows for a physical interpretation of the role of the various terms in the linearised momentum equations to understand how disturbances may be damped or amplified.

To derive a set of energy balance equations we begin by multiplying our streamwise and wall

normal perturbation equations by \bar{u} and \bar{v} respectively and sum the result to obtain

$$\begin{aligned}
& \left(\frac{\partial}{\partial t} + u_B \frac{\partial}{\partial x} \right) \bar{e} + u'_B \bar{u}\bar{v} + \frac{1}{R} [u_B(\bar{u}^2 - \bar{v}^2) + v_B(\bar{u}\bar{u}' + \bar{v}\bar{v}')] \\
& + \frac{\partial}{\partial x}(\bar{u}\bar{p}) + \frac{\partial}{\partial y}(\bar{v}\bar{p}) - \frac{\mu_B}{R} \left(\frac{\partial}{\partial x}(\bar{v}\bar{q}) - \frac{\partial}{\partial y}(\bar{u}\bar{q}) - \bar{q}^2 \right) \\
& - \frac{1}{R} \left\{ \mu'_B \left[\frac{\partial}{\partial x}(\bar{u}\bar{v}) + \frac{\partial}{\partial y}(\bar{e} + \bar{v}^2) \right] + u'_B \left[\frac{\partial}{\partial y}(\bar{\mu}\bar{u}) + \frac{\partial}{\partial x}(\bar{\mu}\bar{v}) - \bar{\mu}\bar{s} \right] + u''_B \bar{\mu}\bar{u} \right\} \\
& - 2 \frac{u_B}{R^2} \left[\bar{u} \frac{\partial \bar{\mu}}{\partial x} - \bar{v} \bar{\mu}' \right] = 0.
\end{aligned} \tag{4.6}$$

where $\bar{e} = (\bar{u}^2 + \bar{v}^2)/2$ is the kinetic energy, $\bar{q} = \frac{\partial \bar{v}}{\partial x} - \frac{\partial \bar{u}}{\partial y}$, is the disturbance vorticity and $\bar{s} = \frac{\partial \bar{v}}{\partial x} + \frac{\partial \bar{u}}{\partial y}$, is defined for convenience. Using the normal mode form of the perturbations, the above equations are averaged over a single time period and integrated through the boundary layer to attain

$$\begin{aligned}
& -2\alpha_i \int_0^\infty u_B \langle \hat{e} \rangle + \langle \hat{u}\hat{p} \rangle dy \\
& = - \underbrace{\left\{ \int_0^\infty u'_B \langle \hat{u}\hat{v} \rangle dy \right\}}_I - \frac{1}{R} \underbrace{\left\{ \int_0^\infty 2\alpha_i \mu_B \langle \hat{v}\hat{q} \rangle + \mu_B \langle \hat{q}^2 \rangle dy \right\}}_{II} \\
& + \frac{1}{R} \underbrace{\left\{ \int_0^\infty \mu'_B \langle \hat{u}\hat{q} \rangle - \mu''_B \langle \hat{e} + \hat{v}^2 \rangle - u'_B \langle \hat{\mu}\hat{s} \rangle dy - 2\alpha_i \int_0^\infty \mu'_B \langle \hat{u}\hat{v} \rangle + u'_B \langle \hat{\mu}\hat{v} \rangle dy \right\}}_{III} \\
& + \underbrace{\left\{ \frac{1}{R^2} \int_0^\infty 2u_B (\langle \alpha \hat{u}\hat{\mu} \rangle - \langle \hat{v}\hat{\mu}' \rangle) dy - \frac{1}{R} \int_0^\infty u_B (2\langle \hat{u}^2 \rangle - \langle \hat{e} \rangle) dy \right\}}_{IV}.
\end{aligned} \tag{4.7}$$

The terms labelled above represent energy production due to Reynolds stresses (EPRS-I), energy dissipation due to viscosity (EDV-II), additional terms due to variable viscosity (AVV-III), and extra terms due to surface stretching (ESS-IV) respectively. The above energy formulation may be compared with that presented in Miller *et al.* [77] for temperature dependent Blasius flow, with the only difference being the additional terms from the surface stretching. Numerical investigations, as demonstrated in Table 4.2 where we integrate the overall energy balance of the system, reveals that the above integral energy equation may be approximated as follows

$$\begin{aligned}
-2\alpha_i & = \mathcal{I} \approx - \underbrace{\int_0^\infty \langle \hat{u}\hat{v} \rangle u'_B dy}_I - \underbrace{\frac{1}{R} \int_0^\infty u_B (2\langle \hat{u}^2 \rangle - \langle \hat{e} \rangle) dy}_{IV_a} \\
& - \underbrace{\frac{1}{R} \int_0^\infty \mu_B \langle \hat{q}^2 \rangle dy}_{II_a} + \underbrace{\frac{1}{R} \int_0^\infty \mu'_B \langle \hat{u}\hat{q} \rangle - \mu''_B \langle \hat{e} + \hat{v}^2 \rangle - u'_B \langle \hat{\mu}\hat{s} \rangle dy}_{III_a},
\end{aligned} \tag{4.8}$$

Table 4.2: Check for energy analysis. Column 3 showing the difference in absolute errors from approximating terms II – IV in (4.7) using equation (4.8)

m	$ \frac{-2\alpha_i}{\mathcal{I}} - 1 \times 10^{-3}$	$ \frac{-2\alpha_i}{\mathcal{I}_a} - 1 \times 10^{-3}$
-0.4	0.1191	0.1189
-0.2	0.2100	0.2093
0	0.0047	0.0047
0.2	0.2122	0.2120
0.4	0.3439	0.3437

where the right hand side of (4.8) has been normalised by the integral of the combination of the energy flux and the work done by pressure. The subscripts ‘a’ denote that terms II-IV have been approximated by the omission of terms whose absolute value is negligably small in each of the cases considered. The energy analysis is performed at $R_c + 5000$ from table 4.1, which is roughly 10% the critical Reynolds number in the isothermal case, and at the value of ω which maximises the growth rate $-\alpha_i$ as seen in Figure 4.1 d). We can easily validate our formulation checking that the total mechanical energy of the system $-2\alpha_i$ balances with the energy integral. This is shown in table 4.2 where we also show the ratio of the total mechanical energy to the right had side of (4.7) is approximately one. The approximate integral equations were derived by noting that this ratio remained largely ratio unchanged by the omission of terms for each of the cases studied.

Before examining the role of each of the energy production terms for various values of m , we first examine the corresponding eigenfunctions. These are shown in Figure 4.2, where we plot the absolute value of the streamwise, wall normal and temperature eigenfunctions for various values of m . We see that the maximum absolute value of \hat{u} increases monotonically with increasing values of m , while the opposite is true of the \hat{T} . The maximum absolute value of \hat{v} appears to be minimised for $m \approx -0.2$ and increases for both increasing and decreasing m . While it is difficult to draw conclusions regarding the flow stability directly from the shape of the eigenfunctions alone, their overall contributions become clearer when we isolate the relative terms in our energy balance equations.

In Figure 4.3 a), we show the relative contribution to the overall energy of the system of each of the terms in equation (4.8). While some of the additional stretching and viscosity terms (ESS - IV_a and AVV - III_a) were required to quantitatively improve the overall energy balance of the system, it is clear from this Figure that their contribution is far less pronounced than that of the terms found in the standard analysis (EPRS - I and EDV - II_a). This is consistent with the energy analysis of the temperature dependent Blasius problem in Miller *et al.* [77]. To understand the role of viscosity variations we follow [77] and decompose the EDV term as

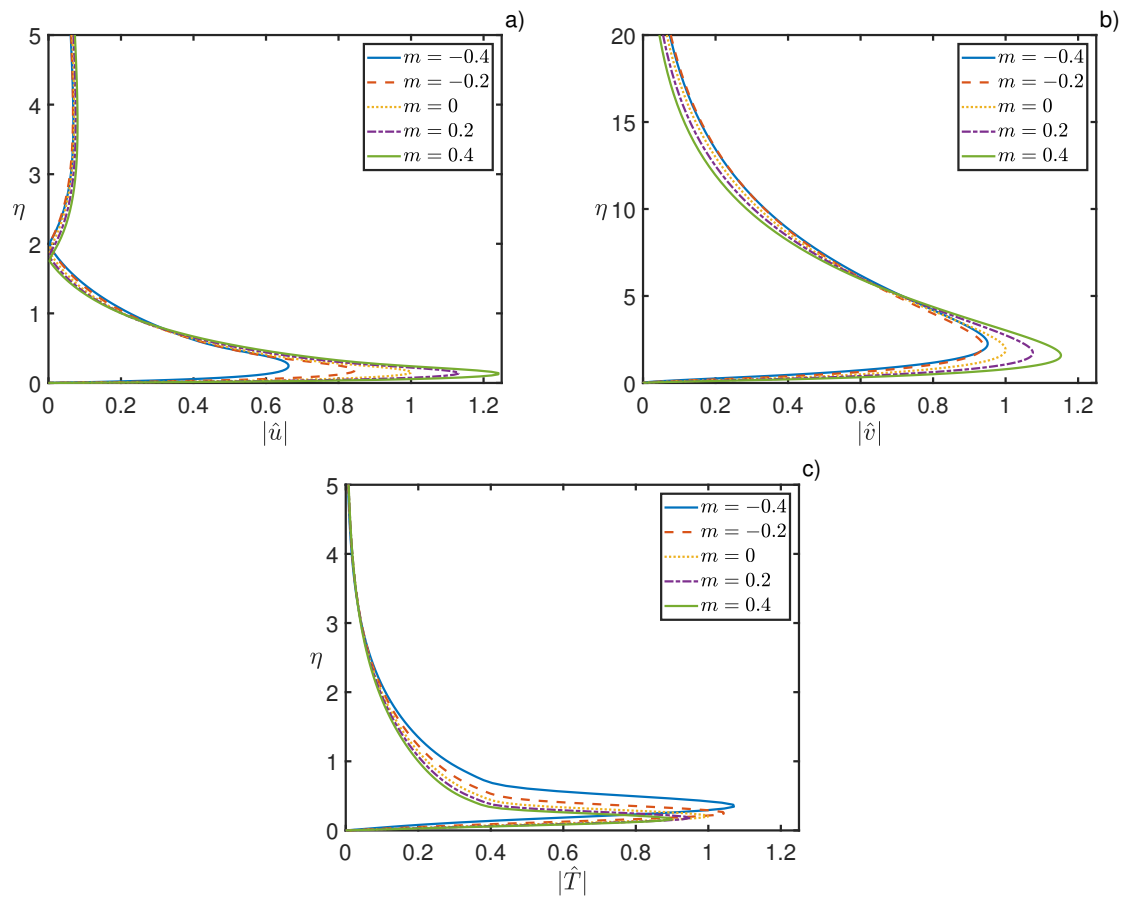


Figure 4.2: Plots of the eigenfunctions of (4.5), evaluated at $R = R_{\text{crit}} + 5000$ and $\min(\alpha_i)$. Each of the eigenfunctions have been scaled such that $\max |Q|_{m=0} = 1$, where $Q = \mathbf{Q} = (u, v, T, p)^T$

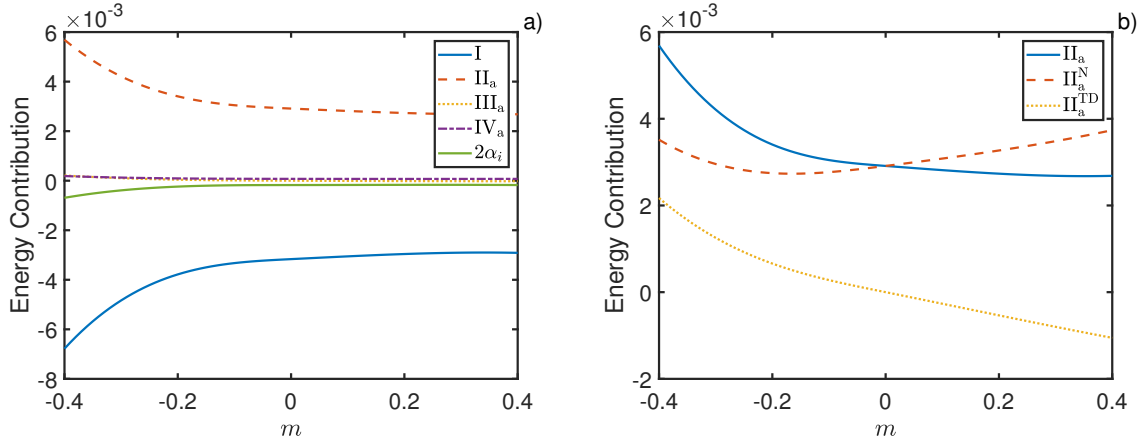


Figure 4.3: a) Plots of the energy contributions for each of the integrals on the right hand side of in equation (4.8). In b) we separate the energy dissipation due to viscosity term III_a into Newtonian and temperature dependent contributions.

follows

$$\Pi_a = \underbrace{\int_0^\infty \langle \hat{q}^2 \rangle dy}_{\Pi_a^N} + \underbrace{\int_0^\infty (\mu_B - 1) \langle \hat{q}^2 \rangle dy}_{\Pi_a^{TD}}.$$

The overall role of the change in viscosity may be observed in Figure 4.3 b). Here we see that although formally an energy dissipation term, for positive values of m this terms adds energy to the system. This energy production is balanced by increased dissipation from the Newtonian component leading to the asymptotic behaviour for as $m \rightarrow 0.4$. The energy analysis suggests that the overall energy balance is governed largely by the standard energy production and dissipation terms. This will be further investigated in Section 4.4 for the isothermal problem.

Before doing so, we will first explain the small range of stabilising values of $m \in [0, 0.34]$ observed in Figure 4.1 c). This is achieved by considering the EPRS and EDV terms from Figure 4.3 a). While in the plot it appears that these two curves are tending to a constant value as m increases, this is not the case. This is made clear in Figure 4.4 where we plot the derivative of these integrals with respect to m . Here we see that the EPRS term increases with m until $m \approx 0.36$. This roughly corresponds to the location found by tracking the critical Reynolds numbers on the neutral curves in Figure 4.1 c). This is then followed by an increase in energy dissipation. The fact that this increase occurs after the increase in energy production, and appears to have a smaller slope drives the increase in critical Reynolds number beyond this range.

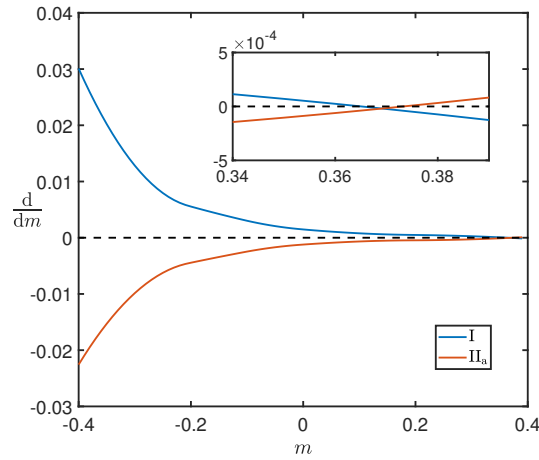


Figure 4.4: Plots derivative of I and II_a with respect to m . From the inset we see that the increase in EPRS occurs before the corresponding increase in EDV, causing the flow to be destabilised for $m > 0.34$.

4.4 Orr-Sommerfeld Comparison

The Orr-Sommerfeld equation has been extensively used to model instabilities of parallel flows. It was traditionally favoured over the primitive variables approach used above, as it reduces the continuity and momentum equations to a single fourth order ODE. This in turn reduces the size of the discretised operator by a factor of three for two-dimensional flows and a factor of four for three-dimensional flows. Given the widespread adoption of Chebychev spectral schemes to discretise the governing ordinary differential equations, where the m -th order derivative matrices are calculated by raising the first order derivate matrix to the m -th power, a trade-off exists. The repeated matrix multiplications required to calculate higher order derivatives can lead to floating point errors and a loss in accuracy. However, storage requirements for one dimensional problem with ~ 100 collocation points are not an issue for most modern laptops and so the primitive variables approach has been used due to its increased accuracy. While this leads to modest storage requirements compared to three-dimensional direct numerical simulations, it is more than sufficient given the exponential convergence of the spectral schemes utilised and the relative smoothness of the dominant eigenmodes of the Orr-Sommerfeld operator. This can be contrasted to the results of Weideman and Reddy [118], who validated Orszag's results [83] for the dominant eigenvalue in Plane Poiseuille flow to full machine precision for $N > 50$. That being said, we will compare our results in the uncoupled ($m = 0$) case, to the standard Orr-Sommerfeld formulation. In doing so we will show that in contrast to the rotating disk, the additional $\mathcal{O}(R^{-1})$ basic flow terms do not affect the overall flow stability. This is further validated by solving the biglobal eigenvalue problem, which arises from explicitly applying the assumptions of the Orr-Sommerfeld approach using the spectral element software Nektar++ [15].

The relative importance of the additional basic flow terms will be revisited in Chapter 6, where we look for alternative mechanisms for energy growth for the isothermal problem.

4.4.1 Orr-Sommerfeld Formulation

Here we outline the formulation of the standard Orr-Sommerfeld equation in two spatial dimensions. A more detailed derivation is given for the three dimensional problem with the addition of the Squire equation is given in Chapter 6. We choose to use the two-dimensional formulation for comparison with our previous results. This is in contrast to the non-modal analysis in Chapter 6 where three dimensional effects become significant.

The derivation of the Orr-Sommerfeld equations starts by taking a (dimensionless) basic flow of the form $\mathbf{U} = (U(y), 0)$, that is a streamwise oriented flow that depends only on the wall normal coordinate y . As before this basic flow state is perturbed such that $\mathbf{u} = (U(y), 0) + (u, v)$ and a system of linearised perturbation equations are found

$$\begin{aligned}\frac{\partial u}{\partial x} + \frac{\partial v}{\partial y} &= 0, \\ \frac{\partial u}{\partial t} + U \frac{\partial u}{\partial x} + vU' &= -\frac{\partial p}{\partial x} + \frac{1}{\text{R}} \nabla^2 u, \\ \frac{\partial v}{\partial t} + U \frac{\partial v}{\partial x} &= -\frac{\partial p}{\partial y} + \frac{1}{\text{R}} \nabla^2 v.\end{aligned}$$

Where $\nabla^2 = \frac{\partial^2}{\partial x^2} + \frac{\partial^2}{\partial y^2}$ is the Laplacian. Differentiating the x momentum with respect to y and the y momentum equation with respect to x and using the continuity equation, we can write the linearised perturbation equations as a single equation in terms of the wall normal perturbation velocity v

$$\left[\left(\frac{\partial}{\partial t} + U \frac{\partial}{\partial x} \right) \nabla^2 - U'' \frac{\partial}{\partial x} - \frac{1}{\text{Re}} \nabla^4 \right] v = 0, \quad (4.9)$$

which is solved subject to the boundary conditions

$$v = v' = 0 \text{ at } y = 0 \text{ and } y = \infty. \quad (4.10)$$

The Orr-Sommerfeld equation is derived by making the same normal mode assumption as before such that $v = \hat{v}(y)e^{i(\alpha x - \omega t)}$. This results in an equation of the form

$$\left[(-i\omega + i\alpha U) (\mathcal{D}^2 - \alpha^2) + i\alpha U'' - \frac{1}{\text{R}} (\mathcal{D}^2 - \alpha^2)^2 \right] \hat{v} = 0. \quad (4.11)$$

It is this equation which we compare to the linearised Navier Stokes equations for Crane's flow

by setting $U = e^{-y}$. To facilitate comparison with Nektar++, we solve the temporal problem by fixing $\alpha \in \Re$ and R to solve for the complex frequency ω via a generalised eigenvalue problem of the form

$$(A - \omega B)\hat{v} = 0,$$

where

$$A = i\alpha U (\mathcal{D}^2 - \alpha^2) + i\alpha U'' - \frac{1}{R} (\mathcal{D}^2 - \alpha^2)^2, \quad B = i(\mathcal{D}^2 - \alpha^2).$$

4.4.2 Nektar++

Nektar++ is an open source spectral element solver. Spectral element methods aim to combine the high order accuracy of spectral methods and the geometric flexibility of finite element schemes and were first used for fluid dynamic simulations by Patera [86]. Traditional finite element schemes for fluid flow problems typically use Taylor-Hood elements, which discretise the pressure with linear basis functions and the velocities with quadratic basis functions on each element. Refinement is achieved either by increasing the mesh density or by raising the order of the polynomial expansion. Spectral elements too typically use high order expansions on each element, however rather than using polynomials of order P defined on $P + 1$ equidistant nodes on each element, they use Lagrange polynomials defined through the zeros of the Gauss-Lobatto-Legendre quadrature points [15]. Thus the minimisation of interpolation errors achieved by classical spectral schemes is retained within each element.

Nektar++ contains a global flow stability solver, which solves the eigenvalue problem corresponding the linearised Navier-Stokes equations of the form

$$\frac{\partial \mathbf{u}}{\partial t} + (\mathbf{u} \cdot \nabla) \mathbf{U} + (\mathbf{U} \cdot \nabla) \mathbf{u} = -\nabla p + \nu \nabla^2 \mathbf{u}, \quad (4.12a)$$

$$\nabla \cdot \mathbf{u} = 0. \quad (4.12b)$$

in 2 – 3 spatial dimensions, where \mathbf{U} is the basic flow and \mathbf{u} is the perturbation. In setting up the problem to correspond to the Orr-Sommerfeld approach we fix our domain to be $[x, y] \in [0, 2\pi/\alpha] \times [0, y_{\max}]$, and impose that the perturbations are periodic in x , consistent with the normal mode assumption. The linearised Navier-Stokes equations are solved using a time stepper method as described in Tuckerman and Barkley [113], where the evolution of the linear perturbation equations (4.12a) is expressed as

$$\mathbf{q}(t) = \mathcal{A}(t)\mathbf{q}(0),$$

so that given some initial perturbation $\mathbf{q}(0)$ and for some arbitrary time τ , we find the dominant

eigenvalues and eigenvectors of the operator $\mathcal{A}(\tau)$. These are found as a solution of the equation

$$\mathcal{A}(\tau)\tilde{\mathbf{q}}_j = \mu_j\tilde{\mathbf{q}}_j,$$

where $\mu_j = e^{(\sigma+i\gamma)\tau}$ and may be related to the growth rate and frequency of the temporal Orr-Sommerfeld problem via

$$\begin{aligned}\mu_j &= e^{(\sigma+i\gamma)\tau} = |\mu_j|e^{i\theta}, \\ \omega_i &= \frac{\ln|\mu_j|}{\tau}, \quad \omega_r = \frac{\theta}{\tau}.\end{aligned}$$

Comparison of Results

To compare the different approaches we calculate the dominant eigenvalues along the line defined by $\text{Re} = 10^4$ that is bounded by the upper and lower branches of the neutral stability curve as shown in Figure 4.5. While there is a small difference between the Orr-Sommerfeld approach and the full linearised Navier Stokes, this difference is not as pronounced as in the rotating disk case. This is likely due to the fact that these additional base flow terms are $\mathcal{O}(R^{-1})$ and the Reynolds numbers are orders of magnitude larger than in the rotating disk case. Note that we have also included the results for a modified Orr-Sommerfeld Squire equation which is derived in Chapter 6 equation (6.3a). This retains the higher order basic flow terms in the formulation and is labelled OS ST (Orr-Sommerfeld stretching terms) in the Figure. Unsurprisingly, this agrees with the linearised Navier-Stokes equations, as it includes all of the same terms.

Using the assumptions of the Orr-Sommerfeld approach also yields the same solutions when compared to the solutions of the linearised Navier-Stokes equations in Nektar++. Note that the additional basic flow terms could not be retained using the Nektar's incompressible Navier stokes solver as it stands. However, given the agreement between the two approaches we can easily use the Nektar++ solutions to qualitatively visualise a single wavelength of the periodic two-dimensional eigenmode. This is shown in Figure 4.6, where we can see the emergence of the TS wave. Under the assumptions of linear theory, this structure is expected to grow as it is convected downstream until the perturbations become sufficiently large and interact with the basic flow, eventually leading to the flow becoming turbulent.

4.5 Discussions and Conclusions

In this Chapter we have numerically investigated the temperature dependent extension of Crane's flow. There are a number of features of interest in this analysis which have significant impli-

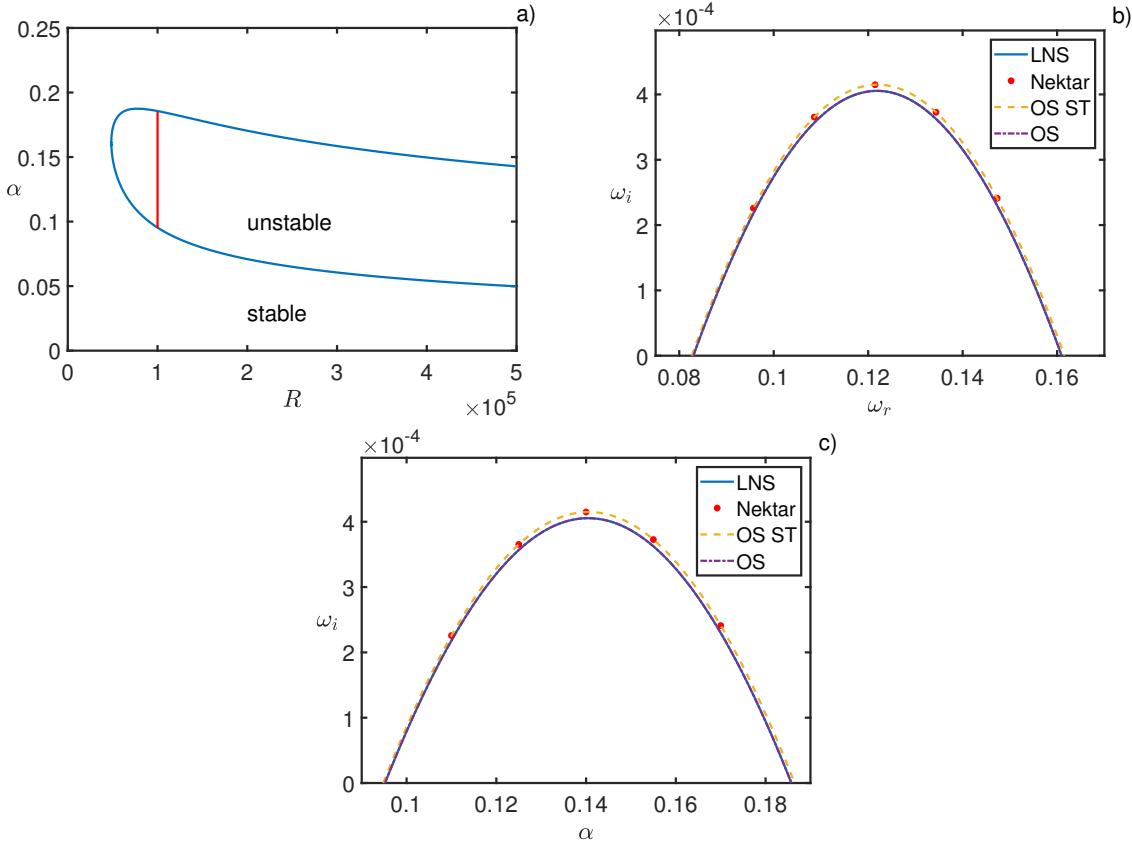


Figure 4.5: Comparison of the frequency and growth rates in b) calculated along the red curve marked on the neutral stability curve in a), for the isothermal stretching sheet. c) shows the corresponding plot of wavenumber versus temporal growth rate.

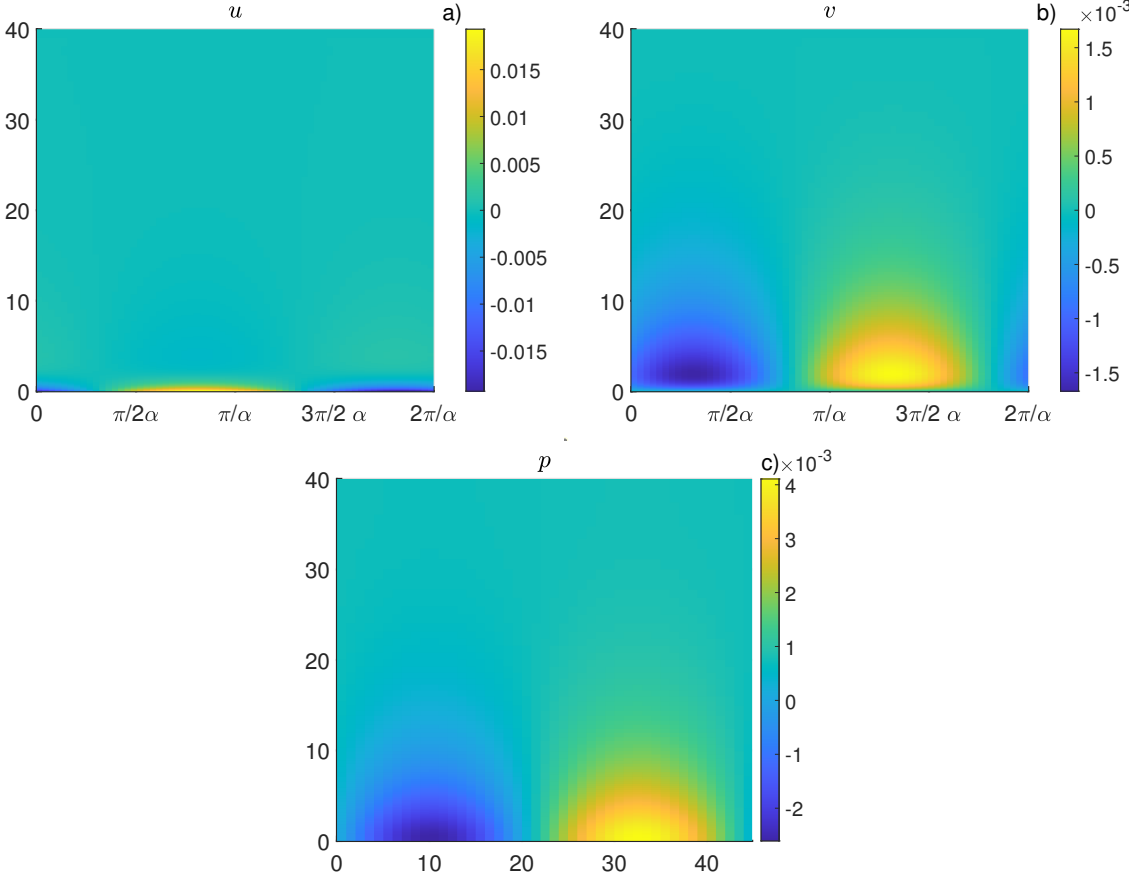


Figure 4.6: Two dimensional structure of the dominant TS eigenmodes for the streamwise, wall normal and pressure perturbations for $\alpha = 0.14$ and $Re = 10^4$, computed using Nektar++.

cations for the remainder of this thesis. Firstly, the critical Reynolds number is very large in comparison to other boundary layers such as Blasius flow, approximately 100 times larger in the isothermal case. However, this discrepancy is less pronounced when compared to boundary layers with exponential base flow solutions such as the asymptotic suction boundary layer studied by Dempsey and Walton [29], who reported a critical Reynolds number of 54370. This will prove useful in the asymptotic analysis in the following Chapter where our asymptotic expansion is predicated on the Reynolds number being large. This means that we will only have to take the leading order term in our expansion to validate our numerical results. Additionally, this observation raises the question of whether such a high Reynolds number would be required to observe transition in practice. This question has led us to investigate alternative mechanisms for energy growth in the non-modal analysis presented in Chapter 6.

Another notable feature is the additional terms that arise from the parallelisation of the basic flow. As discussed in the introduction, retaining these terms is crucial for improving the comparison with experiments in the rotating disk case. While the difference is less pronounced for the stretching sheet, these additional terms also appear to be stabilising, consistent with the findings for the rotating disk. This has been validated using both the Orr-Sommerfeld approach and a biglobal approach, with both methods showing excellent quantitative agreement. Whether this small difference is merely a consequence of the large Reynolds numbers involved will be revisited in Chapter 6, where we investigate energy growth mechanisms at Reynolds numbers that are orders of magnitude smaller.

Regarding transition prediction, there is a small range of values of $m \in [0, 0.34]$ (see Figure 4.1 c)), where the flow is stabilised. Values outside of this range lead to a reduction in the critical Reynolds number when compared to the isothermal case. This is in qualitative agreement with the results for the Blasius boundary layer [77], although the range of stabilising values of m is much narrower for the stretching sheet. The flow is strongly destabilised for negative values of m . This is particularly relevant from an industrial standpoint, as this regime represents the viscothermal behaviour of gases. The fact that the critical Reynolds number was halved for $m = -0.4$, coupled with the prominence of large temperature gradients in many extrusion flows, implies that viscothermal effects should be incorporated into any model of the full system as it destabilises the flow industrially relevant regimes.

The energy analysis suggests that instabilities could be suppressed through modification of the shear of the basic flow as this term drives EPRS. We will return to this idea after we conduct our asymptotic analysis in the next Chapter, as this will provide us with a richer understanding of the mechanisms driving the instability, allowing us to suggest control flow techniques for extrusion processes.

Nevertheless, regardless of the value of the sensitivity parameter our numerical linear stability analysis predicts a critical Reynolds number of order ten thousand, with our analysis performed at a local Reynolds number defined as a dimensionless distance from the inlet. However, Vlegaar [114] suggests that the flat, constant sheet temperature approach, with sheet speed proportional to the distance from the inlet may only be valid within half a meter from the inlet. Recalling the definition of our local Reynolds number $R = x^*/\delta^*$ where $\delta^* = \delta\sqrt{v^*/a^*}$. If we take the following values from Vlegaar $x^* = 0.5\text{m}$, $\nu^* = 3.59 \times 10^{-5}\text{m}^2\text{s}^{-1}$, $a^* = 20\text{s}^{-1}$, and $\delta \sim \mathcal{O}(1)$, we attain a value of $R \sim 400$. Using these figures it suggests that you would need to be approximately fifty meters from the inlet before the linear instability mechanism could be observed, which is far beyond the region at which our current model may be applied. Given these results, the question remains as to whether the linear modal mechanism is responsible for the destabilisation of such flows or whether an alternative mechanism may be responsible. We shall return to this question in Chapter 6, however first we shall validate our numerical results by comparing them to the asymptotic results for the same flow regime.

Chapter 5

Asymptotic Linear Stability Analysis

Prior to the widespread availability of modern computational tools in the late twentieth century, questions regarding the stability of a given flow regime had to be addressed using analytical approximations. As computational resources have become more readily available, the trend has increasingly shifted towards computational approaches, leading to many significant recent discoveries in the field of hydrodynamic stability. However, analytical approximations can explicitly reveal the essential physics driving a given instability and suggest methods for its suppression. They also serve as a means of validating computational results. For these reasons, we perform a lower branch asymptotic linear stability analysis of the temperature-dependent extension of Crane's flow in the absence of viscous dissipation. We focus on the lower branch because it is near this branch that the travelling wave disturbances we are investigating are most amplified. We concentrate on the non-dissipative regime as it allows for easier validation of our solutions through a parallel flow type approximation in the numerical analysis presented in the previous Chapter. As will be demonstrated, the inclusion of a temperature-dependent viscosity distribution quantitatively alters the stability characteristics of the flow, thereby justifying its consideration as a physically meaningful flow variable of interest. The analysis of Section 5.2 has been submitted as part of the publication Hanevy *et al.* [46].

5.1 Introduction

Asymptotic approximations to the stability of boundary layer flows are predicated on the largeness of the Reynolds number, with the earliest calculations taking the inviscid limit. Ignoring the effects of viscosity lead to a reduction of the fourth order Orr-Sommerfeld equation to the

second order Rayleigh equation, where no slip conditions can no longer be satisfied at the boundaries. This immediately implies that if viscous effects are to be accounted for at some large but finite value of the Reynolds number, then any consistent correction to the inviscid solutions must comprise a near wall layer where the governing equations are appropriately scaled to include the effects of viscosity. The next key observation arises through consideration the Rayleigh equation

$$(U - c) (\mathcal{D}^2 - \alpha^2) \hat{v} - U'' \hat{v} = 0,$$

where c is the ratio of the temporal and streamwise wavenumbers ω/α and represents the wave speed. The Rayleigh equation contains a regular singular point when $y = y_c$ such that $U(y_c) = c$. Solutions in the vicinity of this singular point were first obtained in Tollmien [107] via a Frobenius series expansion. It is the relative location and interactions between the viscous wall layer and the inviscid critical layer that determine the asymptotic structure on the upper and lower branches of the neutral stability curves respectively. The asymptotic structure of the lower branch analysis for Crane's flow closely resembles that of the Blasius boundary layer, as seen in Griffiths *et al.* [39]. Given that the Blasius boundary layer is the canonical boundary layer flow and is much more prominent in the literature, we will discuss developments in the analytical approaches to understanding its stability.

The approach taken in the remainder of this Chapter follows largely that of Smith [100], where the goal was to consider non-parallel effects on the lower branch of the Blasius boundary layer by including the slow streamwise variation of the basic flow profile in the asymptotic expansion. The perturbations were found to be governed by a triple deck structure due to the coalescence of the critical layer and the viscous wall layer. This led to a five term expansion where the linearised continuity and Navier-Stokes momentum equations in each of the decks were solved and matched at each order of approximation. The first four terms in Smith's expansion represented a parallel flow approximation with non-parallel terms coming in at the next order.

While it had originally been posited that an alternative five deck scaling was required to determine the upper branch instability [9], it was shown by Hultgren [53] that Smith's parallel flow solutions could be modified to describe both branches provided an additional normalisation term was retained in the dispersion relation. This normalisation term arises due to a loop in the Tietjens function which manifests as a kink on the upper branch for large Reynolds numbers. The five deck approach in Bodonyi and Smith [9] is valid above this kink on the upper branch. This is described in detail in the review of Healey [47], where the change in asymptotic structure from three to five decks can be observed by tracking the turning points in the phase of the numerically computed eigenfunctions along the upper branch as well as the location of the critical point. The critical point is shown to rise through the viscous wall layer with increasing Reynolds number before splitting from the wall layer causing the five deck structure to emerge.

This can be seen in Figure 6 (a) of [47].

As stated, the flow due to a flat stretching sheet has the same structure as the Blasius problem. However since the critical Reynolds number for Crane's flow is orders of magnitude larger than that of the Blasius problem, we will only consider the leading order in our expansion. As we will demonstrate, the leading order approximation will still provide excellent agreement and is sufficient to validate our numerical solutions of the previous Chapter.

5.2 Asymptotic Analysis

The lower branch asymptotic analysis follows largely from the isothermal analysis presented in Griffiths *et al.* [39]. In this Section we briefly highlight where the analysis differs. The first of these differences comes from the fact that the boundary layer thickness is not constant and varies with the sensitivity parameter m . This is accounted for in the numerical analysis by using δ^* as a non dimensionalising length scale so that the relationship between the asymptotic (Re) and numerical (R) Reynolds numbers is as follows

$$R = \delta x_s \text{Re}^{1/2}.$$

Note that the choice of nondimensionalising scales for the asymptotic analysis is the same as in Chapter 3 and [39], however the change in numerical scaling has to be accounted for when comparing the two different solutions. As in the isothermal analysis, we only calculate the leading order term in the dispersion relation. The key parameter driving the instability at this order is the wall shear stress. Here the wall shear stress now depends on the viscosity parameter m such that

$$\sigma_{xy}|_{y=0} = \mu_B u'_B|_{y=0}.$$

Before proceeding with our asymptotic analysis, we first demonstrate the origin of the scalings used on the lower branch by utilising order of magnitude estimates based on the dominant balance of terms in the respective layers, as well as evidence provided by numerical simulations of neutral curves along the lower branch.

5.2.1 Derivation of the Scaling on the Lower Branch

As noted the scaling for the temperature dependant problem follows largely from the isothermal problem. As such our analysis begins by examining the Orr-Sommerfeld system for Crane's flow

in the absence of a temperature dependent viscosity. The relevant equation is as follows

$$\left[\left(-i\omega + i\alpha U - \frac{1}{R}\Delta \right) \Delta - i\alpha U'' + \frac{1}{R} \left(V\Delta \frac{\partial}{\partial y} + V'\Delta + \frac{\partial}{\partial y} \left(U \frac{\partial}{\partial y} \right) \right) \right] \hat{v} = 0, \quad (5.1)$$

where $\Delta = \frac{d^2}{dy^2} - \alpha^2$. A detailed derivation of this equation is provided in Section 6.2. Here however, we are interested in the case of two-dimensional disturbances so that the spanwise wavenumber $\beta = 0$. This is in contrast to the non-modal analysis in the following Chapter. Note also that we have highlighted the additional stretching terms which do not appear in the standard Orr-Sommerfeld equations (4.11) in blue.

Large Reynolds number limit

Taking the limit as $R \rightarrow \infty$ in (5.1), we recover Rayleighs equation which is given as follows

$$\left(U - \frac{\omega}{\alpha} \right) \Delta \hat{v} - U'' \hat{v} = 0. \quad (5.2)$$

This equation governs the perturbations away from the sheet and away from the critical layer where $U = \omega/\alpha$. In both instances, viscosity is required to satisfy no-slip boundary conditions and to smooth out the singularity which arises in the critical layer. We know from related boundary layer flows such as the Blasius boundary layer [100], that the viscous wall layer and the critical layer coalesce on the lower branch. Thus, we consider the dominant balance for each of these respective cases and compare them in order to estimate the magnitude of the lower deck. Once this quantity is obtained the scalings for the main and upper decks immediately follow.

Wall Layer

Close to the wall we have $U = e^{-y} \approx 1 - y + \dots$. Here the dominant balance is between the viscous and inertial terms and is given as follows

$$\frac{d^4 \hat{v}}{dy^4} \sim i\alpha R \left(1 - \frac{\omega}{\alpha} - y \right) \frac{\partial^2 \hat{v}}{\partial y^2}.$$

If we let the thickness of the wall layer be $\mathcal{O}(\iota)$ and write $y = \iota \bar{y}$. Thus, we find

$$\iota \sim \left[\alpha R \left(1 - \frac{\omega}{\alpha} - \iota \bar{y} \right) \right]^{-1/2}$$

Note that from our numerical solutions we have $0 < \omega/\alpha < 1$.

Critical Layer

The critical layer is located at $y = y_c$ where $U(y_c) = \omega/\alpha$. This gives

$$e^{-y_c} = \frac{\omega}{\alpha} \implies y_c = \ln\left(\frac{\omega}{\alpha}\right).$$

The Taylor expansion of our basic flow about the critical point yields

$$U(y) \approx \frac{\omega}{\alpha} + (y - y_c)U'(y_c) + \dots = \frac{\omega}{\alpha} - (y - y_c)\frac{\omega}{\alpha} + \dots$$

Therefore the dominant terms of (5.1) in the vicinity of the critical point are

$$\frac{d^4 \hat{v}}{dy^4} \sim i\alpha R \left(- (y - y_c) \frac{\omega}{\alpha}\right) \frac{\partial^2 \hat{v}}{\partial y^2}.$$

If we write $y = y_c + \iota \bar{y}$, then it immediately follows that $\iota \sim (R\omega)^{-1/3}$.

Merging the Wall and Critical Layers

It remains to compare the scales that we have derived for both the wall and critical layers to make sure that they merge to provide the appropriate scaling for the lower deck. Taylor expansion of our basic flow about the sheet yields $U \approx 1 - y$. If $U = \omega/\alpha$ at the critical layer, this gives $y = 1 - \omega/\alpha$. Balancing this y with the wall layer thickness, ignoring the $\iota \bar{y}$ term for the moment we find

$$1 - \frac{\omega}{\alpha} \sim \left(\alpha R \left(1 - \frac{\omega}{\alpha}\right)\right)^{-1/2} \implies 1 - \frac{\omega}{\alpha} \sim (\alpha R)^{-1/3}.$$

Thus, if $\omega \sim \alpha$, the wall layer and critical layer have the same thickness and merge at the wall. The thickness of the wall layer is $\mathcal{O}(1 - \omega/\alpha)$, so the $\iota \bar{y}$ term is the same size as $1 - \omega/\alpha$ in the wall layer.

Numerical solutions suggest along the lower branch of the neutral curve suggest that $\omega \sim \alpha$ for $R \gg 1$. We can use our numerical solutions to give an indication of the scaling along the lower branch. To do this, we plot $\ln(1 - \omega/\alpha)$ and $\ln(R)$ as shown in Figure 5.1. We can deduce our scaling by observing firstly that there appears to be a linear relationship between the logarithm of both quantities. The slope of this line is approximately -0.25 . This suggests that $1 - \omega/\alpha \sim R^{-1/4}$ and that the thickness of the wall layer is $\mathcal{O}(R)^{-1/4}$. In addition, we further have $1 - \omega/\alpha \sim (\alpha R)^{-1/3}$, which gives $\alpha \sim \omega \sim R^{-1/4}$. For the analysis that follows, we simply have to consider these scalings in terms of our asymptotic Reynolds number Re .

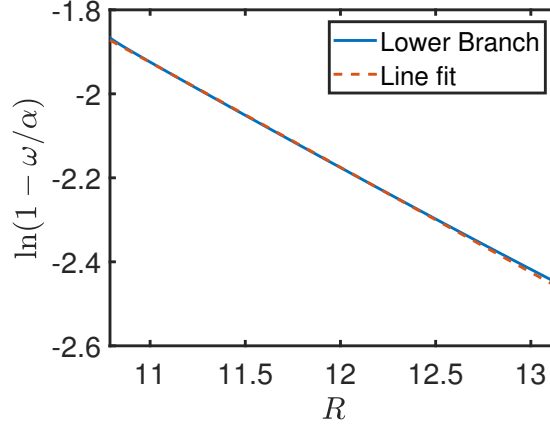


Figure 5.1: Plot of $\ln(1 - \omega/\alpha)$ against $\ln R$. The numerical solutions are the neutral solutions along the lower branch. These compared to a fitted line $y = mx + c$, with slope $m = -0.25$ and intercept $c \approx 1$.

If we continue to ignore viscothermal effects, the different non-dimensionalisations used in the two formulations lead to $R = \text{Re}^{1/2} x$. So that $1 - \omega/\alpha \sim \text{Re}^{-1/8}$ and $\alpha \sim \omega \sim \text{Re}^{-1/8}$. The ratio of the length scales is $\text{Re}^{1/2}$ and the ratio of the time scales is $R = \text{Re}^{1/2} x$. Letting α_n and ω_n denote the wavenumber and frequency for our numerical formulation and α_a and ω_a denote the corresponding terms for the asymptotic formulation then α_a is the ratio of the length scales times α_n giving $\alpha_a \sim \text{Re}^{1/2} \text{Re}^{-1/8} = \text{Re}^{3/8}$. Similarly, we can deduce that $\omega_a = \text{Re}^{3/8}$, and the thickness of the wall layer $\mathcal{O}(\text{Re}^{-1/2} \text{Re}^{-1/8}) = \mathcal{O}(\text{Re}^{-5/8})$. The main deck which covers the extent of the boundary layer scales as $\mathcal{O}(\text{Re}^{-4/8})$ and the upper deck, which is required to ensure the perturbations decay in the free stream, scales as $\mathcal{O}(\text{Re}^{-3/8})$. Although these scalings have been derived for the isothermal problem they may be utilised for the temperature dependent case provided the modification of the mean flow as a result of changes in viscosity remains sufficiently small.

5.2.2 Triple Deck Structure

In order to conduct our lower branch analysis we assume that the Reynolds number is large. For convenience, we define the small parameter $\epsilon = \text{Re}^{-1/8}$. As with the isothermal analysis, we find that the disturbances are governed by a triple deck structure with the lower, main and upper decks of thickness $\mathcal{O}(\epsilon^5)$, $\mathcal{O}(\epsilon^4)$ and $\mathcal{O}(\epsilon^3)$ respectively, as depicted in Figure 5.2. The stability analysis is performed at a local stream wise location x_s with a stream wise length scale and time scale of $\mathcal{O}(\epsilon^3)$. This leads to the introduction of the following scales

$$x - x_s = \epsilon^3 X, \quad t = \epsilon^3 \tau.$$

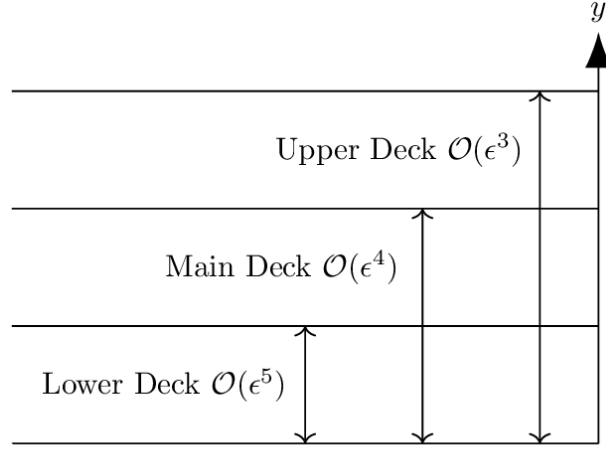


Figure 5.2: Schematic depicting the triple deck scaling used for the asymptotic analysis, with small parameter $\epsilon = \text{Re}^{-1/8}$. Note that this Figure is not to scale.

So that our flow variables are expanded as

$$u = xu_B(\eta) + \tilde{u}(x, y, t), \quad (5.3a)$$

$$v = \text{Re}^{-1/2} v_B(\eta) + \tilde{v}(x, y, t), \quad (5.3b)$$

$$p = \text{Re}^{-1} p_B(\eta) + \tilde{p}(x, y, t), \quad (5.3c)$$

$$T = T_B(\eta) + \tilde{T}(x, y, t), \quad (5.3d)$$

$$\mu = \mu_B(\eta) + \tilde{\mu}(x, y, t), \quad (5.3e)$$

where $\eta = \text{Re}^{-1/2} y$. Our linear perturbation equations become

$$\frac{\partial \tilde{u}}{\partial x} + \frac{\partial \tilde{v}}{\partial y} = 0, \quad (5.4a)$$

$$\begin{aligned} \frac{\partial \tilde{u}}{\partial t} + u_B \frac{\partial \tilde{u}}{\partial x} + \frac{\partial u_B}{\partial x} \tilde{u} + \text{Re}^{-1/2} v_B \frac{\partial \tilde{u}}{\partial y} + \tilde{v} \frac{\partial u_B}{\partial y} + \frac{\partial \tilde{p}}{\partial x} = \\ + \frac{\mu_B}{\text{Re}} \left(\frac{\partial^2 \tilde{u}}{\partial x^2} + \frac{\partial^2 \tilde{u}}{\partial y^2} \right) + \text{Re}^{-1} \left[\frac{\partial \mu_B}{\partial y} \left(\frac{\partial \tilde{u}}{\partial y} + \frac{\partial \tilde{v}}{\partial x} \right) + \frac{\partial \tilde{\mu}}{\partial y} \frac{\partial u_B}{\partial y} + 2 \frac{\partial \tilde{\mu}}{\partial x} \frac{\partial u_B}{\partial x} \right], \end{aligned} \quad (5.4b)$$

$$\begin{aligned} \frac{\partial \tilde{v}}{\partial t} + u_B \frac{\partial \tilde{v}}{\partial x} + \text{Re}^{-1/2} \left(v_B \frac{\partial \tilde{v}}{\partial y} + \frac{\partial v_B}{\partial y} \tilde{v} \right) + \frac{\partial \tilde{p}}{\partial y} = \\ + \text{Re}^{-1} \left[2 \frac{\partial \mu_B}{\partial y} \frac{\partial \tilde{v}}{\partial y} + 2 \text{Re}^{-1/2} \frac{\partial \tilde{\mu}}{\partial y} \frac{\partial v_B}{\partial y} + \mu_B \left(\frac{\partial^2 \tilde{v}}{\partial x^2} + \frac{\partial^2 \tilde{v}}{\partial y^2} \right) + \text{Re}^{-1/2} \tilde{\mu} \frac{\partial^2 v_B}{\partial y^2} + \frac{\partial \tilde{\mu}}{\partial x} \frac{\partial u_B}{\partial y} \right], \end{aligned} \quad (5.4c)$$

$$\frac{\partial \tilde{T}}{\partial t} + u_B \frac{\partial \tilde{T}}{\partial x} + \text{Re}^{-1/2} v_B \frac{\partial \tilde{T}}{\partial y} + \tilde{v} \frac{\partial T_B}{\partial y} = \frac{1}{\text{Re Pr}} \left(\frac{\partial^2 \tilde{T}}{\partial x^2} + \frac{\partial^2 \tilde{T}}{\partial y^2} \right). \quad (5.4d)$$

We assume that the perturbations have normal form and are proportional to $E = \exp(i\theta(X) - i\omega\tau)$, where the frequency is constant and is expanded as $\bar{\omega} = \omega_0 + \epsilon\omega_1 + \dots$. The wavenumber θ is taken to be a slowly varying function of \bar{x} and is expanded as

$$\frac{d\theta}{dX} = \alpha = \alpha_0(x) + \epsilon\alpha_1(x) + \dots.$$

Main Deck

We begin our analysis in the main deck which covers the extent of the boundary layer, and where the disturbances are inviscid and rotational. The wall normal coordinate is $\bar{y} = \epsilon^4 y = \eta$ and the disturbances are expanded as

$$\begin{aligned}\tilde{u} &= (U_{m0} + \epsilon U_{m1} + \dots) E, \\ \tilde{v} &= (\epsilon V_{m0} + \epsilon^2 V_{m1} + \dots) E, \\ \tilde{p} &= (\epsilon P_{m0} + \epsilon^2 P_{m1} + \dots) E, \\ \tilde{T} &= (T_{m0} + \epsilon T_{m1} + \dots) E,\end{aligned}$$

where U_{m0} , for example is a function of both \bar{x} and y . Substituting these expansions into our linear perturbation equations (5.4) we have

$$i\epsilon^{-3} (\alpha_0 + \epsilon\alpha_1 + \dots) [U_{m0} + \epsilon U_{m1} + \dots] + \epsilon^{-3} \left(\frac{\partial V_{m0}}{\partial \eta} + \epsilon \frac{\partial V_{m1}}{\partial \eta} + \dots \right) = 0, \quad (5.5a)$$

$$\begin{aligned}& -i\epsilon^{-3} (\omega_0 + \epsilon\omega_1 + \dots) [U_{m0} + \epsilon U_{m1} + \dots] + i\epsilon^{-3} u_B (\alpha_0 + \epsilon\alpha_1 + \dots) [U_{m0} + \epsilon U_{m1} + \dots] \\ & + \epsilon^{-3} (V_{m0} + \epsilon V_{m1} + \dots) \frac{\partial u_B}{\partial \eta} + i\epsilon^{-2} (\alpha_0 + \epsilon\alpha_1 + \dots) [P_{m0} + \epsilon P_{m1} + \dots] \\ & = \mu_B \left(\frac{\partial^2 U_{m0}}{\partial \eta^2} + \epsilon \frac{\partial^2 U_{m1}}{\partial \eta^2} \right) + \frac{\partial \mu_B}{\partial \eta} \left(\frac{\partial U_{m0}}{\partial \eta} + \epsilon \frac{\partial U_{m1}}{\partial \eta} \right) + \frac{\partial u_B}{\partial \eta} \left(\frac{\partial M_{m0}}{\partial \eta} + \frac{\partial M_{m1}}{\partial \eta} \right) + \mathcal{O}(\epsilon^2),\end{aligned} \quad (5.5b)$$

$$\begin{aligned}
& \epsilon^{-2} (\omega_0 + \epsilon\omega_1 + \dots) \left[V_{m0} + \epsilon V_{m1} + \dots \right] + i\epsilon^{-2} u_B (\alpha_0 + \epsilon\alpha_1 + \dots) \left[V_{m0} + \epsilon V_{m1} + \dots \right] \\
& + \epsilon \left(v_B \left[\frac{\partial V_{m0}}{\partial \eta} + \epsilon \frac{\partial V_{m1}}{\partial \eta} + \dots \right] + \frac{\partial v_B}{\partial \eta} \left[V_{m0} + \epsilon V_{m1} + \dots \right] \right) \\
& + \epsilon^{-3} \left[\frac{\partial P_{m0}}{\partial \eta} + \epsilon \frac{\partial P_{m1}}{\partial \eta} + \dots \right] = \epsilon^{-1} \left\{ 2 \frac{\partial \mu_B}{\partial \eta} \left[\frac{\partial V_{m0}}{\partial \eta} + \epsilon \frac{\partial V_{m1}}{\partial \eta} + \dots \right] \right. \\
& \left. + \mu_B \left[\frac{\partial^2 V_{m0}}{\partial \eta^2} + \epsilon \frac{\partial^2 V_{m1}}{\partial \eta^2} + \dots \right] + i \frac{\partial u_B}{\partial \eta} (\alpha_0 + \epsilon\alpha_1 + \dots) \left[M_{m0} + \epsilon M_{m1} + \dots \right] \right\} + \mathcal{O}(\epsilon^2),
\end{aligned} \tag{5.5c}$$

$$\begin{aligned}
& -i\epsilon^{-3} (\omega_0 + \epsilon\omega_1 + \dots) \left[T_{m0} + \epsilon T_{m1} + \dots \right] + i\epsilon^{-3} u_B (\alpha_0 + \epsilon\alpha_1 + \dots) \left[T_{m0} + \epsilon T_{m1} + \dots \right] \\
& + v_B \left[\frac{\partial T_{m0}}{\partial \eta} + \epsilon \frac{\partial T_{m1}}{\partial \eta} + \dots \right] + \epsilon^{-3} \frac{\partial T_B}{\partial \eta} \left[V_{m0} + \epsilon V_{m1} + \dots \right] = \\
& \text{Pr}^{-1} \left[\frac{\partial^2 T_{m0}}{\partial \eta^2} + \epsilon \frac{\partial^2 T_{m1}}{\partial \eta^2} + \dots \right] + \mathcal{O}(\epsilon^2),
\end{aligned} \tag{5.5d}$$

where we have used

$$M_{mi} = -\frac{m}{(1 + mT_B)^2} (T_{m0} + T_{m1} + \dots),$$

as a shorthand for the asymptotic expansion of the disturbance viscosity. Note that we included only the largest of the viscous terms in the expansion. The remaining terms are sufficiently small that they do not contribute to the leading order dispersion relation. Gathering the leading order terms we have

$$i\alpha_0 U_{m0} + \frac{\partial V_{m0}}{\partial \eta} = 0, \tag{5.6a}$$

$$-i\omega_0 U_{m0} + u_B i\alpha_0 U_{m0} + V_{m0} \frac{\partial u_B}{\partial \eta} = 0, \tag{5.6b}$$

$$\frac{\partial P_{m0}}{\partial \eta} = 0, \tag{5.6c}$$

$$-i\omega_0 T_{m0} + u_B i\alpha_0 T_{m0} + V_{m0} \frac{\partial T_B}{\partial \eta} = 0. \tag{5.6d}$$

From equation (5.6c) we see that P_{m0} is a function of x . The remaining solutions are

$$U_{m0} = -B_0(x) \frac{\partial u_B}{\partial \eta}, \tag{5.7a}$$

$$V_{m0} = iB_0(x) (\alpha_0 u_B - \omega_0), \tag{5.7b}$$

$$T_{m0} = -B_0(x) \frac{\partial T_B}{\partial \eta}, \tag{5.7c}$$

where B_0 and P_{m0} are slowly varying amplitude functions, to be determined by matching with the solutions in the other decks. As $\eta \rightarrow \infty$ we have

$$U_{m0} \rightarrow 0, \quad V_{m0} \rightarrow -i\omega_0 B_0, \quad T_{m0} \rightarrow 0.$$

As $\eta \rightarrow 0$ we have

$$\begin{aligned} U_{m0} &\rightarrow -B_0 \left. \frac{\partial u_B}{\partial \eta} \right|_{\eta=0} + \mathcal{O}(\eta), \\ V_{m0} &\rightarrow iB_0(x) \left(\alpha_0 x_s - \omega_0 + \alpha_0 \eta \left. \frac{\partial u_B}{\partial \eta} \right|_{\eta=0} + \dots \right), \\ T_{m0} &\rightarrow -B_0 \left. \frac{\partial T_B}{\partial \eta} \right|_{\eta=0} + \mathcal{O}(\eta). \end{aligned}$$

For these viscous modes we choose

$$\alpha_0 x_s = \omega_0 \text{ as } \eta \rightarrow 0,$$

corresponding to the critical layer where $u_B = \omega/\alpha$.

Upper Deck

The upper deck is required to satisfy the homogeneous Dirichlet conditions in the free stream. In the upper deck the base flow quantities behave as follows

$$\begin{aligned} u_B \rightarrow T \rightarrow 0, \quad v_B \rightarrow V_\infty, \\ p_B \rightarrow P_\infty, \quad \mu_B \rightarrow 1. \end{aligned}$$

Here the disturbances are inviscid and irrotational. The wall normal coordinate is scaled $\bar{y} = \epsilon^3 \tilde{y}$ and the perturbation variables are expanded as

$$\begin{aligned} \tilde{u} &= (\epsilon \bar{U}_0 + \epsilon^2 \bar{U}_1 + \dots) E, \\ \tilde{v} &= (\epsilon \bar{V}_0 + \epsilon^2 \bar{V}_1 + \dots) E, \\ \tilde{p} &= (\epsilon \bar{P}_0 + \epsilon^2 \bar{P}_1 + \dots) E, \\ \tilde{T} &= (\epsilon \bar{T}_0 + \epsilon^2 \bar{T}_1 + \dots) E, \end{aligned}$$

to ensure matching between the upper and main decks. Again, we substitute these expansions into our linear perturbation equations (5.4) to get we have

$$i\epsilon^{-2}(\alpha_0 + \epsilon\alpha_1 + \dots) [\bar{U}_0 + \epsilon\bar{U}_1 + \dots] + \epsilon^{-2} \left(\frac{\partial \bar{V}_0}{\partial \bar{y}} + \epsilon \frac{\partial \bar{V}_1}{\partial \bar{y}} + \dots \right) = 0, \quad (5.8a)$$

$$\begin{aligned} & -i\epsilon^{-2}(\omega_0 + \epsilon\omega_1 + \dots) [\bar{U}_0 + \epsilon\bar{U}_1 + \dots] + \epsilon^2 V_\infty \left[\frac{\partial \bar{U}_0}{\partial \bar{y}} + \epsilon \frac{\partial \bar{U}_1}{\partial \bar{y}} + \dots \right] \\ & + i\epsilon^{-2}(\alpha_0 + \epsilon\alpha_1 + \dots) [\bar{P}_0 + \epsilon\bar{P}_1 + \dots] = \mathcal{O}(\epsilon^2) \end{aligned} \quad (5.8b)$$

$$\begin{aligned} & -i\epsilon^{-2}(\omega_0 + \epsilon\omega_1 + \dots) [\bar{V}_0 + \epsilon\bar{V}_1 + \dots] + \epsilon^2 V_\infty \left[\frac{\partial \bar{V}_0}{\partial \bar{y}} + \epsilon \frac{\partial \bar{V}_1}{\partial \bar{y}} + \dots \right] \\ & + \epsilon^{-2} \left[\frac{\partial \bar{P}_0}{\partial \bar{y}} + \epsilon \frac{\partial \bar{P}_1}{\partial \bar{y}} + \dots \right] = \mathcal{O}(\epsilon^2) \end{aligned} \quad (5.8c)$$

$$-i\epsilon^{-2}(\omega_0 + \epsilon\omega_1 + \dots) [\bar{T}_0 + \epsilon\bar{T}_1 + \dots] + \epsilon^2 V_\infty \left[\frac{\partial \bar{T}_0}{\partial \bar{y}} + \epsilon \frac{\partial \bar{T}_1}{\partial \bar{y}} + \dots \right] = \mathcal{O}(\epsilon^2). \quad (5.8d)$$

Where again we have not explicitly expanded the viscous terms as they are of a larger order and do not contribute to the flow dynamics in this upper inviscid region as would be expected. The governing equations in this deck are to leading order

$$i\alpha_0 \bar{U}_0 + \frac{\partial \bar{V}_0}{\partial \bar{y}} + i\beta_0 \bar{W}_0 = 0, \quad (5.9a)$$

$$-i\omega_0 \bar{U}_0 = -i\alpha_0 \bar{P}_0, \quad (5.9b)$$

$$-i\omega_0 \bar{V}_0 = -\frac{\partial \bar{P}_0}{\partial \bar{y}}, \quad (5.9c)$$

$$-i\omega_0 \bar{T}_0 = 0. \quad (5.9d)$$

Equation (5.9d) tells us that $\bar{T}_0 = 0$. We can differentiate the x momentum equation with respect to x , the y momentum equation with respect to \bar{y} and use the continuity equation to attain a single equation for \bar{P}_0

$$\frac{\partial \bar{P}_0}{\partial \bar{y}} - \alpha_0^2 \bar{P}_0 = 0.$$

The solution which satisfies the boundedness condition as $\bar{y} \rightarrow \infty$ and matches with solution in the main deck as $\bar{y} \rightarrow 0$ is

$$\bar{P}_0 = P_{m0}(x) e^{-\alpha_0 \bar{y}}.$$

The remaining solutions for the disturbance velocities are thus

$$\bar{U}_0 = \frac{1}{x_s} P_{m0} e^{-\alpha_0 \bar{y}}, \quad (5.10)$$

$$\bar{V}_0 = \frac{i}{x_s} P_{m0}(\bar{x}) e^{-\alpha_0 \bar{y}}, \quad (5.11)$$

$$(5.12)$$

Matching \bar{V}_0 as $\tilde{y} \rightarrow 0$, with V_{m0} as $\eta \rightarrow \infty$ yields the following relation between the two amplitude functions

$$B_0 = -\frac{1}{\alpha_0 x_s^2} P_{m0}.$$

Lower Deck

In order to obtain our dispersion relation we must match our solutions in the main deck with those in the lower deck. This deck is required to satisfy the no slip conditions on the surface of the stretching sheet. Here $\bar{y} = \epsilon^5 \bar{Y}$ and the basic flow quantities are Taylor expanded about $\bar{Y} = 0$.

$$\begin{aligned} u_B &\approx x + u'_B(x, 0) \epsilon \bar{Y} + \dots, \\ v_B &\approx v'_B(x, 0) \epsilon \bar{Y} + \dots, \\ T_B &\approx 1 + T'_B(x, 0) \epsilon \bar{Y} + \dots, \\ \mu_B &\approx \frac{1}{1+m} + \mu'_B(x, 0) \epsilon \bar{Y} + \dots. \end{aligned}$$

The disturbances are expanded as follows

$$\begin{aligned} \tilde{u} &= (U_0 + \epsilon U_1 + \dots) E, \\ \tilde{v} &= (\epsilon^2 V_0 + \epsilon^3 V_1 + \dots) E, \\ \tilde{p} &= (\epsilon P_0 + \epsilon^2 P_1 + \dots) E, \\ \tilde{T} &= (T_0 + \epsilon \bar{T}_1 + \dots) E. \end{aligned}$$

Applying the same procedure as for the other decks we find the governing equations in the lower deck are as follows

$$\epsilon^{-3} (\alpha_0 + \epsilon \alpha_1 + \dots) \left[U_0 + \epsilon U_1 + \dots \right] + \epsilon^{-3} \left[\frac{\partial V_0}{\partial \bar{Y}} + \epsilon \frac{\partial V_1}{\partial \bar{Y}} + \dots \right] = 0, \quad (5.13a)$$

$$\begin{aligned}
& -i\epsilon^{-3}(\omega_0 + \epsilon\omega_1 + \dots) \left[U_0 + \epsilon U_1 + \dots \right] + i\epsilon^{-3}x_s(1 + \epsilon\bar{Y}u'_{B0} + \dots)(\alpha_0 + \epsilon\alpha_1 + \dots) \left[U_0 + \epsilon U_1 + \dots \right] \\
& + (1 + \epsilon\bar{Y}u'_{B0} + \dots) \left[U_0 + \epsilon U_1 + \dots \right] + (v'_{B0}\bar{Y} + \dots) \left[\frac{\partial U_0}{\partial \bar{Y}} + \epsilon \frac{\partial U_1}{\partial \bar{Y}} + \dots \right] \\
& + \epsilon^{-2}(u'_{B0} + \dots) \left[V_0 + \epsilon V_1 + \dots \right] + i\epsilon^{-2}(\alpha_0 + \epsilon\alpha_1 + \dots) \left[P_0 + \epsilon P_1 + \dots \right] \\
& = \epsilon^{-2}\mu_{B0} \left[\frac{\partial^2 U_0}{\partial \bar{Y}^2} + \epsilon \frac{\partial^2 U_1}{\partial \bar{Y}^2} + \dots \right] + \mathcal{O}(\epsilon^{-1}), \tag{5.13b}
\end{aligned}$$

$$\begin{aligned}
& -i\epsilon^{-1}(\omega_0 + \epsilon\omega_1 + \dots) \left[V_0 + \epsilon V_1 + \dots \right] + i\epsilon^{-1}x_s(1 + \epsilon\bar{Y}u'_{B0})(\alpha_0 + \epsilon\alpha_1 + \dots) \left[V_0 + \epsilon V_1 + \dots \right] \\
& + \epsilon^2 \frac{\partial}{\partial \bar{Y}} \left[(v'_{B0} + \dots)(V_0 + \epsilon V_1 + \dots) \right] + \epsilon^{-4} \left[\frac{\partial P_0}{\partial \bar{Y}} + \frac{\partial P_1}{\partial \bar{Y}} \dots \right] = \mathcal{O}(\epsilon^{-1}) \tag{5.13c}
\end{aligned}$$

$$\begin{aligned}
& -i\epsilon^{-3}(\omega_0 + \epsilon\omega_1 + \dots) \left[T_0 + \epsilon T_1 + \dots \right] + i\epsilon^{-3}x_s(1 + \epsilon\bar{Y}u'_{B0} + \dots)(\alpha_0 + \epsilon\alpha_1 + \dots) \left[T_0 + \epsilon T_1 + \dots \right] \\
& + (\bar{Y}v'_{B0} + \dots) \left[\frac{\partial T_0}{\partial \bar{Y}} + \epsilon \frac{\partial T_1}{\partial \bar{Y}} + \dots \right] + \epsilon^{-2}(T'_{B0} + \dots) \left[V_0 + \epsilon V_1 + \dots \right] \\
& = \text{Pr}^{-1} \epsilon^{-2} \left[\frac{\partial^2 T_0}{\partial \bar{Y}^2} + \epsilon \frac{\partial^2 T_1}{\partial \bar{Y}^2} + \dots \right] + \mathcal{O}(\epsilon^2) \tag{5.13d}
\end{aligned}$$

where $u'_{B0} = u'_B(x, 0)$, $T'_{B0} = T'_B(x, 0)$ and $\mu_{B0} = \frac{1}{1+m}$. The leading order terms in the governing equations are thus

$$i\alpha_0 U_0 + \frac{\partial V_0}{\partial \bar{Y}} = 0, \tag{5.14a}$$

$$-i(\omega_1 - x_s \alpha_1)U_0 + i\alpha_0 u'_{B0} \bar{Y} U_0 + u'_{B0} V_0 = -i\alpha_0 P_0 + \mu_{B0} \frac{\partial^2 U_0}{\partial \bar{Y}^2}, \tag{5.14b}$$

$$\frac{\partial P_0}{\partial \bar{Y}} = 0, \tag{5.14c}$$

$$-i(\omega_1 - x_s \alpha_1)T_0 + i\alpha_0 u'_{B0} \bar{Y} T_0 + T'_{B0} V_0 = \text{Pr}^{-1} \frac{\partial^2 T_0}{\partial \bar{Y}^2}. \tag{5.14d}$$

Note that the largest non-zero terms in the x momentum and energy equations are $\mathcal{O}(\epsilon^{-2})$, since $\alpha_0 x_s = \omega_0$ from the definition of the critical layer. For convenience, we define $\lambda = u'_{B0}$ and $\chi = T'_{B0}$. Note that both λ and χ are negative for our flow. From (5.14c) we have $P_0 = P_0(x)$ and in order to match with the main deck we must have

$$P_0 = P_{m0}.$$

Using this we can differentiate the x momentum equation with respect to \bar{Y} and use the continuity equation to attain the following Airy equation after multiplying by α_0

$$\alpha_0 \frac{\partial^3 U_0}{\partial \bar{Y}^3} - \frac{i}{\mu_{B0}} ((\alpha_1 x_s - \omega_1) + \alpha_0 u'_{B0} \bar{Y}) \left(\alpha_0 \frac{\partial U_0}{\partial \bar{Y}} \right) = 0.$$

This may be more easily seen after making the coordinate system transformation

$$\xi = \left(\frac{i\alpha_0 u'_{B0}}{\mu_{B0}} \right)^{1/3} \left(\bar{Y} + \frac{\alpha_1 x_s - \omega_1}{\alpha_0 u'_{B0}} \right),$$

so that the equation becomes

$$\frac{\partial^3}{\partial \xi^3} (\alpha_0 U_0) - \xi \frac{\partial}{\partial \xi} (\alpha_0 U_0) = 0. \quad (5.15)$$

The solution for U_0 must satisfy

$$\begin{aligned} U_0 &= 0 & \text{at} & \quad \bar{Y} = 0, \\ U_0 &\rightarrow \frac{u'_{B0}}{x_s^2} & \text{as} & \quad \bar{Y} \rightarrow \infty. \end{aligned}$$

Therefore, U_0 satisfies a homogeneous Airy equation and our solution is in terms of a Scorer function. The solution to (5.15), which is bounded as $\xi \rightarrow \infty$ is

$$\alpha_0 \frac{\partial U_0}{\partial \xi} = C_0 \text{Ai}(\xi).$$

Then

$$\alpha_0 U_0 = C_0 \int_{\xi_0}^{\xi} \text{Ai}(\bar{\xi}) d\bar{\xi},$$

to satisfy the boundary condition $U_0 = 0$ at $\xi = \xi_0$ where

$$\xi_0 = (i\alpha_0 x_s)^{-2/3} \mu_{B0}^{-1/3} i(\alpha_1 x_s - \omega_1).$$

Eigenrelation

Applying the boundary conditions $U_0 = 0$ in the x momentum equation in the lower deck we have

$$\frac{\partial^2 U_0}{\partial \bar{Y}^2} - i \frac{\alpha_0}{\mu_{B0}} P_0 = 0, \quad \text{at} \quad \bar{Y} = 0.$$

Therefore, we have

$$\left(\frac{i\alpha_0 u'_{B0}}{\mu_{B0}} \right)^{2/3} \mu_{B0} \alpha_0 \frac{\partial^2 U_0}{\partial \xi^2} = i\alpha_0^2 P_{m0} \quad \text{at} \quad \xi = \xi_0,$$

which allows us to relate C_0 and P_{m0} to get

$$\left(\frac{-i\alpha_0|u'_{B0}|}{\mu_{B0}}\right)^{2/3} \mu_{B0} C_0 \text{Ai}'(\xi_0) = i\alpha_0^2 P_{m0}. \quad (5.16)$$

Matching $\alpha_0 U_0$ between the main and lower decks yields a second relationship between C_0 and P_{m0}

$$C_0 \int_{\xi_0}^{\infty} \text{Ai}(\xi) d\xi = -\frac{|u'_{B0}|}{x_s^2} P_{m0}. \quad (5.17)$$

Dividing (5.16) and (5.17) gives the eigenrelation

$$\text{Ai}'(\xi_0) = \kappa (-i\alpha x_s)^{1/3} \frac{\alpha_0 x_s^{5/3}}{\mu_{B0}^{1/3} |\bar{u}'_{B0}|^{5/3}}, \quad (5.18)$$

where $\kappa = \int_{\xi_0}^{\infty} \text{Ai}(\xi) d\xi$ and $\xi_0 = (-i\alpha_0 x_s)^{-2/3} i(\alpha_1 x_s - \omega_1)$. We can scale \bar{x}_s from this eigenrelation by letting

$$\alpha_0 = x_s^{-1/4} \bar{\alpha}_0, \quad \alpha_1 x_s - \omega_1 = x_s^{1/2} \bar{\gamma}_1, \quad |u'_{B0}| = x_s \bar{u}'_{B0},$$

Our scaled eigenrelation becomes

$$\text{Ai}'(\xi_0) = \frac{\kappa e^{-i\pi/6} \bar{\alpha}_0^{4/3}}{\mu_{B0}^{1/3} |\bar{u}'_{B0}|^{5/3}}, \quad (5.19)$$

where

$$\xi_0 = \frac{e^{i5\pi/6} \bar{\gamma}_1}{(\bar{\alpha}_0 \bar{u}'_{B0})^{2/3} \mu_{B0}^{1/3}}.$$

The remainder of the analysis follows that in Griffiths *et al.* [39] and involves numerically solving (5.19) in terms of the Tjietens function to determine the neutral values of $\bar{\gamma}_1$ and $\bar{\alpha}_0$. This can be achieved by swapping the limits of integration of κ , dividing (5.19) by $\xi_0 \int_{\infty}^{\xi_0} \text{Ai}(\xi) d\xi$

$$\frac{\text{Ai}'(\xi_0)}{\xi_0 \int_{\infty}^{\xi_0} \text{Ai}(\xi) d\xi} = \frac{\bar{\alpha}_0^2}{|\bar{u}'_{B0}| \bar{\gamma}_1},$$

If we take the complex conjugate of the equation, since we are only interested in neutral values where the imaginary part is zero, and subtract from one we attain

$$1 - \frac{\text{Ai}'(\xi)}{\xi_0 \int_{\infty}^{\xi_0} \text{Ai}(\xi) d\xi} = \frac{|\bar{u}'_{B0}| \bar{\gamma}_1 - \bar{\alpha}_0^2}{|\bar{u}'_{B0}|},$$

using the notation in Healey [47]. The left-hand side is the Tjietens function $F^+(e^{-i5\pi/6}z)$ and

$$\xi_0 = \frac{e^{-i5\pi/6}(\bar{\alpha}_0|\bar{u}'_{B0}|)^{-2/3}\bar{\gamma}_1}{\mu_{B0}^{1/3}}. \quad (5.20)$$

It is known that the Tjietens function is real when evaluated at $F^+(e^{-i5\pi/6}2.297) = 0.564$ [47]. From this we can evaluate the remaining parameters in our problem for neutral values of $\bar{\alpha}_0$

$$\begin{aligned} 2.297 &\approx \frac{(\bar{\alpha}_0|\bar{u}'_{B0}|)^{-2/3}\bar{\gamma}_1}{\mu_{B0}^{1/3}}, \\ 0.564 &\approx \frac{|\bar{u}'_{B0}|\bar{\gamma}_1 - \bar{\alpha}_0^2}{|\bar{u}'_{B0}|\bar{\gamma}_1}, \end{aligned}$$

This gives

$$\begin{aligned} \bar{\gamma}_1 &\approx 2.297\mu_{B0}^{1/3}|\bar{\alpha}_0\bar{u}'_{B0}|^{2/3}, \\ \bar{\alpha}_0 &\approx (1.001)^{3/4}\mu_{B0}^{1/4}|\bar{u}'_{B0}|^{5/4}. \end{aligned}$$

In order to compare our asymptotic approximation to the numerical solutions of the previous Section, we consider an asymptotic expansion in terms of $c = \omega/\alpha$. We have that

$$\begin{aligned} 1 - \frac{\omega}{\alpha x_s} &= 1 - \frac{\omega_0 + \epsilon\omega_1 + \dots}{x_s\alpha_0(1 + \epsilon\alpha_1/\alpha_0 + \dots)}, \\ &= \epsilon \frac{\alpha_1 x_s - \omega_1}{\alpha_0 x_s} + \dots. \end{aligned}$$

Since $\omega_0 = x_s\alpha_0$. Now $\epsilon = \text{Re}^{-1/8}$ and $\text{R} = \delta x_s \text{Re}^{1/2}$, so we can express our dispersion relation in terms of the numerical Reynolds number R as

$$\begin{aligned} 1 - \frac{\omega}{\alpha x_s} &= \delta^{1/4} \text{R}^{-1/4} x_s^{1/4} \frac{\alpha_1 x_s - \omega_1}{\alpha_0 x_s} + \dots, \\ &= \text{R}^{-1/4} \frac{\bar{\gamma}_1}{\bar{\alpha}_0}. \end{aligned} \quad (5.21)$$

So that for two-dimensional disturbances we obtain the following approximation

$$1 - \frac{\omega}{\alpha x_s} = \frac{2.297}{(1.001)^{1/4}} \mu_{B0}^{1/4} |\bar{u}'_{B0}|^{1/4} \delta^{1/4} \text{R}^{-1/4}. \quad (5.22)$$

In Figure 5.3 we see that the numeric and asymptotic solutions are in excellent agreement for the range of values of m tested. While it is unusual to see such good agreement between numeric and asymptotic solutions in such stability problems with only the leading order term in the expansion, it may be explained by the largeness of the Reynolds numbers under consideration compared to other boundary layers. The same can also be said for the isothermal analysis in

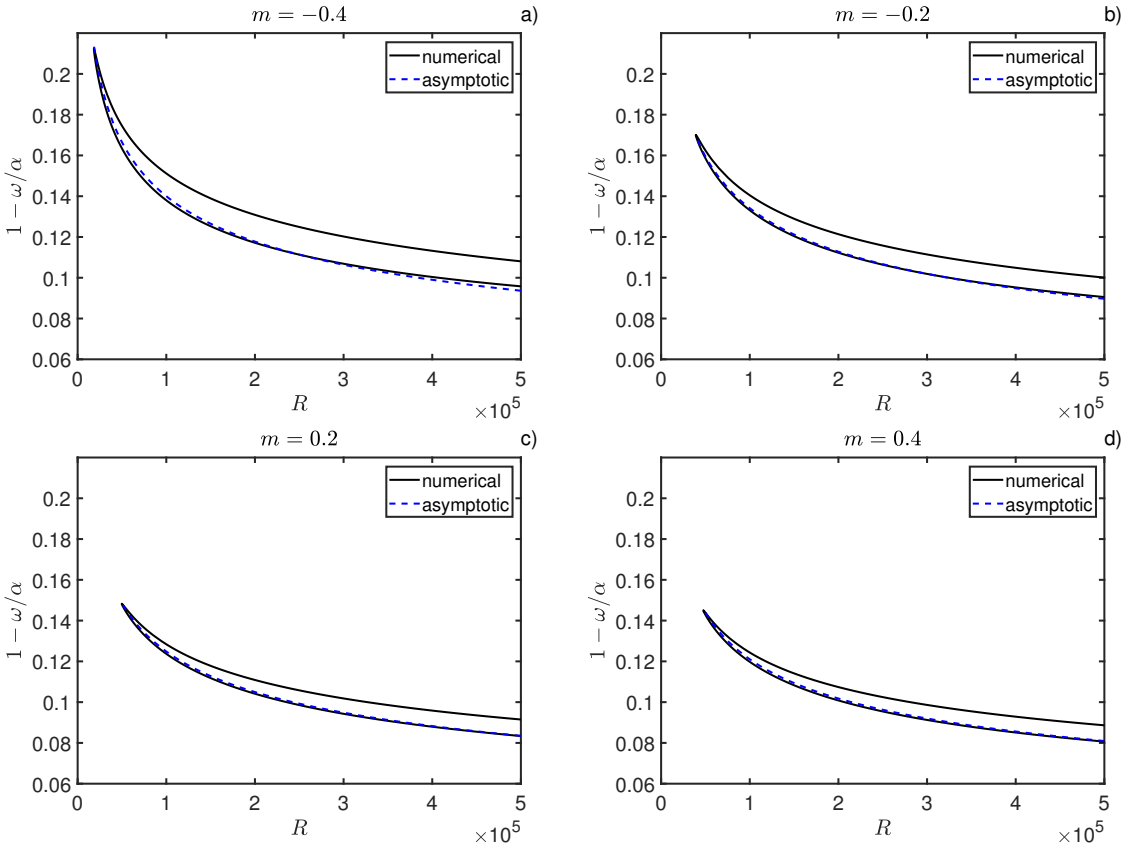


Figure 5.3: Comparison of the asymptotic prediction (5.22) and the numerical solution of (4.5) of the neutral curves for different values of the sensitivity parameter m . In $m = -0.4, -0.2, 0.2$ and 0.4 in a), b), c) and d) respectively.

Griffiths *et al.* [39] where the two curves are also in excellent agreement.

5.3 Discussions and Conclusions

In this Chapter, we have derived leading order solutions to the lower branch eigenrelation for the temperature dependent extension of Crane's problem. In doing so we have validated our numerical solutions of the previous Chapter, as evidenced by the excellent agreement between our asymptotic and numerical eigenvalue calculations, which is illustrated in Figure 5.3. Furthermore, both methods independently highlight the significance of the wall normal derivative of the basic streamwise velocity. In the energy analysis this appears in the EPRS term and is responsible for the destabilisation of the flow for $m > 0.34$. According to our asymptotic analysis, the primary effect on flow stability of imposing a temperature gradient and coupling the temperature and flow fields is primarily a result of the distortion of the shear stress on the surface on the sheet. This suggests that any flow control technique which alters the shear stress is capable of changing the stability characteristics of the flow. This observation is common among boundary layers and has led to the adoption of many active flow control strategies, such as wall suction [76], as well as passive techniques such as wall porosity [17] and compliance [16]. From an industrial perspective, these strategies can be challenging to implement and are not particularly suited for extrusion processes. However, alternative strategies, such as altering the properties of the ambient fluid medium, may prove useful, as suggested by our analysis.

Here we chose to use an inverse relationship between viscosity and temperature to facilitate comparison with other results in the literature [77], [78]. However, the asymptotic results derived are general in the sense that regardless of the specific form of viscosity temperature relationship imposed, the flow stability characteristics can be predicted provided the sheet shear stress can be accurately calculated. Therefore, our analysis can be easily adapted to account for more realistic, empirically derived viscosity functions, which would better match industrial or experimental conditions.

A potential criticism of the stability analysis conducted thus far is that despite the sheet being stretched, we have used parallelisation arguments based on a large Reynolds number to perform a local analysis. Although this approach has been somewhat justified by its success in the rotating disk case, as demonstrated in the work of Lingwood [67], it has not yet been validated for the case of stretching sheets. It is important to emphasise that this is an idealised flow configuration which fails to account for surface curvature, which would be required to conserve mass for any stretching sheet. Consequently, the results presented are approximations that are only valid in a high Reynolds number, small deformation regime. Nevertheless, this approach allows us to predict regimes that are more susceptible to the TS disturbances considered thus far. While a comprehensive analysis of the full system is beyond the scope of this thesis, questions regarding

the implications of these additional physical effects will be revisited in Chapter 8.

As stated previously, the results of Vlegaar indicate that the model we have chosen to use is capable of describing the behaviour of the boundary layer to within half a meter of the inlet. Using parameters from Vlegaar's study, this leads us to a maximum local Reynolds number which is many orders of magnitude smaller than the critical Reynolds number predicted in the previous Chapter. Whether this discrepancy is reduced when additional physical effects such as streamwise variations in sheet thickness and temperature are included remains to be seen. For this reason, the modal mechanism we have considered cannot be completely discarded, and it may be the case that temperature still has a significant quantitative effect. However, in the Chapter which follows we shall investigate, whether the simple models utilised for the stability analysis thus far, offer any plausible transition scenarios without resorting to non-local analysis.

Chapter 6

Non Modal Stability

The modal or eigenvalue based stability analysis of the previous two Chapters determines the stability of a system subject to small perturbations in the asymptotic, large time limit. Non modal stability theory on the other hand looks for transient energy amplification on a much shorter timescale. It was originally proposed as a mechanism to resolve discrepancies between linear stability theory and experiment in the case of Poiseuille flow. In plane Poiseuille flow, instabilities are observed experimentally at Reynolds numbers much smaller than predicted by modal linear stability analysis. While boundary layers are typically better described by modal stability analysis, given the largeness of the critical Reynolds numbers that have been found for the flow induced by a stretching sheet, it seems unreasonable that the flow would remain stable at such large Reynolds numbers. It is this which has caused us to search for alternative energy growth mechanisms for Crane's flow.

6.1 Introduction

Reynolds number estimates for flows induced by extrusion processes will obviously vary widely depending on the process under consideration. However, for cast film extrusion, draw speeds of tens of meters per second are not uncommon [58]. If we further presume that the length scale of the boundary layer to be of order millimetres, and take the approximate value of the kinematic viscosity of air to be $1.5 \times 10^{-5} \text{m}^2 \text{s}^{-1}$, this leaves us with an order of magnitude estimate for the Reynolds number of approximately $R \sim \mathcal{O}(500)$. This is clearly significantly smaller than the critical Reynolds numbers reported in Chapter 4. However, it is still large enough for the boundary layer approximation, upon which our analysis is based upon to be valid. In addition, we will also show that it is large enough for non modal instability mechanisms, which are introduced in this Chapter, to lead to the growth of energy in perturbations to Crane's basic

flow state. Mechanistically, this is an entirely different route to destabilisation than previously considered. However, both modal and non modal mechanisms have been found to compete in different regimes for certain flow regimes, as seen in Hack and Zaki [42], where the boundary layer induced by spanwise wall oscillations is studied. Here modal mechanisms dominate when the amplitude of wall oscillations is sufficiently large. For Crane's flow in the absence of temperature effects, we will show that the non-modal mechanism appears to dominate, however, this may not be that case as additional physical effects such as temperature are incorporated into the model.

The linear stability theory approach adopted throughout this thesis has seen mixed success when compared to experiments. For instance, it performs well in describing the stability of Rayleigh-Bènard convection, that being the buoyancy driven instability of fluid between two plates being heated from below [90]. For bounded shear flows such as plane Poiseuille flow, linear stability theory predicts a critical Reynolds number of $R = 5722$ [83], but turbulence is observed in experiments at $R \approx 1000$ [25]. The same can be said for other related flows such as pipe Poiseuille flow and Couette flow as outlined in the review in Trefethen *et al.* [110]. On the surface it appears that the cases where the eigenvalue analysis of linear stability theory fails are those to which the theory is most applicable in that the basic flows are exact and parallel. The key factor which distinguishes Rayleigh Bènard convection from Poiseuille flow is the normality of the linearised operators [110].

A matrix or operator is said to be normal if its eigenfunctions are mutually orthogonal [59]. While this is the case for Rayleigh Bènard convection, it is shown in Reddy *et al.* [91] that this property does not hold true for Poiseuille or Couette flows. An implication of this non-normality is the short term amplification of disturbance energy. While this does eventually decay, energy can be amplified by a factor of thousands, despite eigenvalues indicating flow stability ([41],[14]). One of the primary goals has been to identify the structure of the disturbances which maximise this transient energy growth. This too will be the focus for the remainder of this Chapter. First however, we will discuss the avenues from which this problem has been approached previously to justify the analysis which follows.

Due to the disagreement between theory and experiment, most of the early focus on non-modal stability has been on the bounded shear flows discussed above. These flows are characterised by a discrete set of eigenvalues. This allows arbitrary perturbations to be expanded as a weighted sum of eigenvectors and this property has been exploited for the majority of the early studies regarding this mechanism. For example in Schmid and Henningson [97], a formulation is presented which determines maximum energy growth over a given time period in terms of the matrix exponential of the discretised linear operator. The matrix exponential is computed by performing a singular value decomposition which accounts for the most prominent eigenmodes of the system. An issue with this scheme for boundary layers is that boundary layers are com-

prised of both a discrete and continuous spectrum as shown by Grosch and Salwen [40]. While it is possible to use a discrete approximation to the continuous spectrum as shown by Butler and Farrell [14], the continuous part of the spectrum is sensitive to changes in the number of collocation points and boundary layer mappings used [97]. To avoid these issues, we follow the analysis of Corbett and Bottaro [22] and employ a power iteration scheme which iteratively integrates the direct and adjoint equations. While we adopt the temporal formulation here, this power iteration approach has been applied in a spatial formulation in Luchini [69] by integrating the direct and adjoint linearised boundary layer equations.

Despite the variety of approaches adopted, common structures have been found to emerge. First is the Reynolds number dependence of both the maximum energy growth and the time taken for this growth to occur. The energy growth is found to scale with R^2 and the time scales with R across a variety of flow regimes in the temporal formulation. Another commonality is the fact that the most amplified disturbances are found in the long wavelength ($\alpha \rightarrow 0$) limit. This directly corresponds to experimental evidence of disturbances which manifest as streamwise oriented streaks and had to be actively controlled in the vibrating ribbon experiments of Klebanoff *et al.* [63]. Initially these streaks start out as streamwise oriented vortices which move fluid from a region of high streamwise velocity to lower velocity or vice versa. This in turn appears as a perturbation of the basic streamwise velocity which grows as it is advected downstream.

The three dimensionality of these structures is in direct contrast to the vast majority of two dimensional modal analyses which cite Squires theorem as a justification for ignoring three dimensional effects. This is because Squires theorem states that if a flow has an unstable three dimensional mode for some Reynolds number, then it has an unstable two dimensional eigenmode at some lower value of the Reynolds number [101]. As we will see this is no longer valid for the non modal instability mechanism.

6.2 Isothermal Stretching Sheet

In the modal analysis the additional terms appearing in the linearised Navier-Stokes equations had minimal impact on the growth rates of the system. Here our aim is to investigate whether or not these terms become important in the non-modal analysis. The idea being that non modal growth mechanisms arise at Reynolds numbers which are orders of magnitude smaller and perhaps these terms will have a greater influence. In the interest of clarity, we conduct this analysis in the absence of temperature dependent viscosity. This will allow us to identify the importance of this mechanism, while also facilitating comparison with results from the literature.

Starting with the dimensional continuity and Navier-Stokes equations we have

$$\nabla \cdot \mathbf{u}^* = 0, \quad (6.1a)$$

$$\rho^* \frac{D\mathbf{u}^*}{Dt^*} = -\frac{1}{\rho^*} p^* + \nu^* \nabla^2 \mathbf{u}^*. \quad (6.1b)$$

The velocity, pressure and time scales are $a^* x_s^*$, $\rho^* (a^* x_s^*)^2$ and $L^*/a^* x_s^*$, where $L^* = \sqrt{\nu^*/a^*}$ is the non-dimensionalising length scale. This is in contrast to the scaling for the temperature dependent case as there the boundary layer thickness is not constant. The mean flow quantities are perturbed as follows

$$u = \frac{x}{R} U(y) + \tilde{u}, \quad (6.1c)$$

$$v = \frac{1}{R} V(y) + \tilde{v}, \quad (6.1d)$$

$$w = \tilde{w}, \quad (6.1e)$$

$$p = \frac{1}{R^2} P(y) + \tilde{p}, \quad (6.1f)$$

where the basic flow terms are exact solutions to the Navier-Stokes equations and are given by

$$U = e^{-y}, \quad V = e^{-y} - 1, \quad P = P_0 + \frac{1 - e^{-2y}}{2}.$$

The Reynolds number is defined as $R = x_s^* a^* L^*/\nu^* = x_s^*/L^* = x_s$ and is equivalent to the dimensionless streamwise location. Thus the stability analysis is performed at a local x location where the variable x is replaced by the Reynolds number as for the temperature dependent problem. Since we seek to evaluate the short term time growth of the disturbances we proceed by expanding our perturbation variables as follows

$$\tilde{q} = \hat{q}(y, t) e^{i(\alpha x + \beta z)},$$

so that rather than assuming a disturbance frequency using Fourier transforms, the temporal evolution of the disturbances are explicitly integrated. Our linearised Navier Stokes equations become

$$i\alpha \hat{u} + \hat{v}' + i\beta \hat{w} = 0, \quad (6.2a)$$

$$\frac{\partial \hat{u}}{\partial t} + i\alpha U \hat{u} + \frac{1}{R} V \hat{u}' + U' \hat{v} + \frac{1}{R} U \hat{u} + i\alpha \hat{p} - \frac{1}{R} \Delta \hat{u} = 0, \quad (6.2b)$$

$$\frac{\partial \hat{v}}{\partial t} + i\alpha U \hat{v} + \frac{1}{R} V \hat{v}' + \frac{1}{R} V' \hat{v} + \hat{p}' - \frac{1}{R} \Delta \hat{v} = 0, \quad (6.2c)$$

$$\frac{\partial \hat{w}}{\partial t} + i\alpha U \hat{w} + \frac{1}{R} V \hat{w}' + i\beta \hat{p} - \frac{1}{R} \Delta \hat{w} = 0, \quad (6.2d)$$

where $\Delta = \mathcal{D}^2 - k^2$ is the Laplacian, with $k^2 = \alpha^2 + \beta^2$. The equations above may be combined to give an Orr-Sommerfeld Squire system of the form

$$\begin{aligned} \left[\left(\frac{\partial}{\partial t} + i\alpha U - \frac{1}{R} \Delta \right) \Delta - i\alpha U'' + \frac{1}{R} \left(V \Delta \frac{\partial}{\partial y} + V' \Delta + \frac{\alpha^2}{k^2} \frac{\partial}{\partial y} \left(U \frac{\partial}{\partial y} \right) \right) \right] \hat{v} \\ + \frac{\alpha\beta}{k^2 R} \left[U' + U \frac{\partial}{\partial y} \right] \hat{\eta} = 0, \\ \left[i\beta U' - \frac{\alpha\beta}{k^2 R} U \frac{\partial}{\partial y} \right] \hat{v} + \left[\frac{\partial}{\partial t} + i\alpha U - \frac{1}{R} \Delta + \frac{1}{R} V \frac{\partial}{\partial y} + \frac{\beta^2}{k^2 R} U \right] \hat{\eta} = 0, \end{aligned}$$

where we have written the additional stretching terms, highlighted in blue, in terms of the wall normal and vorticity perturbations using the following relations

$$\hat{u} = \frac{1}{k^2} (i\alpha\hat{v}' - i\beta\hat{\eta}), \quad \hat{w} = \frac{1}{k^2} (i\beta\hat{v}' + i\alpha\hat{\eta}).$$

The system is solved subject to the following boundary conditions

$$\hat{v} = \frac{\partial \hat{v}}{\partial y} = \hat{\eta} = 0 \text{ at } y = 0, \quad \hat{v} \rightarrow \frac{\partial \hat{v}}{\partial y} \rightarrow \hat{\eta} \rightarrow 0 \text{ as } y \rightarrow \infty.$$

Comparing the above system to Equation (2) in Corbett and Bottaro [22] we see a number of additional terms which appear due to the action of the stretching sheet all of which are $\mathcal{O}(R^{-1})$. Since the critical Reynolds number for the modal analysis is of the order of fifty thousand, removing these terms has minimal impact on the eigenvalues of the system. However, since we expect transient energy amplification at Reynolds numbers which are orders of magnitude smaller, we will include them in our analysis and compare the results to those obtained using the standard Orr-Sommerfeld Squire system. This simply means omitting the terms in blue above. As we will see this leads to a fundamental change in the structure of the optimisation problem and the question remains as to which formulation leads more suitably describes the underlying physics of the problem. Writing the system in matrix form we have

$$\frac{d}{dt} \Phi \mathbf{v} = \Lambda \mathbf{v}, \tag{6.3a}$$

where

$$\Lambda = \begin{bmatrix} \Lambda_{11} & \Lambda_{12} \\ \Lambda_{21} & \Lambda_{22} \end{bmatrix}, \quad \Phi = \begin{bmatrix} \Phi_{11} & 0 \\ 0 & \Phi_{22} \end{bmatrix}. \tag{6.3b}$$

The block matrices are defined as follows

$$\begin{aligned}\Phi_{11} &= \Delta, & \Phi_{22} &= \mathbf{I}, \\ \Lambda_{11} &= \left(-i\alpha U + \frac{1}{\mathbf{R}}\Delta\right)\Delta + i\alpha U'' - \frac{1}{\mathbf{R}}\left(V\Delta\frac{\partial}{\partial y} + V'\Delta + \frac{\alpha^2}{k^2}\frac{\partial}{\partial y}\left(U\frac{\partial}{\partial y}\right)\right), \\ \Lambda_{12} &= -\frac{\alpha\beta}{k^2\mathbf{R}}\left[U' + U\frac{\partial}{\partial y}\right], & \Lambda_{21} &= -i\beta U' + \frac{\alpha\beta}{k^2\mathbf{R}}U\frac{\partial}{\partial y}, \\ \Lambda_{22} &= -i\alpha U + \frac{1}{\mathbf{R}}\left(\Delta - V\frac{\partial}{\partial y} - \frac{\beta^2}{k^2}U\right),\end{aligned}$$

and $\mathbf{v} = [\hat{v}, \hat{\eta}]^T$. It is from this equation that the Orr-Sommerfeld-Squire solutions in Figure 4.5 were obtained. The generalised eigenvalue problem may simply be written $(\mathbf{\Lambda} + i\omega\mathbf{\Phi})\mathbf{v} = 0$. Note that the additional terms which appear due to surface stretching have been highlighted in blue. Note also that Λ_{12} is identically zero for non-stretching boundary layer flows.

6.3 Non-Model Analysis

Following Corbett and Bottaro [22], we seek the initial conditions to the initial value problem defined in equation (6.3a), which maximise the growth in kinetic energy over the interval $[0, \tau]$. The kinetic energy, defined in primitive variables is proportional to

$$2E(t) = (\mathbf{u}, \mathbf{u}) = \int_0^\infty \mathbf{u}^\dagger \mathbf{u} \, dy$$

and is the inner product of the perturbation velocity with itself, with the superscript \dagger denoting the complex conjugate transpose. If scale by the perturbation kinetic energy by the initial energy we attain

$$G(t) = \frac{E(t)}{E(0)},$$

and it is this quantity that we seek to maximise. Note that an equivalent definition of kinetic energy in terms of the wall normal velocity and vorticity is

$$E(t) = \frac{1}{k^2} \int_0^\infty -v^\dagger \Delta v + \eta^\dagger \eta \, dy.$$

We employ a power iteration scheme to maximise this quantity. This process can be broken into four distinct steps

1. Integrate the direct equation forward in time from $t = 0$ to $t = \tau$.
2. Convert from direct to adjoint variables.
3. Integrate the adjoint equations backwards in time from $t = \tau$ to $t = 0$.
4. Convert from adjoint variables back to direct variables.

To proceed we must first determine the adjoint of (6.3a)

6.3.1 Derivation of the Adjoint

In order to derive the appropriate adjoint equations, we must perform integration by parts on the direct Orr-Sommerfeld Squire system. As such it proves useful to first write the system in the equivalent form

$$\mathbf{A}_0 \frac{\partial \mathbf{v}}{\partial t} + \mathbf{A}_1 \frac{\partial^3 \mathbf{v}}{\partial t \partial y^2} = \mathbf{B}_0 \mathbf{v} + \mathbf{B}_1 \frac{\partial \mathbf{v}}{\partial y} + \mathbf{B}_2 \frac{\partial^2 \mathbf{v}}{\partial y^2} + \mathbf{B}_3 \frac{\partial^3 \mathbf{v}}{\partial y^3} + \mathbf{B}_4 \frac{\partial^4 \mathbf{v}}{\partial y^4}, \quad (6.4)$$

where the components of the operators are easily recovered from the Orr-Sommerfeld Squire system and are as follows

$$\begin{aligned} \mathbf{A}_0 &= \begin{bmatrix} -k^2 & 0 \\ 0 & 1 \end{bmatrix} & \mathbf{A}_1 &= \begin{bmatrix} 1 & 0 \\ 0 & 0 \end{bmatrix} \\ \mathbf{B}_0 &= \begin{bmatrix} i\alpha(U'' + k^2U) + \frac{k^2}{\mathbf{R}}(k^2 + V') & -\frac{\alpha\beta}{k^2\mathbf{R}}U' \\ -i\beta U' & -i\alpha U - \frac{1}{\mathbf{R}}(k^2 + \frac{\beta^2}{k^2}U) \end{bmatrix} & \mathbf{B}_1 &= \begin{bmatrix} \frac{1}{\mathbf{R}}(k^2V - \frac{\alpha^2}{k^2}U') & -\frac{\alpha\beta}{k^2\mathbf{R}}U \\ \frac{\alpha\beta}{k^2\mathbf{R}}U & -\frac{1}{\mathbf{R}}V \end{bmatrix} \\ \mathbf{B}_2 &= \begin{bmatrix} -i\alpha U - \frac{1}{\mathbf{R}}(2k^2 + V' + \frac{\alpha^2}{k^2}U) & 0 \\ 0 & \frac{1}{\mathbf{R}} \end{bmatrix} & \mathbf{B}_3 &= \begin{bmatrix} -\frac{1}{\mathbf{R}}V & 0 \\ 0 & 0 \end{bmatrix} \\ \mathbf{B}_4 &= \begin{bmatrix} \frac{1}{\mathbf{R}} & 0 \\ 0 & 0 \end{bmatrix} \end{aligned}$$

Next we introduce our adjoint variables $\tilde{\mathbf{a}} = (\tilde{a}, \tilde{b})^T$. The adjoint equations are derived by scalar multiplying equation (6.4) by $\tilde{\mathbf{a}}$ and integrating over $[0, \tau] \times [0, \infty)$, applying integration by parts

$$\begin{aligned} 0 &= \int_0^\infty \int_0^\tau \tilde{\mathbf{a}}^\dagger \left[\mathbf{A}_0 \frac{\partial \mathbf{v}}{\partial t} + \mathbf{A}_1 \frac{\partial^3 \mathbf{v}}{\partial t \partial y^2} - \mathbf{B}_0 \mathbf{v} - \mathbf{B}_1 \frac{\partial \mathbf{v}}{\partial y} - \mathbf{B}_2 \frac{\partial^2 \mathbf{v}}{\partial y^2} - \mathbf{B}_3 \frac{\partial^3 \mathbf{v}}{\partial y^3} - \mathbf{B}_4 \frac{\partial^4 \mathbf{v}}{\partial y^4} \right] dt dy \quad (6.5) \\ &= \int_0^\infty \int_0^\tau \mathbf{v}^\dagger \left[-\mathbf{A}_0^\dagger \frac{\partial \tilde{\mathbf{a}}}{\partial t} - \mathbf{A}_1^\dagger \frac{\partial^3 \tilde{\mathbf{a}}}{\partial t \partial y^2} - \mathbf{B}_0^\dagger \tilde{\mathbf{a}} + \frac{\partial}{\partial y} (\mathbf{B}_1^\dagger \tilde{\mathbf{a}}) - \frac{\partial^2}{\partial y^2} (\mathbf{B}_2^\dagger \tilde{\mathbf{a}}) + \frac{\partial^3}{\partial y^3} (\mathbf{B}_3^\dagger \tilde{\mathbf{a}}) - \frac{\partial^4}{\partial y^4} (\mathbf{B}_4^\dagger \tilde{\mathbf{a}}) \right] dt dy \\ &+ \int_0^\infty \left[\mathbf{v}^\dagger \mathbf{A}_0^\dagger \tilde{\mathbf{a}} + \mathbf{v}^\dagger \mathbf{A}_1^\dagger \frac{\partial^2 \tilde{\mathbf{a}}}{\partial y^2} \right]_{t=0}^\tau + \left[\frac{\partial \mathbf{v}^\dagger}{\partial y} \mathbf{A}_1^\dagger \tilde{\mathbf{a}} - \mathbf{v}^\dagger \mathbf{A}_1^\dagger \frac{\partial \tilde{\mathbf{a}}}{\partial y} \right]_{t=0}^\tau \Big|_{y=0}^\infty \\ &\int_0^\tau -\mathbf{v}^\dagger \mathbf{B}_1^\dagger \tilde{\mathbf{a}} - \frac{\partial \mathbf{v}^\dagger}{\partial y} \mathbf{B}_2^\dagger \tilde{\mathbf{a}} + \mathbf{v}^\dagger \frac{\partial}{\partial y} (\mathbf{B}_2^\dagger \tilde{\mathbf{a}}) - \frac{\partial^2 \mathbf{v}^\dagger}{\partial y^2} \mathbf{B}_3^\dagger \tilde{\mathbf{a}} + \frac{\partial \mathbf{v}^\dagger}{\partial y} \frac{\partial}{\partial y} (\mathbf{B}_3^\dagger \tilde{\mathbf{a}}) - \mathbf{v}^\dagger \frac{\partial^2}{\partial y^2} (\mathbf{B}_3^\dagger \tilde{\mathbf{a}}) \\ &- \frac{\partial^3 \mathbf{v}^\dagger}{\partial y^3} \mathbf{B}_4^\dagger \tilde{\mathbf{a}} + \frac{\partial^2 \mathbf{v}^\dagger}{\partial y^2} \frac{\partial}{\partial y} (\mathbf{B}_4^\dagger \tilde{\mathbf{a}}) - \frac{\partial \mathbf{v}^\dagger}{\partial y} \frac{\partial^2}{\partial y^2} (\mathbf{B}_4^\dagger \tilde{\mathbf{a}}) + \mathbf{v}^\dagger \frac{\partial^3}{\partial y^3} (\mathbf{B}_4^\dagger \tilde{\mathbf{a}}) dt \Big|_{y=0}^\infty. \quad (6.6) \end{aligned}$$

Boundary conditions for the adjoint equations may be derived by requiring that the boundary terms (in y) are identically zero. Expanding these terms, taking into account the boundary

conditions on the direct variables and base flows we have

$$\begin{aligned} & \int_0^\tau -\frac{\partial \mathbf{v}^\dagger}{\partial y} \mathbf{B}_2^\dagger \tilde{\mathbf{a}} - \frac{\partial^2 \mathbf{v}^\dagger}{\partial y^2} \mathbf{B}_3^\dagger \tilde{\mathbf{a}} + \frac{\partial^2 \mathbf{v}^\dagger}{\partial y^2} \frac{\partial}{\partial y} (\mathbf{B}_4^\dagger \tilde{\mathbf{a}}) - \frac{\partial^3 \mathbf{v}^\dagger}{\partial y^3} \mathbf{B}_4^\dagger \tilde{\mathbf{a}} d\tau \Big|_{y=0}^\infty \\ &= \int_0^\tau -\frac{1}{R} \frac{\partial \hat{\eta}^\dagger}{\partial y} \tilde{b} - \frac{1}{R} V \frac{\partial^2 \hat{v}^\dagger}{\partial y^2} \tilde{a} + \frac{1}{R} \frac{\partial^2 \hat{v}^\dagger}{\partial y^2} \frac{\partial \tilde{a}}{\partial y} - \frac{1}{R} V \frac{\partial^3 \hat{v}^\dagger}{\partial y^3} \tilde{a} d\tau \Big|_{y=0}^\infty. \end{aligned} \quad (6.7)$$

It is clear that these terms are zero if we impose the same boundary conditions as for the direct problem *i.e.*

$$\tilde{a} = \frac{\partial \tilde{a}}{\partial y} = \tilde{b} = 0 \text{ at } y = 0, \quad \tilde{a} \rightarrow \frac{\partial \tilde{a}}{\partial y} \rightarrow \tilde{b} \rightarrow 0 \text{ as } y \rightarrow \infty.$$

Doing so ensures that each term in (6.7) is identically zero, both on the surface of the stretching sheet, and in the free-stream. We require that $\tilde{\mathbf{a}}$ satisfies the adjoint equation

$$-\mathbf{A}_0^\dagger \frac{\partial \tilde{\mathbf{a}}}{\partial t} - \mathbf{A}_1^\dagger \frac{\partial^3 \tilde{\mathbf{a}}}{\partial t \partial y^2} = \mathbf{B}_0^\dagger \tilde{\mathbf{a}} - \frac{\partial}{\partial y} (\mathbf{B}_1^\dagger \tilde{\mathbf{a}}) + \frac{\partial^2}{\partial y^2} (\mathbf{B}_2^\dagger \tilde{\mathbf{a}}) - \frac{\partial^3}{\partial y^3} (\mathbf{B}_3^\dagger \tilde{\mathbf{a}}) + \frac{\partial^4}{\partial y^4} (\mathbf{B}_4^\dagger \tilde{\mathbf{a}}), \quad (6.8)$$

which is given in terms of (\tilde{a}, \tilde{b}) as follows

$$\begin{aligned} -\frac{\partial}{\partial t} (\Delta \tilde{a}) &= \left[\left(i\alpha U + \frac{1}{R} \Delta \right) \Delta + 2i\alpha U' \frac{\partial}{\partial y} - \frac{\alpha^2}{k^2 R} \left(U' \frac{\partial}{\partial y} + U \frac{\partial^2}{\partial y^2} \right) \right. \\ &\quad \left. + \frac{1}{R} \left(V'' \frac{\partial}{\partial y} + 2V' \frac{\partial^2}{\partial y^2} + V \Delta \right) \right] \tilde{a} \\ &\quad + \left[i\beta U' - \frac{\alpha\beta}{k^2 R} \left(U' + U \frac{\partial}{\partial y} \right) \right] \tilde{b} \end{aligned} \quad (6.9a)$$

$$\begin{aligned} -\frac{\partial \tilde{b}}{\partial t} &= \left[-\frac{\alpha\beta}{k^2 R} U \frac{\partial}{\partial y} \right] \tilde{a} \\ &\quad + \left[i\alpha U + \frac{1}{R} \Delta - \frac{1}{R} \left(1 + \frac{\beta^2}{k^2} \right) U + \frac{1}{R} V \frac{\partial}{\partial y} \right] \tilde{b}. \end{aligned} \quad (6.9b)$$

We can write equation (6.9) in a compact form, equivalent to equation (6.3a), which is more convenient for numerical discretisation

$$\frac{d}{dt} \Phi^+ \mathbf{v} = \Lambda^+ \mathbf{v}, \quad (6.10)$$

$$\Phi^+ = \begin{bmatrix} \Phi_{11}^+ & 0 \\ 0 & \Phi_{22}^+ \end{bmatrix}, \quad \Lambda^+ = \begin{bmatrix} \Lambda_{11}^+ & \Lambda_{12}^+ \\ \Lambda_{21}^+ & \Lambda_{22}^+ \end{bmatrix}, \quad (6.11)$$

with

$$\begin{aligned}
\Phi_{11}^+ &= \Delta, & \Phi_{22}^+ &= I, \\
\Lambda_{11}^+ &= (-i\alpha U - \frac{1}{R}\Delta)\Delta - 2i\alpha U' \frac{\partial}{\partial y} \\
&+ \frac{1}{R} \left[-V\Delta \frac{\partial}{\partial y} + (1 + \frac{\alpha^2}{k^2}) U' \frac{\partial}{\partial y} + (2 + \frac{\alpha^2}{k^2}) U \frac{\partial^2}{\partial y^2} \right], \\
\Lambda_{12}^+ &= -i\beta U' + \frac{\alpha\beta}{k^2 R} (U \frac{\partial}{\partial y} + U'), \\
\Lambda_{21}^+ &= -\frac{\alpha\beta}{k^2 R} U \frac{\partial}{\partial y} \\
\Lambda_{22}^+ &= -i\alpha U - \frac{1}{R} \left[\Delta + V \frac{\partial}{\partial y} - (\frac{\beta^2}{k^2} + 1)U \right].
\end{aligned}$$

Where we have again highlighted the additional terms due to surface stretching in blue.

6.3.2 Numerical Scheme

Both the direct and adjoint equations are discretised using a Chebyshev spectral scheme as in Chapter 4. Time integration was performed using a second order backwards Euler scheme with a first order scheme used for the initial integration step. This is written for the direct scheme as

$$\frac{e_1}{dt} (\Phi - \Lambda) \mathbf{v}_{j+1} = -\frac{e_2}{dt} \Phi \mathbf{v}_j - \frac{e_3}{dt} \Phi \mathbf{v}_{j-1}, \quad (6.12)$$

where the subscript j indicates the current time step. The Euler coefficients are given by

$$e_1 = \frac{3}{2}, \quad e_2 = -2, \quad e_3 = \frac{1}{2}, \quad \text{for } j > 1, \quad (6.13)$$

$$e_1 = 1, \quad e_2 = -1, \quad e_3 = 0, \quad \text{for } j = 1. \quad (6.14)$$

The time step was defined as follows

$$dt = \frac{\tau}{\lceil \frac{\tau}{0.2} + 1 \rceil} \leq 0.2.$$

This was chosen so that our results would be consistent with those of Corbett and Bottaro [22], although a smaller timestep would improve the accuracy of our simulations at the cost of additional matrix inversions for each power iteration. Finally, in order to implement the scheme we need to relate our direct and adjoint variables at each iteration. These relationships are

defined as follows

$$\tilde{\mathbf{a}}(\tau)^k = \frac{1}{k^2}[-v(\tau)^k, \eta(\tau)^k]^T, \quad \mathbf{v}(0)^{k+1} = k^2[-\tilde{a}(0)^k, \tilde{b}(0)^k]^T,$$

and are given by Corbett and Bottaro [22]. With this we can now impose a wavenumber pair (α, β) and the Reynolds number R , and integrate the Orr-Sommerfeld Squire system with arbitrary initial conditions, over an arbitrary time interval $(0, \tau)$ to find the initial conditions which maximises energy growth $G(\tau)$ over this time interval. This is defined to be a local optimal

$$\sigma(\tau) \equiv \max_{\forall v_0(\alpha, \beta)} G(\tau).$$

A global optimal is defined as the maximum growth obtainable for given wavenumber pair. It is the growth obtained at the time t_γ , for which σ is maximised and is defined as follows

$$\gamma = \max_{\forall t} \sigma(t),$$

Finally the largest transient growth possible for a given base Reynolds number is termed the maximal optimal and is defined as follows

$$\Gamma = \max_{\forall \alpha, \beta} \gamma(t_\gamma).$$

It is found by maximising γ over all possible wavenumber pairs. We are primarily interested in determining this quantity. To clarify, calculating σ involves finding the initial conditions which maximise energy growth for an arbitrary time interval and wavenumber pair. The calculation of γ requires us to determine the time interval which maximises energy growth, given a wavenumber pair. Finally Γ involves finding the wavenumber pair which maximise γ . An interesting property of such problems is that Γ is consistently found to occur in the $\alpha \rightarrow 0$ limit ([34],[22],[14]). Another property of note is that the spanwise wavenumber which attains the maximum optimal remains constant when the boundary layer is scaled by the momentum thickness, rather than the boundary layer thickness used in Chapter 4, for both the Falkner-Skan [22] and asymptotic suction boundary layers [34]. This distinction is important for the isothermal stretching sheet as due to the nature of our basic flow solutions, the momentum thickness is half the boundary layer thickness. This is not generally the case and is due to the analytical, exponentially decaying streamwise velocity profile for Crane's flow. With these features noted, the procedure for finding the maximal optimal Γ is as follows.

We begin by choosing an arbitrary value of the Reynolds number, typically $R \sim 100$. Chosen to be large enough to justify the boundary layer approximation, while not so large to slow the power iteration scheme since $\tau \sim R$. Next, we employ our power iteration scheme for a range of β values using Matlab's `fminbnd` function to find the global optimal γ for each value of β .

`fminbnd` uses a combination of golden Section search and parabolic interpolation to find the time that maximises G . From this we can estimate a maximum optimal Γ , with corresponding β_Γ and t_Γ . To more accurately resolve the maximum optimal we use Matlab's `fminsearch` which varies both β and t and uses a simplex search method to maximise the growth in kinetic energy. These derivative-free methods are preferred over Newton-type optimisation schemes, as to calculate derivatives using finite differences numerically, more calls to the original direct adjoint scheme have to be called. This typically takes $\sim 5 - 6$ iterations to converge. With a time step of approximately 0.2, considering our validation test case in the next Section, we have

$$870/0.2 \times 2 \times 5 \approx 43500$$

matrix inversions (*i.e.* equation (6.12)) to perform, for a single power iteration to converge. The derivative-free schemes that we have implemented, reduce the number of iterations required to maximise the energy causing significant reduction in overall computational time and effort.

6.4 Numerical Results

In this Section, we present the results of our calculations across several different cases. We begin by validating our numerical solver through the computation of optimal perturbations for the Blasius boundary layer, comparing our findings with those reported in [22]. Following the validation, we shift our focus to Crane's flow. Initially, we compute the optimal perturbations by solving the standard Orr-Sommerfeld-Squire system (OSSQ) without the inclusion of the additional terms that arise due to surface stretching. These OSSQ results provide a baseline for comparison. We then incorporate the extra stretching terms (EST) into our calculations and re-solve the system. The inclusion of these terms introduces significant changes to the behaviour of the initial value problem (IVP) compared to the OSSQ formulation. We observe that the EST fundamentally alters the dynamics of the system in ways that are not reflected in the traditional modal analysis. This change in behaviour between the OSSQ and EST cases raises the question of which formulation offers a more accurate description of the system's dynamics? This question will be revisited in our conclusions.

6.4.1 Validation

To validate the solver we chose to compare our results to those of Corbett and Bottaro [22] for the Blasius boundary layer. This amounts to iteratively solving equations (6.3a) and (6.10), while omitting the additional terms which appear due to surface stretching. The basic flow

Table 6.1: Comparison of the maximum optimal computed for Blasius flow scaled by the momentum thickness to the results of Corbett and Bottaro [22].

	β_θ	Γ	t_Γ
[22]	0.25114	280.7	870.8
Present analysis	0.25144	279.52	865.06
% error	0.12%	0.42%	0.66%

$U(y) = f'$ is determined by the solution of the Blasius ODE

$$f''' + \frac{1}{2}ff'' = 0,$$

subject to the boundary conditions

$$f(0) = f'(0) = 0, \quad f' \rightarrow 1 \text{ as } y \rightarrow \infty,$$

and may be numerically solved using the shooting method scheme outlined in Chapter 3. The wall normal coordinate is scaled using the momentum thickness, which is defined as

$$\theta = \int_0^\infty U(1 - U) dy \approx 0.664.$$

With this basic flow and scaling we can implement our optimisation procedure to calculate the maximum optimum for $R_\theta = 166$. The Reynolds number is defined $R_\theta = U_\infty^* L^* / \nu^*$, where U_∞^* is the dimensional free-stream velocity, ν^* the kinematic viscosity and $L^* = l^* \theta$ is the non dimensional length scale l^* , scaled by the momentum thickness. The particular value of the Reynolds number is chosen to compare to results reported in by Corbett and Bottaro [22] in table 6.1. Here we see that for each quantity predicted, the spanwise wavenumber, the energy growth and the time at which this energy growth is achieved, our solver corroborates the results of [22] with relative errors of $< 1\%$. We also show the structure of the maximum optimums in Figure 6.1. Here we see the substantial relative growth in magnitude of the streamwise velocity perturbation compared to the spanwise and wall-normal components. Qualitatively similar observations are made across a wide variety of flow regimes in which the basic flow is two dimensional from boundary layers ([22],[14]), to the bounded shear flows discussed in this Chapters introduction ([110],[41]).

6.4.2 Crane OSSQ

Having validated our optimisation scheme for the Blasius boundary layer, we now shift our focus to Crane's flow. Given the minimal differences observed when including the additional

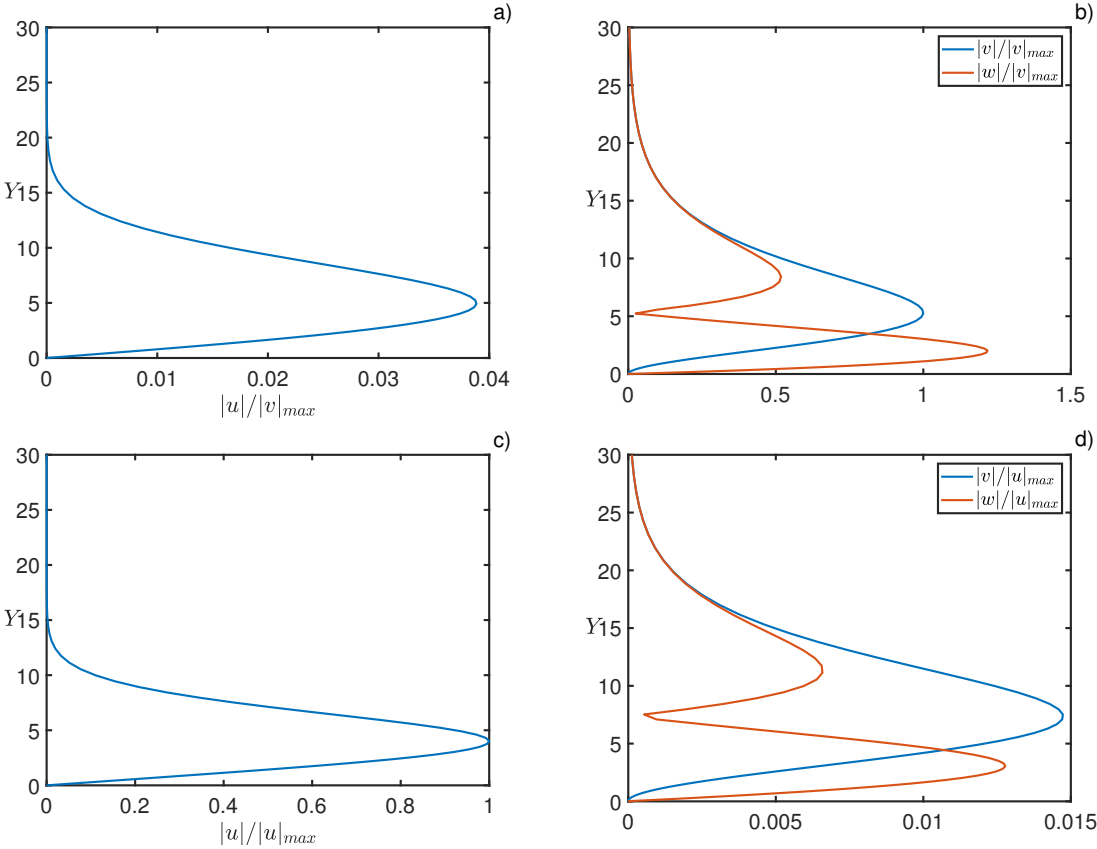


Figure 6.1: Maximum optimum for the Blasius boundary layer for $R_\theta = 166$, $\beta_\theta = 0.25144$. Initial conditions a) & b) and final perturbations c) & d). Note the wall normal coordinate is scaled such that $Y = y/\theta$.

Table 6.2: Comparison of the maximum optimal computed for Crane’s flow, with and without stretching terms to the results of Fransson and Corbett [34] for the asymptotic suction boundary layer (ASBL). The substantial difference when the extra stretching terms are included is discussed in the next Section.

	β	$\Gamma \times 10^3 R^2$	$t_\Gamma R$
Crane OSSQ	0.51	0.95	1.25
Crane EST	0.79	0.55	0.51
ASBL [34]	0.53	0.99	1.48

stretching terms in the modal analysis, we begin by solving the standard Orr-Sommerfeld-Squire system, replacing the Blasius basic flow with the exponentially decaying basic flow of Crane [23]. By applying the same optimisation procedure as for the Blasius boundary layer, we report the Reynolds number dependence of the maximal optimal energy growth (Γ) and the time (t_Γ) at which it occurs. These Figures are provided in table 6.2, where they are compared to the results of Fransson and Corbett [34] for the asymptotic suction boundary layer (ASBL). The ASBL is an extension of the Blasius boundary layer and is obtained by applying uniform suction on the surface of the plate downstream from the leading edge. Assuming that the wall-normal velocity component V is constant and that $V \sim R^{-1}$, attained by applying the usual boundary layer scaling arguments, the x momentum equation may be directly integrated to obtain

$$U = 1 - e^{-y}.$$

Considering the qualitative similarities in the basic flow profiles, particularly the exponentially decay of the streamwise velocity component and a wall normal velocity of $\mathcal{O}(R^{-1})$, the maximal optima are largely in agreement with the additional stretching terms excluded. This is also true for the critical Reynolds numbers reported in the modal analysis, both of which are approximately 5×10^4 .

To visualise the structure of the optimal perturbations we plot the perturbations in real space in Figure 6.2. Utilising the same scalings as for the Blasius case in Figure 6.1 for the streamwise velocity perturbation, we can clearly see the lift-up effect going from the initial condition a) to the maximum optimum in b). Here this manifests as an upwards shift of the centre of the vortices with a corresponding increase in the magnitude of the streamwise velocity perturbation. This perturbation structure was first noted by Landahl [65] in the context of inviscid algebraic instabilities but is equally observed for the short-time stability of two-dimensional viscous flows. Similar visualisations are presented for the ASBL [34]. Note that the arrows in the quiver plot are not to scale and are intended for illustrative purposes only.

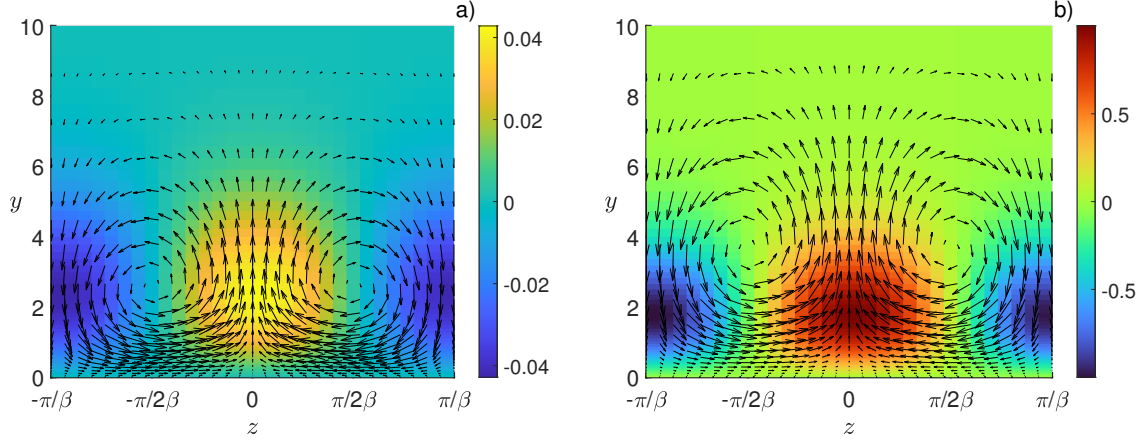


Figure 6.2: Quiver plot of the wall-normal and spanwise optimum perturbation for Crane's flow at $R = 500$, with colours indicating the magnitude of the streamwise velocity component. Scalings correspond to those in Figure 6.1, with different colour schemes used to indicate the different scalings used at the initial and final times. a) The initial condition and b) the maximum optimum evaluated at $t = t_\Gamma$.

6.4.3 Crane EST

In the previous Section we compared the results for Crane's flow to those of the ASBL due to the similarities between them. However, an important distinction between the two cases is that the additional terms in the ASBL arise from the wall suction boundary condition imposed on the basic flow. Consequently, all additional terms are constant, of $\mathcal{O}(R^{-1})$, and have minimal impact, even on the non-modal stability of the system. In contrast, for Crane's flow, the wall-normal velocity terms depend on the wall-normal coordinate, and we also encounter non-zero x -derivatives of the streamwise basic flow component due to the action of the stretching sheet. The significance of these extra stretching terms, as evidenced by the large disparity in the maxima reported in table 6.2, will be explored in this Section.

To understand these differences, it is instructive to evaluate the energy evolution of the local optima determined via power iteration for different time domains for both the OSSQ and EST cases. This evaluation is illustrated in Figure 6.3 where we observe that the standard OSSQ system a) behaves as expected. Specifically, for different time integration lengths, the power iteration converges to the initial condition which maximises energy growth over the given interval. In contrast, when considering the EST case, we see the power iteration returns the same initial conditions regardless of the length of time over which the equations are integrated. This fundamental change in behaviour explains the disparity between the maxima reported in table 6.2. This observation suggests that the additional stretching terms in the EST case impose a constraint on the optimisation process, leading to a uniform initial condition across various time

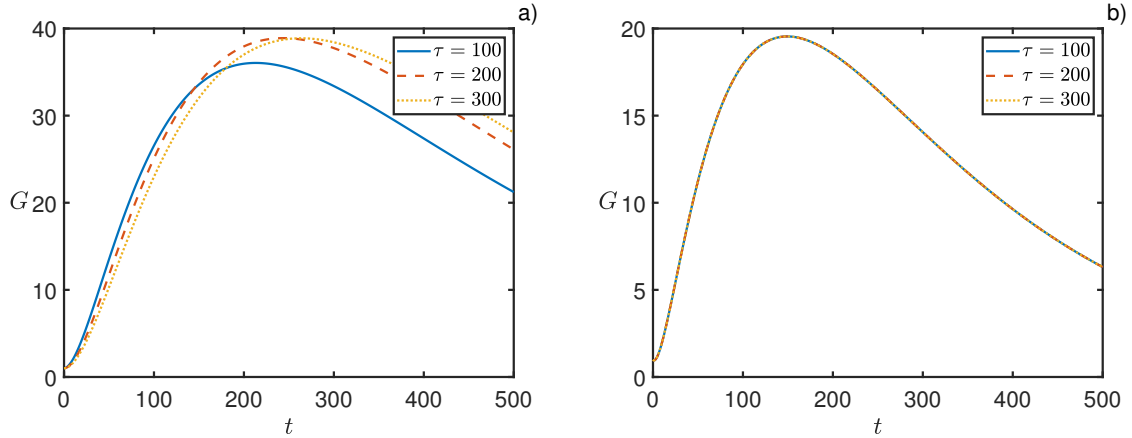


Figure 6.3: Local optima of the OSSQ a) and EST b) systems determined via power iteration for different time intervals. In both instances we fix $R = 200$, $\beta = 0.51$ and $\alpha=0$.

domains. Consequently, the differences in energy growth characteristics between the OSSQ and EST cases are not merely quantitative but also reflect a fundamental shift in the underlying dynamics of the flow stability problem.

From an optimisation perspective, the fact that the IVP appears to have a unique solution when the stretching terms are retained significantly reduces the computational complexity of calculating the maximum optimum. In this scenario, the optimisation procedure is simplified to determining the spanwise wavenumber β , only. Additionally, the direct-adjoint system only needs to be solved once for each value of β . Despite the significant changes in the structure of the solutions when the stretching terms are included, the Reynolds number scaling for both the maximum energy growth Γ and the time taken to achieve this growth t_Γ remains consistent. This scaling is illustrated in Figure 6.4 for both the OSSQ and EST cases. It is important to note that the differences in energy at $t = 0$ are due to the initial perturbation kinetic energy being scaled to one for each calculation.

The inclusion of the extra stretching terms in the analysis raises the question of whether they provide a more accurate description of the short-term instability dynamics for flows like Crane's flow. This remains an open question and warrants further investigation. One possible explanation for the observed differences could be that Crane's flow is an exact analytical solutions to the full Navier-Stokes equations, which might justify the inclusion of these higher-order basic flow terms in the stability analysis. To explore this further, a similar analysis could be conducted with the inclusion of temperature-dependent viscosity, as was done in Chapters 4 and 5. In the coupled, temperature-dependent scenario, where exact analytical solutions are no longer available, it would be interesting to see if the IVP continues to exhibit a unique initial condition over different time domains when using the power iteration method. This would help determine

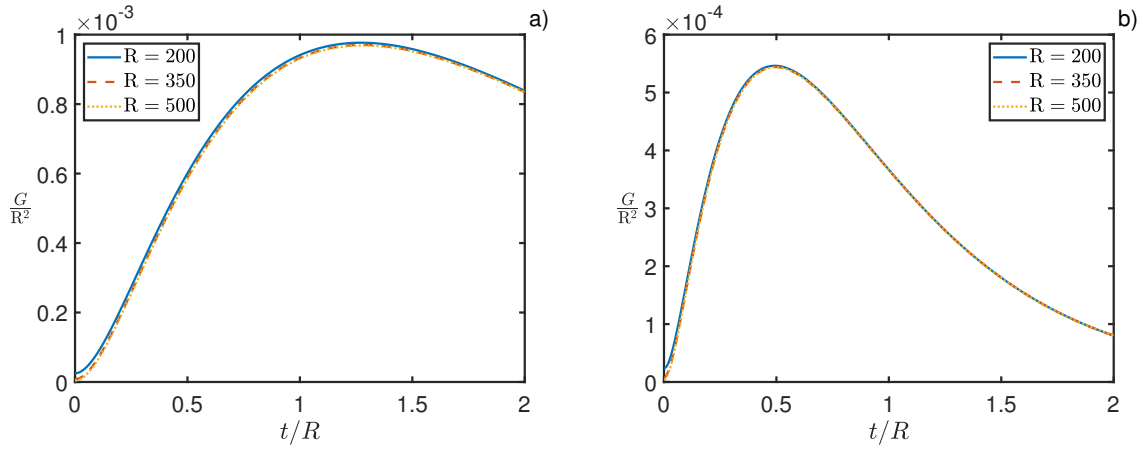


Figure 6.4: Maximum optima for different Reynolds numbers for a) OSSQ and b) EST. Parameter values correspond to those reported in table 6.2.

whether the unique behaviour observed with the stretching terms is due to the exact nature of Crane’s flow or if it is a more general characteristic of such stretching flows. However, due to time constraints, this line of investigation will not be pursued here.

6.5 Discussion and Conclusions

In this Chapter, we have explored the non-modal stability of isothermal flow driven by a stretching sheet, revealing significant potential for energy amplification at Reynolds numbers much lower than the critical values identified in modal analyses. This finding suggests that short-term energy growth presents a more realistic transition scenario for flows typically encountered in extrusion processes. Indeed, throughout this Chapter we have seen significant energy amplification occur within the domain of applicability of Crane’s model as per the work of Vlegaar [114], who provides a rough upper bound of $R \sim 400$ to be within half a meter of the inlet. After this point, assuming a linear stretching rate becomes untenable as the sheet accelerates exponentially.

Comparing our results to other boundary layers, the critical Reynolds number for the Blasius boundary layer, scaled by the displacement thickness, is for instance 519.4 [97]. This is approximately 100 times smaller than the critical Reynolds number for Crane’s flow both with and without the additional stretching terms. Conversely, the maximum transient energy growth in the Blasius boundary layer scales as $1.5 \times 10^{-3} R^2$ [14], whereas for Cranes flow it scales as 0.95×10^{-3} , and $0.55 \times 10^{-3} R^2$, with and without the extra stretching terms respectively. Despite the reduction in potential energy amplification, the fact that the critical Reynolds number is orders of magnitude larger for Crane’s flow means that the non-modal mechanism may develop long before the modal results take effect. This also explains the relative success of linear stability

theory in the Blasius case [47], compared to other bounded parallel flows such as Poiseuille flow [110].

A key aspect of our analysis is the consideration of higher-order basic flow terms. We have demonstrated that including these additional terms fundamentally changes the flow characteristics when compared to the modal analysis discussed in Chapter 4. Despite these changes, the observation that the extra stretching terms (EST) have a stabilizing effect on the maximum energy amplification, as indicated in table 6.2, aligns with the results of both the modal analysis of the stretching sheet in Chapter 4 and the findings of Malik *et al.* [73] for the rotating disk. For the rotating disk, the inclusion of higher order basic flow terms was justified by improved agreement with experimental results [64]. However, since Crane's flow represents an idealised flow regime, determining whether the EST are important requires a different means of validation, likely through the form of numerical simulations. The challenge lies in the fact that the most amplified energy amplification occurs in the long wavelength ($\alpha \rightarrow 0$) limit, and this regime is inaccessible to traditional direct numerical simulations. Despite this limitation, small finite values of the streamwise wavenumber could be investigated to assess the relevance and impact of the EST in Crane's flow. Such investigations would help determine whether these additional terms offer a more accurate description of the flow dynamics.

In Chapter 4, we analysed the spatial, rather than temporal stability problem for Crane's flow as it is generally deemed to be more appropriate for boundary layers. Similar arguments have been made for non-modal analysis, with two main approaches being adopted in the literature ([70],[5]). Both are based on the direct-adjoint integration of the linearised boundary layer equations. The approach of Luchini [70] is in a sense a simplification of the analysis of Andersson *et al.* [5], which uses boundary layer scaling arguments to simplify the analysis and impose additional inflow and outflow boundary conditions which reflect this scaling. The long wavelength limit of the maximum optima raises additional concerns about the validity of using parallelisation arguments in our present analysis. This could also be addressed by the spatial analysis, which could be adapted from these studies to account for the motion of the stretching sheet. However, spatial results for the Blasius boundary layer produce qualitatively similar results as the temporal analysis, indicating that the temporal approach effectively captures the key instability mechanisms. Further exploration through spatial analysis could offer a more detailed picture, but it is likely that the main conclusions regarding flow stability and transition would remain consistent.

As with the analyses conducted in previous Chapters, there remain several additional flow variables that have not yet been fully explored. Notably, temperature effects and the curvature of the sheet have yet to be considered. Including these factors could potentially alter our results particularly since the basic flow solutions are no longer exact analytical solutions. Despite these

omissions, our investigations have demonstrated that traditional modal analysis is unlikely to be the primary mechanism driving flow transition. Instead, the results suggest that non-modal mechanisms may play a more crucial role in the early stages of the transition process.

Chapter 7

Summary of Results

Throughout this thesis, we have proposed and analysed various models for flows induced by extrusion processes, extending the model of Crane [23] for the flow induced by a linearly stretched flat sheet. There are a number of features of Crane's flow which make it amenable to analysis using the tools of boundary layer theory. Under Crane's assumptions, the flow admits an exact analytical solution of the full Navier-Stokes equations via a similarity solution, where the streamwise velocity component is proportional to distance along the stretching axis, and all other variables depend solely on the wall-normal coordinate. Additionally, by assuming that disturbances are amplified far from the inlet, parallelisation arguments—similar to those used in the rotating disk—can be applied to the flow, thereby permitting the use of an ordinary, rather than partial, differential eigenvalue problem to model the growth of disturbances. This approach was originally applied to Crane's flow by Griffiths *et al.* [39], where excellent agreement was found between numerical and asymptotic results in the isothermal case. Encouraged by these results, our goal was to extend this simple model, focussing on flows which mimic many of the characteristics of Crane's flow to allow us to determine the important physical mechanisms driving the instability of these classes of flows.

In Chapters 2 and 3, we introduced two new formulations. The first of these involved the inclusion of temperature effects. This entailed maintaining both the flat geometry and linear stretching rate of Crane's flow while imposing a temperature-dependent viscosity. This approach has been commonly employed in other boundary layers, such as the rotating disk [78] and Blasius boundary layer [77]. Temperature effects are clearly relevant to a variety of extrusion flows. In polymer extrusion, for instance, the polymer undergoes thermally induced phase transitions, behaving as a liquid while being drawn before solidifying at the outlet. Although the model we proposed initially neglected streamwise variations in the temperature of the sheet, by assuming the sheet was fixed at a constant temperature higher than that of the free-stream, it allowed us

to make novel quantitative predictions regarding the behaviour of the basic flow.

For mathematical convenience, we chose to impose an inverse relationship between temperature and viscosity for the majority of our calculations. This relationship is given in dimensionless form as $\mu = (1 + mT)^{-1}$, where m is a parameter determining the sensitivity of the viscosity to changes in temperature. The momentum and energy equations are uncoupled when $m = 0$, in this case we recover the exact solutions of Crane. In the coupled case, our extended model no longer yields an exact analytical solution and the resulting boundary layer problem had to be solved numerically using a shooting method. However, we were able to show that approximate, near wall solutions could be attained under the assumption of weak temperature dependence, *i.e.* $|m| \ll 1$.

The inverse viscosity relationship has the advantage of being easily interpreted, with negative values of the sensitivity parameter indicating gaseous-type flows and positive values corresponding to liquids. From an industrial perspective, we are primarily interested in gaseous-type flows; however, results were presented for both cases. For all calculations in this thesis, we fixed $Pr = 0.72$, as this value is used to model the Prandtl number of air ([77],[78]). While this choice was appropriate for $m < 0$, the parameter regime of interest, it should be noted that for $m > 0$, this value would likely vary with temperature. With these caveats in mind, our main result was that wall shear stress increases with increasing values of the sensitivity parameter, which has important implications for the corresponding linear stability analysis.

For the purposes of this thesis, we were primarily interested in the constant wall temperature case. However, we also examined the role of viscous dissipation. Dissipative effects are commonly associated with compressible flow regimes at speeds far greater than those observed in extrusion flows. However, by including viscous dissipation in our model, we showed that we can no longer assume that temperature is invariant in the drawing direction, as the kinetic energy produced by the stretching sheet leads to increases in temperature near the sheet. While this regime was explored due to the interesting changes in the characteristics of the boundary layer equations, the Keller-Box scheme developed to iteratively integrate the nonlinear boundary layer equations could be easily adapted to account for streamwise variations in sheet temperature observed in industrial extrusion processes.

Perhaps the most pertinent critique of Crane's model is the omission of the sheet's deformation. Any incompressible material being accelerated by stretching must deform to conserve mass. Although Crane's model could be viewed as a small deformation approximation of such processes, it is clear, when compared to models of stretching sheets ([82],[50]), that deformation should be accounted for. In Chapter 2, this was achieved by performing a coordinate system transformation to flatten curvature of the sheet, before applying standard boundary layer arguments to derive

the leading order equations. Our formulation closely followed that of Rees and Pop [92], for the flow induced by a wavy moving surface. However our formulation is generalised in that it can be readily tailored to model a wide variety boundary layer flows. This was illustrated in Chapter 3 by applying our formulation to surface thickening flows, such as those observed in textile compaction. In Hanevy *et al.* [45], we also show how the formulation may be used to model surface roughness.

However, here we are primarily interested in boundary layers induced by stretching sheets. By imposing an exponentially thinning sheet profile, similar to those predicted empirically by Trouton [111] and analytically in numerous studies for a variety of flow geometries ([82],[50],[75]), we showed that analytical boundary layer solutions can be derived. These solutions were validated by comparison to numerical solutions of the full Navier-Stokes equations using the finite element software FEniCS [68] and were shown to be in excellent agreement. Our results demonstrate that failing to account for the sheet's deformation leads to quantitatively poor predictions for the basic flow velocities, particularly near the inlet, where the role of deformation is most pronounced. To derive these solutions, our analysis relied on being able to analytically integrate $\sigma = \sqrt{1 + (s'_\xi)^2}$, where s represents the shape of the sheet. This integral cannot be evaluated analytically for general sheet profiles, and more complex sheet shapes could be explored by implementing a suitable numerical integration scheme. In our formulation, there were several “free” integration constants, which we selected to make our basic flow closely mimic Crane's flow profiles. This was done solely for comparative purposes; in practice, these constants would be determined through experimental comparisons. In fact, the Trouton model predicts an exponentially accelerating sheet profile, which could be readily modelled by our formulation.

Concerning flow stability, several approaches were taken. The first involved extending the modal analysis of the isothermal problem performed by Griffiths *et al.* [39] to account for temperature dependence. This consisted of a complimentary numerical and asymptotic analysis in Chapters 4 and 5 respectively. In the numerical analysis we showed that there exists a narrow range of positive values of the sensitivity for which the flow is stabilised. This is consistent with the results for the Blasius boundary layer presented by Miller *et al.* [77]. In our integral energy analysis we demonstrated that the destabilisation observed for $m > 0.36$ is due to a relative increase in the energy production from the Reynolds stress term, although it should be emphasised that we have not accounted for variations in Prandtl number which would be expected in this regime. The main finding of the numerical analysis is that negative values of the sensitivity parameter are strongly destabilising. We found that the critical Reynolds number was approximately halved when compared to the isothermal case for $m = -0.4$. This is of practical interest, as this is the parameter regime that would be observed for such flows in industry and suggests that temperature effects should be considered. Given that we defined our critical Reynolds number in terms of the dimensionless distance from the inlet, this means that if modal instabilities are to

be observed, they will occur further upstream in the presence of a large temperature gradient.

For the remainder of the numerical analysis, we evaluated the role of the additional basic flow terms that arise due to the action of the stretching sheet. This was achieved by solving both the Orr-Sommerfeld equations and a global flow solver in Nektar++ under the assumptions of the normal mode analysis. Higher-order basic flow terms are typically neglected in similar numerical studies of the Blasius boundary layer but are required to improve agreement with experiments for the rotating disk. However, due to the large critical Reynolds number for Crane's flow, these terms were not found to significantly affect the quantitative results of our modal analysis. Nevertheless, it is interesting to note that these terms are stabilising, as in the case of the rotating disk.

The large critical Reynolds numbers reported in the numerical analysis had important implications for the asymptotic analysis in Chapter 5. Here we adopted the triple deck, lower branch analysis as outlined by Smith [100] for the Blasius boundary layer. While Smith [100] included five terms in his expansion to incorporate non-parallel effects, we found excellent agreement between our asymptotic and numerical solutions using only the leading order term in the expansion. This is a consequence of the large Reynolds numbers involved, as the asymptotic expansions exploit the high Reynolds number. Although unusually large compared to the Blasius or rotating disk boundary layers, a critical Reynolds number of a similar magnitude is reported by Wall and Wilson [116] for the ASBL, which also exhibits an exponentially decaying streamwise velocity profile. As in the isothermal analysis, the leading order asymptotic solutions are governed by the wall shear stress, which is modified to account for the non-constant viscosity. An advantage of our asymptotic results is that they are easily adaptable; for example, our inverse temperature-viscosity relationship could easily be replaced with a more accurate, empirically derived viscosity distribution. Provided the wall shear stress could be accurately calculated, our asymptotic dispersion relation could be modified to determine the flow stability.

As we have shown, the large critical Reynolds numbers from the numerical analysis are advantageous for asymptotically analysing flow stability. However, it raises the question of whether laminar flow would be observed in practice at such high Reynolds numbers. To address this question, we explored alternative energy growth mechanisms in the form of transient growth in Chapter 6. Here we solved the temporal problem by adopting the direct-adjoint power iteration scheme introduced by Corbett and Bottaro [22]. We demonstrated that significant energy amplification can occur at Reynolds numbers which are more than one hundred times smaller than the critical Reynolds number from the modal analysis. While this does not allow us to specify exactly where transition will occur, it does suggest that the modal analysis alone is inadequate for describing this process.

In contrast to the modal analysis, numerical non-modal investigations indicate that retaining the additional stretching terms fundamentally changes the structure of the optimisation problem, with the initial conditions obtained through power iteration being independent of the time domain over which they are integrated when stretching terms are included. The reason for this phenomenon remains unclear and requires further investigation. While this problem is mathematically interesting, given that the underlying model omits much of the essential physics for such flows, it is unlikely to have major consequences for extrusion flows in practice. Our analysis may be thought of as an initial step to identify alternative routes to transition. However, we can conclude that the non-modal energy mechanism is likely a far more important factor driving the instability of extrusion-induced flows compared to the convective instabilities previously considered.

As demonstrated, we have presented several additional models for the flows induced by the motion of stretching sheets. This has enabled us to quantify how the omission of these additional physical effects has resulted in poor predictions of both basic flow profiles and their stability. The key takeaways from our analysis are as follows: firstly, neglecting the deformation of the sheet leads to inaccurate predictions for the basic flow profiles in the vicinity of the inlet. Secondly, large temperature gradients have significant implications for the linear stability results, halving the critical Reynolds number even for moderate values of the sensitivity parameter. Finally, non-modal mechanisms are likely the primary factors governing the stability of these simplified models of such flows.

As with any thesis, there are several additional ways in which the models presented could be adapted and improved. In the following Chapter, we briefly discuss some alternative approaches that were considered, highlighting where challenges arose and suggesting future lines of investigation.

Chapter 8

Future Works

In this Chapter, we discuss alternative approaches used to analyse flows induced by stretching sheets. In particular, we highlight why certain types of instabilities have not been reported in the thesis thus far, and examine the challenges involved in implementing various non-local stability schemes. Additionally, we briefly review several studies that have attempted to couple the dynamics of the sheet with the induced boundary layer, emphasising the issues and challenges associated with sharp viscosity gradients, transitioning from Stokes flow in the sheet ($R \ll 1$) to large Reynolds numbers in the boundary layer.

8.1 Alternative Flow Stability Approaches

Thus far, we have invoked parallel flow approximations to analyse the stability of the flow induced by stretching sheets, both in the modal numerical analysis in Chapters 4, and the non-modal analysis of Chapter 6. While this gives us an indication of the important physical factors for the disturbances considered, there are several additional physical effects which warrant attention for a comprehensive understanding of the full system. Initially, this was our intention after deriving the basic flow solutions for the deforming sheet in Chapter 3. In the remainder of this Section we will outline how we attempted to incorporate the effects of curvature by considering non-local stability schemes as well as exploring different types of “local” instabilities, beyond the Tollmien-Schlichting and non-modal instabilities previously considered.

8.1.1 BiGlobal

The vast majority of studies in hydrodynamic stability theory have focused on parallel shear flows, either by direct analysis of inherently parallel flows such as Poiseuille or Couette flows, or by employing parallelisation arguments for boundary layers. This involves leveraging the slow streamwise variation of the basic flow, as seen in the rotating disk, Blasius boundary layer, and, in this thesis, the stretching sheet. This approach is favoured as it reduces a partial differential eigenvalue problem to an ordinary differential eigenvalue problem, where modes only need to be resolved in one spatial dimension. In using this approach it is explicitly assumed that

1. The basic flow depends on only one spatial dimension.
2. The perturbations are periodic in all other spatial dimensions and in time.

These assumptions become invalid when the deformation of the sheet is taken into account. Nevertheless, these stability concepts are easily generalised to account for multiple inhomogeneous spatial directions.

The term ‘‘BiGlobal’’ was first introduced in the review of Theofilis [104], to differentiate between absolute instabilities (referred to as global instabilities in the review of Huerre and Monkewitz [52] and discussed in the context of stretching sheets in Section 8.1.3 below), and the instabilities of basic flows which vary in two spatial dimensions. BiGlobal stability analysis assumes homogeneity in the third spatial dimension and assumes perturbations take the following form

$$\tilde{\mathbf{q}}(\mathbf{x}, t) = \hat{\mathbf{q}}(x, y) \exp\{i(\beta z - \omega t)\}.$$

Substituting these perturbations into the linearised Navier-Stokes equations results in a two-dimensional eigenvalue problem. Computations are typically performed in the temporal framework, with β and R prescribed. However, spatial simulations can be conducted, though at a significantly higher computational cost, by constructing the corresponding companion matrix [85]. This matrix factorisation converts the quadratic eigenvalue problem into a linear eigenvalue problem, following the same scheme used by Matlab’s `polyeig` function, which we employed in Chapter 4. The above formulation is easily extended for flows which vary in three spatial dimensions, commonly referred to as a TriGlobal stability analysis.

Progress in analysing such instabilities is inherently tied to the large increases in computational resources over recent years. This is due to the sharp increase in storage requirements with the number of discretised dimensions. Generalising the one-dimensional spectral schemes of Chapter 4, with a modest $N = 64$ collocation points, Theofilis [104] provides the following storage estimates for the respective discretised matrices: approximately 17.6TB for three-dimensional simulations, 4.3GB for two-dimensional simulations, and 1.0MB for one-dimensional simulations.

This considerable demand for storage has driven the implementation of alternative approaches, which construct sparse discretisations of the linearised Navier-Stokes equations using spectral/finite elements ([56],[81],[15]), and finite volume schemes ([30],[3]). These methods have the added advantage of being able to easily handle non-Cartesian geometries. The schemes used to solve the resulting eigenvalue problem vary depending on several factors, each presenting its own trade-offs and advantages. While it is beyond the scope of this thesis to explore these schemes in depth, the reader is referred to Theofilis [105] for a comprehensive review. Instead, we will focus on the specific challenges associated with the stretching sheet problem.

Crane’s flow, like many boundary layer flows, faces ambiguity when determining appropriate boundary conditions at the outflow. In our “global” calculations using Nektar++ in Chapter 4, we addressed this issue by parallelising the flow and enforcing periodic perturbations, consistent with the assumptions of our normal mode analysis. While this approach is useful for validation, it does not provide a comprehensive description of the perturbation dynamics. Other strategies for imposing outflow boundary conditions face similar limitations. For example, Fasel *et al.* [31] used a Robin outflow condition, derived via Gaster’s transformation [35], obtained from consideration of the local results. However, this effectively forces BiGlobal results to align with local results by imposing artificial, non-physical boundary conditions.

Alternative outflow boundary conditions have been explored for other flow regimes, such as no-stress conditions obtained in deriving the weak form for finite element simulations [56], and linearly extrapolated boundary conditions [104]. These approaches typically lead to the formation of spurious modes arising in the vicinity of the outlet which need to be discarded when post processing results [105]. However, due to the action of the stretching sheet, it is unclear whether such an approach is justifiable in this context. In the next Section we discuss the parabolised stability equations (PSE), which eliminate the need to specify outflow conditions due to the parabolic nature of the approximations made.

8.1.2 PSE

The parabolised stability equations (PSE) were developed to model convective instabilities by simplifying the elliptic linearised Navier-Stokes equations. The idea of using parabolic equations to model the evolution of boundary layer disturbances originated by Floryan and Saric [33] and was further explored by Hall [43] in their studies of Görtler vortices. Itoh [55] was the first to adapt these ideas to follow the spatial development of Tollmien-Schlichting (T-S) waves. Over time, the method has been extended by various authors to include compressible, non-linear, and curvature effects, which are particularly relevant for stretching sheet flows ([48],[6],[49]).

The appeal of the PSE lies in its computational efficiency compared to global schemes or direct numerical simulation (DNS). This is achieved by decomposing perturbations into a slowly varying amplitude function and an oscillatory part, expressed as:

$$\tilde{\mathbf{q}}(\mathbf{x}, t) = \hat{\mathbf{q}}(x, y) \exp \left\{ i \left(\int_{x_0}^x \alpha(\bar{x}) d\bar{x} + \beta z - \omega t \right) \right\}.$$

It is further assumed that the basic flow varies slowly in the streamwise direction, which implies that the perturbation amplitude functions and the streamwise wavenumber α are also slowly varying functions of x . This leads to the introduction of the following scales

$$V, \frac{\partial}{\partial x} \sim \mathcal{O}(R^{-1}), \quad U, \frac{\partial}{\partial y} \sim \mathcal{O}(1).$$

When substituted into the linearised Navier-Stokes equations, terms of up to $\mathcal{O}(R^{-1})$ are retained, resulting in a system of “almost” parabolic stability equations. However, residual ellipticity introduces step size restrictions, where oscillations may develop in the numerical solution if the step size is too small. As a consequence, stabilisation schemes have been proposed. For example, Li and Malik [66] suggest omitting the x -derivative of the pressure perturbation to relax step size constraints, whereas Andersson *et al.* [4] propose the inclusion of an additional stabilisation terms. However, as Towne *et al.* [108] demonstrate, the PSE can only capture disturbances of a single wavelength at each frequency and that the imposition of stabilisation techniques can lead to the improper evolution of disturbances.

The PSE approach treats a boundary value problem as an initial value problem, where the streamwise marching scheme is initialised by solutions attained from local analysis. The quality of results for the PSE is therefore highly dependent on the quality and applicability of the conditions used to initialise the scheme. Despite this limitation, the method has demonstrated excellent performance in simulating boundary layers, particularly within the Falkner-Skan-Cooke family, which includes the Blasius boundary layer. Evidence of this can be found in the comparison between PSE results and direct numerical simulation (DNS) in Bertolotti *et al.* [6] where the two approaches show excellent agreement. Although it is difficult to know in advance whether this agreement will hold for a given flow regime, the significant reduction in computational cost compared to other non-local schemes makes PSE an attractive option when applicable.

Preliminary numerical experimentation indicates that non-parallel effects are destabilising for the isothermal flat stretching sheet. Further details about our implementation may be found in Appendix D. A comparison between the local and PSE solutions are shown in Figure 8.1, where the streamwise marching scheme has been initialised from the critical values reported by Griffiths *et al.* [39] and in table 4.1. The results show significant amplification occurs when the development of the boundary layer is considered. This is in contrast to the studies of

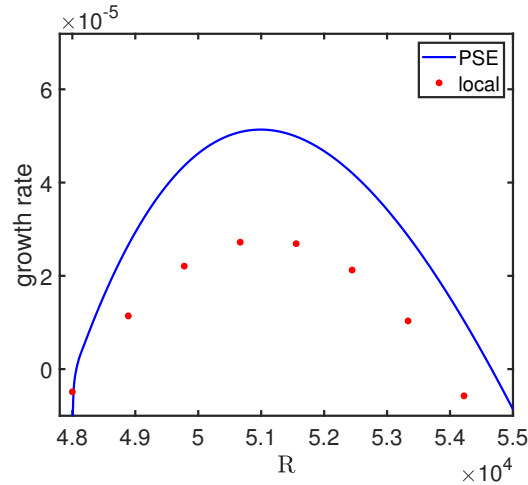


Figure 8.1: Comparison of local and PSE results for the isothermal stretching sheet. The scheme is initialised using the eigenfunctions calculated from the spatial modal analysis for $R = 48499.1$, $\omega = 0.1364$.

Wang [117] and Malik *et al.* [73] for the rotating disk flow. However, it is well known that the rotating disk boundary layer is susceptible to absolute instabilities [67], the presence of which may contaminate the PSE results for the disk [108].

Although we have not yet conducted a full parametric analysis of Crane’s flow using PSE, such an investigation would allow for a detailed quantification of the effects of curvature on convective instabilities in extrusion flows. This approach has been widely applied in studies of instabilities over swept wings, where the irregular wing geometry is accounted for by expressing the Navier-Stokes equations in curvilinear coordinates [117].

8.1.3 Absolute Instability

In prior stability analyses throughout this thesis, we focused on either temporal or spatial instabilities, referring to disturbances that grow either in time or space. In contrast, absolute instabilities are disturbances that grow both in space and time, typically defined by the impulse response or Green’s function. The rotating disk boundary layer, for instance, is known to be susceptible to absolute instabilities [67]. In the previous Section, we proposed the use of the PSE to evaluate the impact of curvature and non-parallel effects for Crane’s flow. Given the qualitative similarities between Crane’s flow and the rotating disk—and the inability for the PSE to capture absolute instabilities—in this Section, we present our reasoning for why we believe that Crane’s flow is not absolutely unstable. This supports the continued use of PSE in future investigations. To build this argument, we must first introduce several concepts and definitions

that are specific to absolute instabilities.

We begin by taking a dispersion relation

$$\mathcal{D}(\alpha, \omega; \mathbf{R}) = 0,$$

where α , ω and \mathbf{R} , as before, represent the streamwise wavenumber, frequency and Reynolds numbers respectively. To analyse the system's stability, we introduce the associated differential operator that governs the fluctuations $\Psi(x, t)$ in real space and time. This is expressed as

$$\mathcal{D} \left[-i \frac{\partial}{\partial x}, i \frac{\partial}{\partial t}; \mathbf{R} \right] \Psi(x, t) = 0.$$

To deduce the flow's stability characteristics we are interested in the system's response to impulsive forcing. This is given by the Green's function $G(x, t)$ as follows

$$\mathcal{D} \left[-i \frac{\partial}{\partial x}, i \frac{\partial}{\partial t}; \mathbf{R} \right] G(x, t) = \delta(x)\delta(t), \quad (8.1)$$

where δ denotes the Dirac delta function and the basic flow is perturbed at $x = t = 0$. Flow stability can then be defined in terms of the Green's function as follows [97]: The basic flow is linearly stable if

$$\lim_{t \rightarrow \infty} G(x, t) = 0 \quad \text{along all rays} \quad \frac{x}{t} = \text{constant}.$$

The basic flow is linearly unstable if

$$\lim_{t \rightarrow \infty} G(x, t) \rightarrow \infty \quad \text{along at least one ray} \quad \frac{x}{t} = \text{constant}.$$

Unstable basic states are then further classified as being either convectively or absolutely. Convective instability implies that

$$\lim_{t \rightarrow \infty} G(x, t) = 0 \quad \text{along the ray} \quad \frac{x}{t} = 0,$$

whereas absolute instability requires

$$\lim_{t \rightarrow \infty} G(x, t) \rightarrow \infty \quad \text{along the ray} \quad \frac{x}{t} = 0.$$

A schematic representation of these definitions, showing the distinction between convective and absolute instabilities, is provided in Figure 8.2.

With these definitions noted, we will demonstrate how the method outlined in Briggs *et al.* [12], may be used to assess whether a flow is absolutely unstable. In the process we will reproduce results from Lingwood [67] for the rotating disk. Here the basic flow solutions are the well known

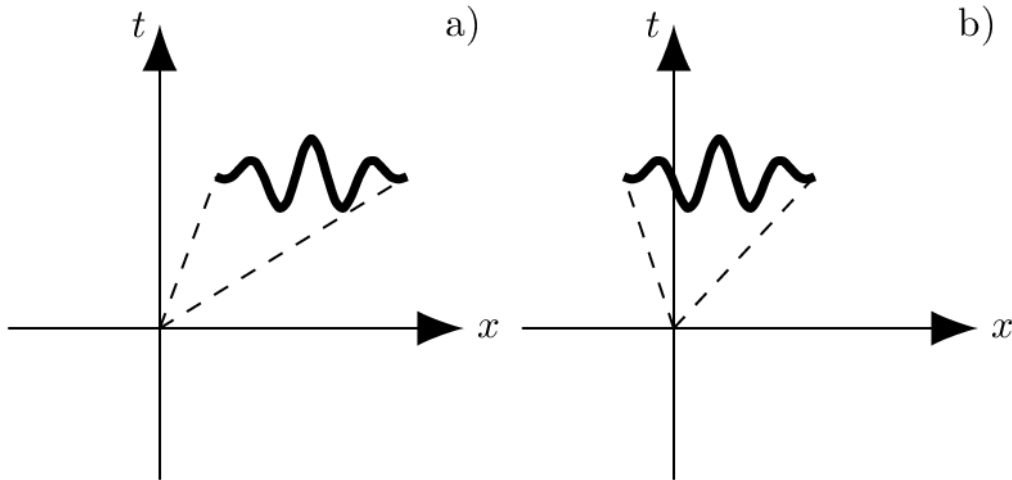


Figure 8.2: Schematic depicting the impulse response of a) convective and b) absolute instabilities in an x - t -plane diagram.

Von Kármán [115] solutions obtained for the steady, axisymmetric Navier-Stokes equations in a frame of reference rotating with the disk. The associated linear stability equations are derived by Malik *et al.* [73] (Equations (2.11)–(2.14)) and include higher order basic flow terms associated with streamline curvature and Coriolis forces.

Our definition of the Green’s function (8.1), may be expressed as a double Fourier integral

$$G(x, t) = \frac{1}{4\pi^2} \int_F \int_L \frac{\exp[i(\alpha x - \omega t)]}{\mathcal{D}(\alpha, \omega)} d\alpha d\omega,$$

where L and F denote inversion contours in the ω and α planes respectively. Given the definitions of convective and absolute instabilities, we are interested in calculating the large time behaviour of the Fourier-Laplace integral. Briggs’ method involves “splitting” this integral, by first considering the wave number integral

$$\tilde{G}(x, \omega) = \frac{1}{2\pi} \int_L \frac{\exp[i\alpha x]}{\mathcal{D}(\alpha, \omega)} d\alpha,$$

followed by the frequency inversion

$$G(x, t) = \frac{1}{2\pi} \int_F \tilde{G}(x, \omega) \exp[-i\omega t] d\omega.$$

In Figure 8.3, we begin by computing the numerical dispersion relation along the contours labelled ω_F and α_L at $\text{Re} = 515$, $\beta = 6$, for the rotating disk. The contour F is chosen to lie above all zeros of the dispersion relation, thereby satisfying the causality condition. This ensures that all disturbances are zero for $t < 0$. Evaluating the spatial eigenvalue problem along this

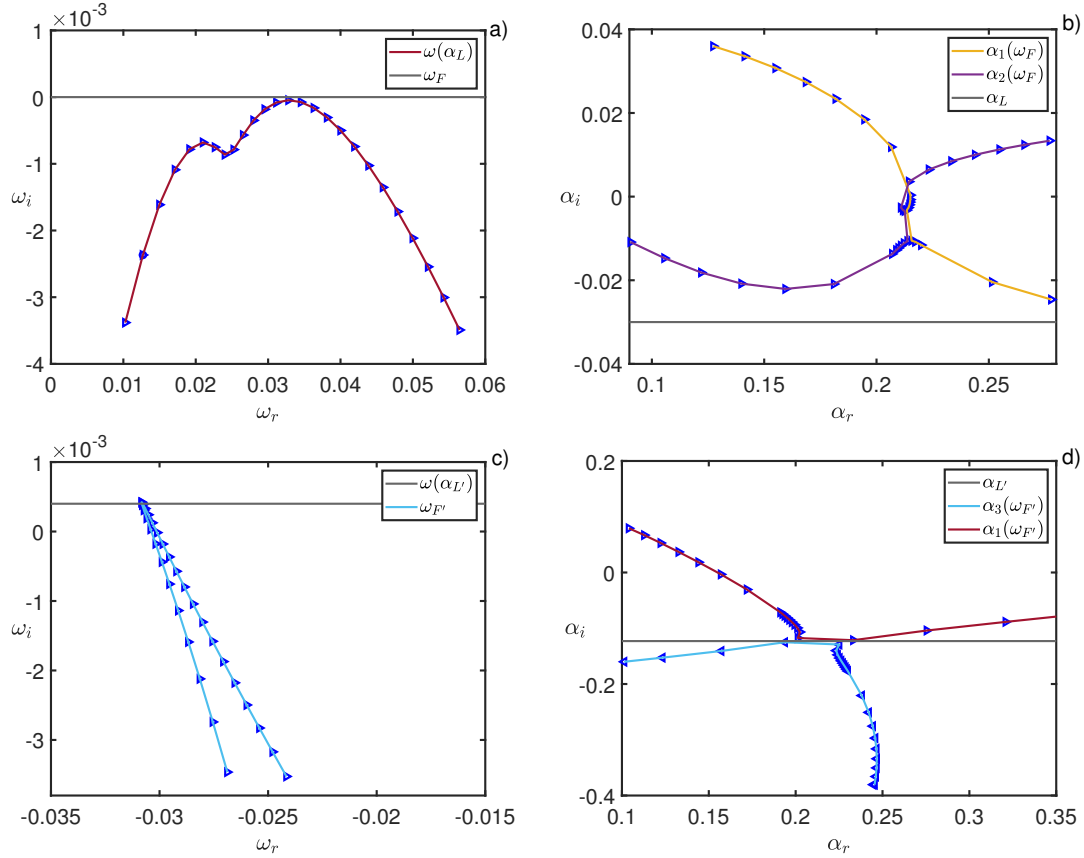


Figure 8.3: Diagram illustrating Briggs’ method for locating absolute instabilities in the rotating disk. In each plot the direction of the markers indicate the direction of the evolution branch for increases in the real part of the spanwise wavenumber and frequency.

contour leads to the two spatial branches in b). The subscripts 1 and 2, refer the mode type. The type 1 or cross-flow mode was originally discovered by Gregory *et al.* [38]. It is inviscid and is related to instabilities observed on swept wings. The type 2 mode is viscous and caused by curvature and Coriolis effects. They were originally found in the calculations Malik *et al.* [73], who retained higher-order basic flow terms when parallelising the linearised Navier-Stokes equations.

Solving the temporal problem along the contour α_L , leads to the curve $\omega(\alpha_L)$ in a). The essence of Briggs’ method is to deform the contour ω_F , so that the spatial contour α_L is pinched between the two spatial branches. This is shown in c) and d) for $Re = 530$, $\beta = 67$. Here the prime superscripts indicate that the contours have been deformed. Note also that in d) one of the spatial branches is now of type 3. These modes were initially found by Mack [71] and are spatially damped but propagate energy towards the centre of the disk.

Using Briggs’ criterion we can conclude that an absolute instability has been found since a pinch

point in the α plane has been found with branches which originate from different halves of the α plane ($\pm\alpha_i$) and we have a corresponding branch point in the ω plane, where $\omega_i > 0$ at the branch point. In contrast, for Crane’s flow, we have not found an equivalent to the type 3 mode in the disk, which opposes the direction of the mean flow. This indicates that absolute instabilities are not present and that the PSE is a viable approach for evaluating non-parallel effects in such flows. However, it is important to note that this may change if the momentum equations in the sheet and boundary layer are coupled, potentially giving rise to different modes of instability, such as interfacial instabilities, which could induce absolutely unstable behaviour.

8.1.4 Görtler Vortices

Görtler [37] was the first to examine steady instabilities for Blasius flow over a concave surface. His analysis involved transforming the cylindrical Navier-Stokes equations into a Cartesian-like system, by taking the large Reynolds number, small curvature limit. Assuming a two-dimensional basic flow, one arrives at a system of linearised boundary layer equations with an additional forcing term in terms of the Görtler number in the y momentum equation to account for the curved geometry. The Görtler number is assumed to be finite and is defined using

$$G^2 = \frac{R L}{\mathcal{R}},$$

where R is the Reynolds number, L is a characteristic length scale and \mathcal{R} is the radius of curvature. Following Görtler’s approach local results can be obtained, where it is found that disturbances in the form of streamwise-oriented, counter rotating vortices develop. This is similar to the non-modal instability mechanism studied in Chapter 6, the difference being that the most amplified Görtler vortices are steady. From the local results, neutral stability curves that separate the (β, G) plane—where β is the spanwise wavenumber—into regions of stability and instability can be calculated. However, Hall [43] has shown that a unique neutral curve cannot be found for all values of β and that the stability of the system can only be determined by solving a parabolic system of equations, similar to the PSE, which depend on the choice of initial condition. Nevertheless for $G > 7$, marching solutions are found to converge to local solutions [10].

The Görtler instability belongs to a family of related but distinct instabilities induced by centrifugal forces, all of which are governed by the Rayleigh circulation criterion [90]. The inviscid mechanism for these instabilities was originally given for flows in a circular geometry (r, θ, z) , with a parallel basic flow of the form $\mathbf{u} = (0, U(r), 0)$. In such a scenario, Rayleigh’s circulation

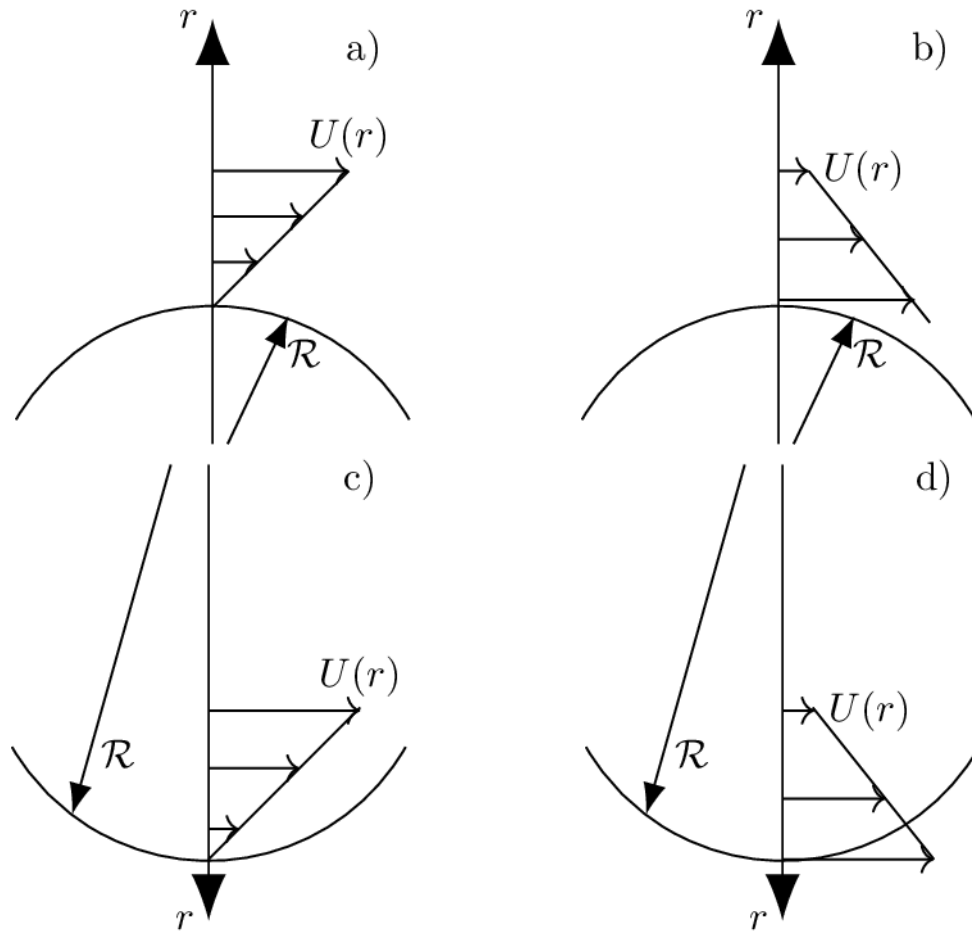


Figure 8.4: Schematic illustrating combinations of base flows and surface curvatures to induce centrifugal instabilities. According to the Rayleigh circulation criterion a) and d) are stable, whereas b) and c) are unstable. This Figure is reproduced from the review of Saric *et al.* [95].

criterion is a necessary and sufficient condition for the existence of instabilities, stating that if

$$\frac{d}{dr}(rU(r)) < 0,$$

anywhere in the flow, then the flow is unstable. A schematic of different flow configurations and surface curvatures is shown in Figure 8.4. While the diagrams depict linear velocity profiles, Floryan [32] has shown that the criterion also holds for boundary layers. With the inclusion of viscosity, Rayleigh's criterion becomes a necessary condition. Rewriting Crane's flow in an equivalent form we have $y = \mathcal{R} - r$, where \mathcal{R} , is the radius of curvature of the surface, such that

$$U = e^{r-\mathcal{R}} \implies \frac{d}{dr}(rU(r)) > 0,$$

and the criterion is not satisfied. This corresponds to Figure 8.4 d). It should be noted that

the same conclusions were reached by Davis and Pozrikidis [26] and Bhattacharyya and Gupta [7] for the flat stretching sheet. For the concave surface profiles expected in extrusion flows, the combination of basic flow and curvature is not conducive to inducing the Görtler instability. However, this observation suggests that the surface thickening profiles examined in Chapter 3 may be susceptible to these instabilities.

8.2 The Coupled Sheet Fluid Problem

To fully describe the dynamics of the flow induced by a stretching sheet, it is necessary to couple the dynamics of the sheet with those of the ambient fluid. Analytical approximations could be constructed by modifying the Trouton-based analysis of Howell [50], imposing a stress condition at the interface between the two fluid mediums to drive the boundary layer flow. Numerical simulations however, present significant challenges given the rapid changes in viscosities between the two phases. Nonetheless, interface tracking schemes such as volume of fluid or level-set methods, may be applicable in less severe regimes in order to validate analytical approximations. Both types of analysis in this case would require fixing the sheet to have finite length. While the boundary layer approximation has proven useful thus far, this approach would yield more industrially relevant results. In this Section, we highlight some approaches that have been taken in the literature thus far and suggest means by which they could be adapted and improved.

Of particular interest is the experimental and numerical results of Tammisola *et al.* [102], who examined the effects of surrounding air flow on the stability of a planar liquid sheet. In their experiments, a sheet of water falling under the influence of gravity was surrounded on either side by a channels of air flowing from pumps. Their aim was to prevent the break-up of the liquid sheet by co-blowing air at a similar velocity, reducing the shear stress at the interface. Experimental results were compared to a simple one-dimensional model. To derive this model, the basic states were assumed with a uniform profile imposed in the sheet, based on experimental results. In the boundary layer, two different profiles were employed. The first was the Sakiadas profile [94], which is a solution to the boundary layer equations for a constant, non-accelerating wall velocity. The second profile used was the analytical solution to Stokes' first problem, expressed in terms of the error function. To attain results, an Orr-Sommerfeld equation was constructed by perturbing about the assumed basic states. The equations were supplemented by five additional boundary conditions to capture the interface dynamics: velocity continuity (I & II), continuity of shear stress (III), normal stress jump (IV), and the evolution equation (V) at the interface.

While the co-blowing of air was shown to be stabilising, superior agreement between the experimental and theoretical results was found when the boundary layer was assumed to be fully driven by the sheet. This discrepancy arises due to the increased uncertainty regarding the

basic flows in the co-blowing scenario. However, given that the stagnant air case more closely corresponds to extrusion type flows, this indicates that this approach could be used to model the fully coupled dynamics, at least within some small deformation limit. It should be noted that the analysis was presented to extend theoretical results attained for the breakup of inviscid sheets, such as the analytical results of De Luca and Costa [27], who identified the presence of a convective-absolute instability boundary in their weakly non-parallel analysis of an inviscid two-dimensional sheet falling under gravity surrounded by a still gas. This is in contrast to the small Reynolds number approach used to model extrusion flows as in Howell [51] and O’Kiely *et al.* [84]. Whether the agreement between theory and experiment would persist in the viscous limit is unclear. However, given the relative ease at which such an approach could be implemented, it may prove beneficial to validate any numerical or experimental results in future. From [51], we can model the basic flow of a stretching viscous sheet and our analytical boundary layer approximations in Chapter 3 could easily be adapted for such an analysis.

The stability of the coupled sheet-fluid system was investigated numerically in the work of Della Pia *et al.* [28], utilising the volume of fluid method. This approach involves solving the continuity and Navier-Stokes equations over the entire domain, where material properties such as density and viscosity are discontinuous across the interface. The Navier-Stokes equations are supplemented with a volume fraction advection equation, which tracks the location of the interface as the solution evolves in time. Global stability properties of the flow regime were obtained by adding a small amplitude Gaussian bump to the steady solutions obtained for the sheet, where it was found that the system was destabilised for large density ratios between the sheet and ambient fluid.

This analysis is closer to the coupled problem found in extrusion flows since it reduces the sheet Reynolds number from $R = 3000$ in Tammisola *et al.* [102], to $R = 420$. However, the Reynolds number still remains far too large for conclusions regarding industrially relevant extrusion regimes to be drawn from this study. For example in the modelling of glass sheet drawing in O’Kiely [82], an upper bound of $R = 10^{-4}$ within the sheet is provided. While the Reynolds number of the sheet could be lowered further, such schemes are known to develop interfacial spurious currents when sharp variations in fluid properties are observed across the interface [54]. It is hoped that improvements in the development of these schemes, will make these extrusion regimes accessible to numerical simulations in the future.

To conclude, we briefly comment on the work of Al-Housseiny and Stone [2], who derived analytical basic flow solutions for the coupled sheet-fluid problem for both viscous and elastic sheets. Rather than using asymptotic arguments to determine the dominant balance of the system, a number of ad-hoc assumptions are made regarding the relative sizes of the respective terms in the two phases. To construct a matching condition at the interface, it is assumed that

the x -component of the normal stress in the sheet is a function of the streamwise sheet velocity, while the shear stress term in the sheet is a function of the streamwise boundary layer velocity, with no justification provided for why these approximations are made. These assumptions could be better substantiated by non-dimensionalising the problem to exploit small aspect ratios in the sheet [51].

While this analysis represents the first theoretical attempt to couple dynamics of the sheet and the boundary layer, the authors themselves acknowledge that “these self-similar solutions are valid under limiting conditions”. More general solutions may be obtained by modifying the Trouton approach ([51],[84]), which imposes a no-stress condition at the interface, to incorporate a thin shear layer near the interface which allows the Trouton solutions to match with deforming boundary-layer solutions equivalent to those presented in Chapter 3. Given the large viscosity ratios between the two phases, this inner boundary layer would likely be very thin. This property, which makes the problem numerically very challenging, should be amenable to an asymptotic analysis which could exploit this small length scale.

Bibliography

- [1] J. A. D. Ackroyd. A series method for the solution of laminar boundary layers on moving surfaces. *Z. fur Angew. Math. Phys.*, 29:729–741, 1978.
- [2] T. T. Al-Housseiny and H. A. Stone. On boundary-layer flows induced by the motion of stretching surfaces. *J. Fluid Mech.*, 706:597—606, 2012. doi: 10.1017/jfm.2012.292.
- [3] S. Albensoeder, H. Kuhlmann, and H. Rath. Three-dimensional centrifugal-flow instabilities in the lid-driven-cavity problem. *Phys. Fluids*, 13(1):121–135, 2001.
- [4] P. Andersson, D. Henningson, and A. Hanifi. On a stabilization procedure for the parabolic stability equations. *J. Eng. Math.*, 33:311–332, 1998.
- [5] P. Andersson, M. Berggren, and D. S. Henningson. Optimal disturbances and bypass transition in boundary layers. *Phys. Fluids*, 11(1):134–150, 1999.
- [6] F. P. Bertolotti, T. Herbert, and P. Spalart. Linear and nonlinear stability of the Blasius boundary layer. *J. Fluid Mech.*, 242:441–474, 1992.
- [7] S. Bhattacharyya and A. Gupta. On the stability of viscous flow over a stretching sheet. *Q. Appl. Math.*, 43(3):359–367, 1985.
- [8] S. Bickerton, M. J. Buntain, and A. A. Somashekar. The viscoelastic compression behavior of liquid composite molding preforms. *Compos. Part A Appl. Sci. Manuf.*, 34:431–444, 2003.
- [9] R. Bodonyi and F. T. Smith. The upper branch stability of the Blasius boundary layer, including non-parallel flow effects. *Proc. R. Soc. London, Ser. A*, 375(1760):65–92, 1981.
- [10] A. Bottaro and P. Luchini. Görtler vortices: are they amenable to local eigenvalue analysis? *Eur. J. Mech. (B/Fluids)*, 18(1):47–65, 1999.
- [11] J. Brady and A. Acrivos. Steady flow in a channel or tube with an accelerating surface velocity. An exact solution to the Navier—Stokes equations with reverse flow. *J. Fluid Mech.*, 112:127–150, 1981.

- [12] R. J. Briggs *et al.* *Electron-stream interaction with plasmas*, volume 187. MIT press Cambridge, MA, 1964.
- [13] J. Buckmaster, A. Nachman, and L. Ting. The buckling and stretching of a viscida. *J. Fluid Mech.*, 69(1):1–20, 1975.
- [14] K. M. Butler and B. F. Farrell. Three-dimensional optimal perturbations in viscous shear flow. *Phys. Fluids A*, 4(8):1637–1650, 1992.
- [15] C. D. Cantwell, D. Moxey, A. Comerford, A. Bolis, G. Rocco, G. Mengaldo, D. De Grazia, S. Yakovlev, J.-E. Lombard, D. Ekelschot, *et al.* Nektar++: An open-source spectral/hp element framework. *Comput. Phys. Commun.*, 192:205–219, 2015.
- [16] P. W. Carpenter and P. J. Morris. The effect of anisotropic wall compliance on boundary-layer stability and transition. *J. Fluid Mech.*, 218:171–223, 1990.
- [17] P. W. Carpenter and L. J. Porter. Effects of passive porous walls on boundary-layer instability. *AIAA J.*, 39(4):597–604, 2001.
- [18] T. Cebeci and P. Bradshaw. *Physical and computational aspects of convective heat transfer*. Springer Science & Business Media, 2012.
- [19] T. Cebeci and K. Stewartson. On stability and transition in three-dimensional flows. *AIAA J.*, 18(4):398–405, 1980.
- [20] A. Chakrabarti and A. Gupta. Hydromagnetic flow and heat transfer over a stretching sheet. *Q. Appl. Math.*, 37(1):73–78, 1979.
- [21] A. J. Cooper and P. W. Carpenter. The stability of rotating-disc boundary-layer flow over a compliant wall. Part 1. Type I and II instabilities. *J. Fluid Mech.*, 350:231–259, 1997.
- [22] P. Corbett and A. Bottaro. Optimal perturbations for boundary layers subject to stream-wise pressure gradient. *Phys. Fluids*, 12(1):120–130, 2000.
- [23] L. J. Crane. Flow past a stretching plate. *Z. fur Angew. Math. Phys.*, 21(4):645–647, 1970.
- [24] L. J. Crane. Boundary layer flow due to a stretching cylinder. *Z. fur Angew. Math. Phys.*, 26(5):619–622, 1975.
- [25] S. J. Davies and C. M. White. An experimental study of the flow of water in pipes of rectangular section. *Proc. R. Soc. London, Ser. A*, 119(781):92–107, 1928.
- [26] J. M. Davis and C. Pozrikidis. Linear stability of viscous flow induced by surface stretching. *Arch. Appl. Mech.*, 84:985–998, 2014.

- [27] L. De Luca and M. Costa. Instability of a spatially developing liquid sheet. *J. Fluid Mech.*, 331:127–144, 1997.
- [28] A. Della Pia, M. Chiatto, and L. de Luca. Global eigenmodes of thin liquid sheets by means of volume-of-fluid simulations. *Phys. Fluids*, 32(8), 2020.
- [29] L. J. Dempsey and A. G. Walton. Vortex/Tollmien–Schlichting wave interaction states in the asymptotic suction boundary layer. *Q. J. Mech. Appl. Math.*, 70(3):187–213, 2017.
- [30] H. A. Dijkstra. On the structure of cellular solutions in Rayleigh–Bénard–Marangoni flows in small-aspect-ratio containers. *J. Fluid Mech.*, 243:73–102, 1992.
- [31] H. Fasel, U. Rist, and U. Konzelmann. Numerical investigation of the three-dimensional development in boundary-layer transition. *AIAA J.*, 28(1):29–37, 1990.
- [32] J. Floryan. Görtler instability of boundary layers over concave and convex walls. *Phys. Fluids*, 29(8):2380–2387, 1986.
- [33] J. M. Floryan and W. S. Saric. Stability of Gortler vortices in boundary layers. *AIAA J.*, 20(3):316–324, 1982.
- [34] J. H. Fransson and P. Corbett. Optimal linear growth in the asymptotic suction boundary layer. *Eur. J. Mech. B/Fluids*, 22(3):259–270, 2003.
- [35] M. Gaster. A note on the relation between temporally-increasing and spatially-increasing disturbances in hydrodynamic stability. *J. Fluid Mech.*, 14(2):222–224, 1962.
- [36] D. Geropp. Der turbulente Wärmeübergang am rotierenden Zylinder. *Ing. Arch.*, 38: 195–203, 1969.
- [37] H. Görtler. Über eine dreidimensionale Instabilität laminarer Grenzschichten an konkaven Wänden. *Ges. D. Wiss. Göttingen, Nachr. ad, Math.*, 1940.
- [38] N. Gregory, J. T. Stuart, and W. Walker. On the stability of three-dimensional boundary layers with application to the flow due to a rotating disk. *Philos. Trans. R. Soc. London A.*, 248(943):155–199, 1955.
- [39] P. Griffiths, S. Stephen, and M. Khan. Stability of the flow due to a linear stretching sheet. *Phys. Fluids*, 33(8):084106, 2021.
- [40] C. E. Grosch and H. Salwen. The continuous spectrum of the Orr-Sommerfeld equation. Part 1. The spectrum and the eigenfunctions. *J. Fluid Mech.*, 87(1):33–54, 1978.
- [41] L. H. Gustavsson. Energy growth of three-dimensional disturbances in plane Poiseuille flow. *J. Fluid Mech.*, 224:241–260, 1991.

- [42] M. P. Hack and T. A. Zaki. Modal and non-modal stability of boundary layers forced by spanwise wall oscillations. *Journal of Fluid Mechanics*, 778:389–427, 2015.
- [43] P. Hall. The linear development of Görtler vortices in growing boundary layers. *J. Fluid Mech.*, 130:41–58, 1983.
- [44] N. Hanevy and D. O’Kiely. Asymptotic Analysis for Fiber Drawing Processes. *SIAM J. Appl. Math.*, 83(2):725–747, 2023.
- [45] N. Hanevy, J. Ferguson, P. M. Trevelyan, and P. T. Griffiths. Boundary-layer flows over deforming surfaces. *Phys. Rev. Fluids*, 9(5):054101, 2024.
- [46] N. Hanevy, S. Stephen, M. Philip, and P. Griffiths. Stability of the flow due to a heated stretching sheet (submitted). *Phys. Fluids*, 2024.
- [47] J. Healey. On the neutral curve of the flat-plate boundary layer: comparison between experiment, Orr–Sommerfeld theory and asymptotic theory. *J. Fluid Mech.*, 288:59–73, 1995.
- [48] S. Hein, F. Bertolotti, M. Simen, A. Hanifi, and D. Henningson. Linear nonlocal instability analysis—the linear NOLOT code. 1995.
- [49] T. Herbert. Parabolized stability equations. *Annu. Rev. Fluid Mech.*, 29(1):245–283, 1997.
- [50] P. Howell. Models for thin viscous sheets. *Eur. J. Appl. Math.*, 7(4):321–343, 1996.
- [51] P. D. Howell. *Extensional thin layer flows*. PhD thesis, University of Oxford, 1994.
- [52] P. Huerre and P. A. Monkewitz. Local and global instabilities in spatially developing flows. *Annu. Rev. Fluid Mech.*, 22(1):473–537, 1990.
- [53] L. S. Hultgren. Higher eigenmodes in the Blasius boundary-layer stability problem. *Phys. Fluids*, 30(10):2947–2951, 1987.
- [54] V. Inguva, A. Schulz, and E. Y. Kenig. On methods to reduce spurious currents within VOF solver frameworks. Part 1: a review of the static bubble/droplet. *Chem. Prod. Process Model.*, 17(2):121–135, 2022.
- [55] N. Itoh. Secondary instability of laminar flows. *Proc. R. Soc. London, Ser. A*, 375(1763):565–578, 1981.
- [56] C. Jackson. A finite-element study of the onset of vortex shedding in flow past variously shaped bodies. *J. Fluid Mech.*, 182:23–45, 1987.

- [57] M. Juniper, A. Hanifi, and V. Theofilis. Modal Stability Theory Lecture notes from the FLOW-NORDITA Summer School on Advanced Instability Methods for Complex Flows, Stockholm, Sweden, 2013. *Applied Mechanics Reviews*, 66, 02 2014. doi: 10.1115/1.4026604.
- [58] T. Kanai and G. Campbell. *Film processing advances*. Carl Hanser Verlag GmbH Co KG, 2014.
- [59] T. Kato. *Perturbation theory for linear operators*, volume 132. Springer Science & Business Media, 2013.
- [60] H. B. Keller and T. Cebeci. Accurate numerical methods for boundary layer flows I. Two dimensional laminar flows. In *Proceedings of the International Conference on Numerical Methods in Fluid Dynamics, Lecture Notes in Physics*, pages 92–100. Springer, 1971.
- [61] P. Kelly. A viscoelastic model for the compaction of fibrous materials. *J. Text. Inst.*, 102(8):689–699, 2011.
- [62] P. A. Kelly. A viscoelastic model for the compaction of fibrous materials. *J. Text. Inst.*, 102:689–699, 2011.
- [63] P. S. Klebanoff, K. Tidstrom, and L. Sargent. The three-dimensional nature of boundary-layer instability. *J. Fluid Mech.*, 12(1):1–34, 1962.
- [64] R. Kobayashi, Y. Kohama, and C. Takamadate. Spiral vortices in boundary layer transition regime on a rotating disk. *Acta Mech.*, 35(1):71–82, 1980.
- [65] M. Landahl. A note on an algebraic instability of inviscid parallel shear flows. *J. Fluid Mech.*, 98(2):243–251, 1980.
- [66] F. Li and M. R. Malik. Mathematical nature of parabolized stability equations. In *Laminar-Turbulent Transition: IUTAM Symposium, Sendai/Japan, September 5–9, 1994*, pages 205–212. Springer, 1995.
- [67] R. Lingwood. *Stability and transition of the boundary layer on a rotating disk*. PhD thesis, University of Cambridge, 1995.
- [68] A. Logg, K.-A. Mardal, and G. Wells. *Automated solution of differential equations by the finite element method: The FEniCS book*, volume 84. Springer Science & Business Media, 2012.
- [69] P. Luchini. Reynolds-number-independent instability of the boundary layer over a flat surface. *J. Fluid Mech.*, 327:101–115, 1996.

- [70] P. Luchini. Reynolds-number-independent instability of the boundary layer over a flat surface: optimal perturbations. *J. Fluid Mech.*, 404:289–309, 2000.
- [71] L. M. Mack. Linear stability theory and the problem of supersonic boundary-layer transition. *AIAA J.*, 13(3):278–289, 1975.
- [72] E. Magyari and B. Keller. Heat and mass transfer in the boundary layers on an exponentially stretching continuous surface. *J. Phys. D*, 32(5):577, 1999.
- [73] M. R. Malik, S. P. Wilkinson, and S. A. Orszag. Instability and transition in rotating disk flow. *AIAA J.*, 19(9):1131–1138, 1981.
- [74] C. Martelli, J. Canning, B. Gibson, and S. Huntington. Bend loss in structured optical fibres. *Opt. Express*, 15(26):17639–17644, 2007.
- [75] M. Matovich and J. Pearson. Spinning a molten threadline. Steady-state isothermal viscous flows. *Ind. Eng. Chem. Fundam.*, 8(3):512–520, 1969.
- [76] R. Messing and M. J. Kloker. Investigation of suction for laminar flow control of three-dimensional boundary layers. *J. Fluid Mech.*, 658:117–147, 2010.
- [77] R. Miller, S. J. Garrett, P. T. Griffiths, and Z. Hussain. Stability of the Blasius boundary layer over a heated plate in a temperature-dependent viscosity flow. *Phys. Rev. Fluids*, 3(11):113902, 2018.
- [78] R. Miller, P. Griffiths, Z. Hussain, and S. J. Garrett. On the stability of a heated rotating-disk boundary layer in a temperature-dependent viscosity fluid. *Phys. Fluids*, 32(2), 2020.
- [79] S. Morgan. *Stability of periodically modulated rotating disk boundary layers*. PhD thesis, Cardiff University, 2018.
- [80] M. R. Myers. A model for unsteady analysis of preform drawing. *AIChE J.*, 35(4):592–602, 1989.
- [81] R. Natarajan and A. Acrivos. The instability of the steady flow past spheres and disks. *J. Fluid Mech.*, 254:323–344, 1993.
- [82] D. O’Kiely. *Mathematical models for the glass sheet redraw process*. PhD thesis, University of Oxford, 2017.
- [83] S. A. Orszag. Accurate solution of the Orr–Sommerfeld stability equation. *J. Fluid Mech.*, 50(4):689–703, 1971.
- [84] D. O’Kiely, C. Breward, I. Griffiths, P. Howell, and U. Lange. Edge behaviour in the glass sheet redraw process. *J. of Fluid Mech.*, 785:248–269, 2015.

- [85] P. Paredes, V. Theofilis, D. Rodriguez, and J. Tendero. The PSE-3D instability analysis methodology for flows depending strongly on two and weakly on the third spatial dimension. In *AIAA Paper*, page 3752, 2011.
- [86] A. T. Patera. A spectral element method for fluid dynamics: laminar flow in a channel expansion. *J. Comput. Phys.*, 54(3):468–488, 1984.
- [87] J. Pearson and M. Matovich. Spinning a molten threadline. Stability. *Ind. Eng. Chem. Fundam.*, 8(4):605–609, 1969.
- [88] I. Pop and S. Nakamura. Laminar boundary layer flow of power-law fluids over wavy surfaces. *Acta Mech.*, 115:55–65, 1996.
- [89] K. R. Rajagopal, T. Na, and A. Gupta. Flow of a viscoelastic fluid over a stretching sheet. *Rheol. Acta*, 23:213–215, 1984.
- [90] L. Rayleigh. LIX. On convection currents in a horizontal layer of fluid, when the higher temperature is on the under side. *Phil. Mag.*, 32(192):529–546, 1916.
- [91] S. C. Reddy, P. J. Schmid, and D. S. Henningson. Pseudospectra of the Orr–Sommerfeld operator. *SIAM J. Appl. Math.*, 53(1):15–47, 1993.
- [92] D. A. S. Rees and I. Pop. Boundary layer flow and heat transfer on a continuous moving wavy surface. *Acta Mech.*, 112(1):149–158, 1995.
- [93] P. L. Sachdev, N. M. Bujurke, and N. P. Pai. Dirichlet Series Solution of Equations Arising in Boundary Layer Theory. *Math. Comput. Model.*, 32:971–980, 2000.
- [94] B. Sakiadis. Boundary-layer behavior on continuous solid surfaces: II. The boundary layer on a continuous flat surface. *AiChE J.*, 7(2):221–225, 1961.
- [95] W. S. Saric *et al.* Gortler vortices. *Annu. Rev. Fluid Mech.*, 26(1):379–409, 1994.
- [96] B. Scheid, S. Quiligotti, B. Tran, R. Gy, and H. A. Stone. On the (de) stabilization of draw resonance due to cooling. *J. Fluid Mech.*, 636:155–176, 2009.
- [97] P. J. Schmid and D. S. Henningson. *Stability and transition in shear flows*. 2001.
- [98] W. Schultz and S. Davis. One-dimensional liquid fibers. *J. Rheol.*, 26(4):331–345, 1982.
- [99] Y. T. Shah and J. Pearson. On the stability of nonisothermal fiber spinning. *Ind. Eng. Chem. Fundam.*, 11(2):145–149, 1972.
- [100] F. T. Smith. On the non-parallel flow stability of the Blasius boundary layer. *Proc. R. Soc. London, Ser. A* 3, 366(1724):91–109, 1979.

- [101] H. B. Squire. On the stability for three-dimensional disturbances of viscous fluid flow between parallel walls. *Proc. R. Soc. London, Ser. A* 3, 142(847):621–628, 1933.
- [102] O. Tammisola, A. Sasaki, F. Lundell, M. Matsubara, and L. D. Söderberg. Stabilizing effect of surrounding gas flow on a plane liquid sheet. *J. Fluid Mech.*, 672:5–32, 2011.
- [103] M. Taroni, C. Breward, L. Cummings, and I. Griffiths. Asymptotic solutions of glass temperature profiles during steady optical fibre drawing. *J. Engrg. Math.*, 80(1):1–20, 2013.
- [104] V. Theofilis. Advances in global linear instability analysis of nonparallel and three-dimensional flows. *Prog. Aerosp. Sci.*, 39(4):249–315, 2003.
- [105] V. Theofilis. Global linear instability. *Annu. Rev. Fluid Mech.*, 43(1):319–352, 2011.
- [106] A. J. Thompson, J. R. McFarlane, J. P.-H. Belnoue, and S. R. Hallett. Numerical modelling of compaction induced defects in thick 2D textile composites. *Mater. Des.*, 196:109088, 2020.
- [107] W. Tollmien. Über die entstehung der turbulenz. *Nachr. G es. Wiss. Göttingen, Math. Phys. Klasse 21.*, pages 18–21, 1930.
- [108] A. Towne, G. Rigas, and T. Colonius. A critical assessment of the parabolized stability equations. *Theor. Comput. Fluid Dyn.*, 33:359–382, 2019.
- [109] L. N. Trefethen. *Spectral methods in MATLAB*. SIAM, 2000.
- [110] L. N. Trefethen, A. E. Trefethen, S. C. Reddy, and T. A. Driscoll. Hydrodynamic stability without eigenvalues. *Science*, 261(5121):578–584, 1993.
- [111] F. T. Trouton. On the coefficient of viscous traction and its relation to that of viscosity. *Proc. A*, 77(519):426–440, 1906.
- [112] F. K. Tsou, E. M. Sparrow, and E. F. Kurtz. Hydrodynamic stability of the boundary layer on a continuous moving surface. *J. Fluid Mech.*, 26:145–161, 1966.
- [113] L. S. Tuckerman and D. Barkley. *Bifurcation analysis for timesteppers*. Springer, 2000.
- [114] J. Vlegaar. Laminar boundary-layer behaviour on continuous, accelerating surfaces. *Chem. Eng. Sci.*, 32(12):1517–1525, 1977.
- [115] T. Von Kármán. Über laminare und turbulente Reibung. *Z. Angew. Math. Mech.*, 1: 233–252, 1921.
- [116] D. Wall and S. Wilson. The linear stability of flat-plate boundary-layer flow of fluid with temperature-dependent viscosity. *Phys. Fluids*, 9(10):2885–2898, 1997.

- [117] M. Wang. *Stability analysis of three-dimensional boundary layers with parabolized stability equations*. PhD thesis, The Ohio State University, 1994.
- [118] J. A. Weideman and S. C. Reddy. A MATLAB differentiation matrix suite. *ACM Trans. Math. Softw.*, 26(4):465-519, 2000.

Appendix A

Numerical Validation of Basic Flow Solutions

A.1 Crane's Flow

Here we give a detailed outline of the numerical schemes used to attain and validate the similarity solutions obtained in Chapter 3. As previously shown the Keller-Box method [60] provided accurate solutions in all cases. Due to a discrepancy between the Keller-Box solutions and our locally self similar solutions in the dissipative regime, a linear finite difference scheme was also used to ensure that the Keller-Box solutions were behaving as expected. This comparison was only possible when the energy and momentum equations were uncoupled.

A.1.1 Shooting Scheme

Recalling our governing boundary layer equations (3.2), where to illustrate our scheme, we focus on the non-dissipative regime $Ec = 0$.

$$\mu f''' + \mu' f'' + f f'' - f'^2 = 0, \quad (\text{A.1a})$$

$$T'' + \text{Pr}(fT' + Ec x^2 \mu (f'')^2) = 0. \quad (\text{A.1b})$$

Note also that we have omitted the y momentum equation as it is simply integrated to attain the pressure and has no bearing on the boundary conditions determined by the shooting scheme.

The boundary conditions are

$$f = f' - 1 = T - 1 = 0 \quad \text{at } \eta = 0, \quad (\text{A.1c})$$

$$f' \rightarrow 0, \quad T \rightarrow 0 \quad \text{as } \eta \rightarrow \infty. \quad (\text{A.1d})$$

To proceed we write our governing equations as a system of first order ODE's as follows

$$f = y_1, \quad f' = y_2, \quad f'' = y_3, \quad T = y_4, \quad T' = y_5.$$

so that

$$y_1' = y_2, \quad (\text{A.2a})$$

$$y_2' = y_3, \quad (\text{A.2b})$$

$$y_3' = 1/\mu (y_2^2 - \mu' y_3 - y_1 y_3), \quad (\text{A.2c})$$

$$y_4' = y_5, \quad (\text{A.2d})$$

$$y_5' = -\text{Pr } y_1 y_5 \quad (\text{A.2e})$$

Our goal is to reformulate this boundary value problem as an initial value problem and determine the initial conditions $y_3(0)$ and $y_5(0)$ so that the free-stream conditions are satisfied. To proceed we solve (A.2) subject to the “guessed” initial conditions

$$y_1(0) = a, \quad y_5(0) = b, \quad (\text{A.3})$$

These guesses are iterated using Newton's method until the free stream conditions $y_2(\eta_\infty)$ and $y_5(\eta_\infty)$ are sufficiently close to zero. This leads to the following

$$\begin{bmatrix} a_{n+1} \\ b_{n+1} \end{bmatrix} = \begin{bmatrix} a_n \\ b_n \end{bmatrix} - \left(\begin{bmatrix} \frac{\partial y_2}{\partial a} & \frac{\partial y_2}{\partial b} \\ \frac{\partial y_5}{\partial a} & \frac{\partial y_5}{\partial b} \end{bmatrix}^{-1} \begin{bmatrix} y_2 \\ y_5 \end{bmatrix} \right) \Bigg|_{\eta=\eta_\infty}$$

where the Jacobian is calculated numerically using finite differences and the ODE's are integrated using a fourth order Runge Kutta scheme. The value of η_∞ is made progressively larger so as to avoid convergence issues associated with poor initial guesses.

A.1.2 Keller-Box Method

Recalling our governing boundary layer PDEs for Crane's flow (2.2)

$$\frac{\partial u}{\partial x} + \frac{\partial v}{\partial y} = 0, \quad (\text{A.4a})$$

$$u \frac{\partial u}{\partial x} + v \frac{\partial u}{\partial y} = \frac{\partial}{\partial y} \left(\mu \frac{\partial u}{\partial y} \right), \quad (\text{A.4b})$$

$$u \frac{\partial T}{\partial x} + v \frac{\partial T}{\partial y} = \text{Pr}^{-1} \frac{\partial^2 T}{\partial y^2} + \text{Ec} \mu \left(\frac{\partial u}{\partial y} \right)^2, \quad (\text{A.4c})$$

and corresponding boundary conditions

$$u - x = v = T - 1 = 0 \quad \text{at } y = 0, \quad (\text{A.4d})$$

$$u \rightarrow T \rightarrow 0 \quad \text{as } y \rightarrow \infty. \quad (\text{A.4e})$$

To validate our similarity solutions we compared them to numerical solutions of the boundary layer equations using the Keller-Box method [60]. The Keller-Box method is an implicit finite difference scheme which has been used to solve a wide variety of nonlinear boundary layer problems. The method is described in detail by Cebeci and Bradshaw [18], however we will provide an explanation of how the method was applied to our extension of Crane's model including both viscothermal and dissipative effects. To apply the Keller-Box method we define

$$\begin{aligned} a = v, \quad b = u, \quad c &= u', \\ d = T, \quad e &= T', \end{aligned}$$

with primes being used to denote differentiation with respect to y . We write our system (3.2) as

$$a' + b_x = 0, \quad (\text{A.5a})$$

$$b' - c = 0, \quad (\text{A.5b})$$

$$\mu(d)(c' - mec) - bb_x - ac = 0, \quad (\text{A.5c})$$

$$d' - e = 0, \quad (\text{A.5d})$$

$$\frac{1}{\text{Pr}} e' - bd_x - ae + \text{Ec} \mu(d) c^2 = 0. \quad (\text{A.5e})$$

To initialise the scheme we set the initial temperature and velocity profiles at $x = 0$, equal to the similarity solutions computed above for a given value of the sensitivity parameter. This is then used as the initial guess for the profile at $x^i = x^{i-1} + \Delta x$. The ODE's are then evaluated

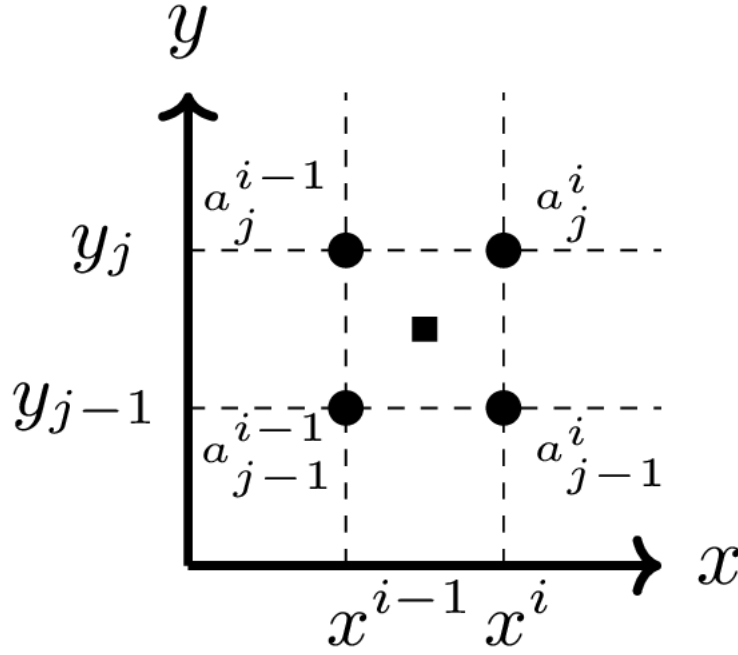


Figure A.1: Diagram outlining how the Keller-Box scheme is discretised.

at $(x^i, y_{j-1/2})$ while the PDE's are evaluated at $(x^{i-1/2}, y_{j-1/2})$. As such it is useful to define the following quantities

$$\begin{aligned}\Delta_y a_j^i &= \frac{1}{2\Delta y_j} (a_j^i + a_j^{i-1} - a_{j-1}^i - a_{j-1}^{i-1}), \\ \Delta_x a_j^i &= \frac{1}{2\Delta x_i} (a_j^i - a_j^{i-1} + a_{j-1}^i - a_{j-1}^{i-1}), \\ a_{j-1/2}^{i-1/2} &= \frac{1}{4} (a_j^i + a_j^{i-1} + a_{j-1}^i + a_{j-1}^{i-1}).\end{aligned}$$

which will be used to simplify the notation in the explanation that follows. The next step is to linearise (A.5). Since a, b, c, d, e are known at the previous step in x, x_{i-1} , we use this as our initial guess at x_i by setting

$$a_j^i = a_j^{i(n)} + \delta a_j^i,$$

where $a_j^{i(0)} = a_j^{i-1}$ and δ denotes a correction to our current guess, which is assumed to be small. To simplify notation the superscripts on the perturbed quantities will be dropped since their x

location is known. The viscosity term is written

$$\begin{aligned}
\mu(d_{j-1/2}^{i-1/2}) &= e^{-m\left(d_{j-1/2}^{i-1/2} + \frac{\delta d_j + \delta d_{j-1}}{4}\right)} \\
&= e^{-m d_{j-1/2}^{i-1/2}} e^{-\frac{m}{4}(\delta d_j + \delta d_{j-1})}, \\
&= e^{-m d_{j-1/2}^{i-1/2}} \left(1 - \frac{m}{4}[\delta d_j + \delta d_{j-1}]\right) + \mathcal{O}(\delta^2), \\
\mu(d_{j-1/2}^{i-1/2}) &= \left[1 + m d_{j-1/2}^{i-1/2} + \frac{m}{4}(\delta d_j + \delta d_{j-1})\right]^{-1}, \\
&= \left[1 + m d_{j-1/2}^{i-1/2}\right]^{-1} \left[1 + \frac{m}{4} \frac{\delta d_j + \delta d_{j-1}}{1 + m d_{j-1/2}^{i-1/2}}\right]^{-1}, \\
&= \left[1 + m d_{j-1/2}^{i-1/2}\right]^{-1} \left(1 - \frac{m}{4} \frac{\delta d_j + \delta d_{j-1}}{1 + m d_{j-1/2}^{i-1/2}}\right) + \mathcal{O}(\delta^2),
\end{aligned}$$

for the exponential and inverse distributions respectively. Substituting this into our first order system yields

$$\alpha_1 \delta a_j + \alpha_2 \delta a_{j-1} + \alpha_3 \delta b_j + \alpha_4 \delta b_{j-1} = r_1, \quad (\text{A.6a})$$

$$\frac{1}{\Delta y}(\delta b_j - \delta b_{j-1}) - \frac{1}{2}(\delta c_j + \delta c_{j-1}) = r_2 = 0, \quad (\text{A.6b})$$

$$\begin{aligned}
\beta_1 \delta a_j + \beta_2 \delta a_{j-1} + \beta_3 \delta b_j + \beta_4 b_{j-1} + \beta_5 \delta c_j + \beta_6 \delta c_{j-1} \\
+ \beta_7 \delta d_j + \beta_8 \delta d_{j-1} + \beta_9 \delta e_j + \beta_{10} \delta e_{j-1} = r_3, \quad (\text{A.6c})
\end{aligned}$$

$$\frac{1}{\Delta y}(\delta d_j - \delta d_{j-1}) - \frac{1}{2}(\delta e_j + \delta e_{j-1}) = r_4 = 0, \quad (\text{A.6d})$$

$$\begin{aligned}
\gamma_1 \delta a_j + \gamma_2 \delta a_{j-1} + \gamma_3 \delta b_j + \gamma_4 \delta b_{j-1} + \gamma_5 \delta c_j + \gamma_6 \delta c_{j-1} \\
+ \gamma_7 \delta d_j + \gamma_8 \delta d_{j-1} + \gamma_9 \delta e_j + \gamma_{10} \delta e_{j-1} = r_5, \quad (\text{A.6e})
\end{aligned}$$

where the coefficients of the corrections in the continuity, momentum, and energy equations are outlined below. Note that we have only imposed that the perturbations satisfy the ordinary differential equations in (A.6b) and (A.6d). While this is a nonstandard way of applying the Keller-Box method, it prevented oscillations from developing in the corrections which in turn prevented the scheme from converging at a sufficiently large distance downstream. Applying the Keller-Box method as suggested in Cebeci and Bradshaw [18] would instead result in

$$r_2 = -\frac{1}{\Delta y}(b_j^i - b_{j-1}^i) + \frac{1}{2}(c_j^i - c_{j-1}^i), \quad (\text{A.7})$$

$$r_4 = -\frac{1}{\Delta y}(d_j^i - d_{j-1}^i) + \frac{1}{2}(e_j^i - e_{j-1}^i). \quad (\text{A.8})$$

However, we will show that our modified version of the method strongly agrees with our similarity solutions for $Ec = 0$ and a finite difference scheme which can only be used when the temperature

and fluid flow are uncoupled as it is unable to handle the nonlinear terms which arise in the coupled case. The errors for the remaining equations are defined

$$r_1 = -\Delta_y a_j^i - \Delta_x b_j^i, \quad (\text{A.9a})$$

$$r_3 = -\mu_{j-1/2}^{i-1/2} \left(\Delta_y c_j^i - m \mu_{j-1/2}^{i-1/2} c_{j-1/2}^{i-1/2} e_{j-1/2}^{i-1/2} \right) + b_{j-1/2}^{i-1/2} \Delta_x b_j^i + a_{j-1/2}^{i-1/2} c_{j-1/2}^{i-1/2}, \quad (\text{A.9b})$$

$$r_5 = -\text{Pr}^{-1} \Delta_y e_j^i + b_{j-1/2}^{i-1/2} \Delta_x d_j^i + a_{j-1/2}^{i-1/2} e_{j-1/2}^{i-1/2} - \text{Ec} \mu_{j-1/2}^{i-1/2} \left(c_{j-1/2}^{i-1/2} \right)^2. \quad (\text{A.9c})$$

The coefficients of the continuity equation are

$$\alpha_1 = -\alpha_2 = \frac{1}{2\Delta y}, \quad (\text{A.10a})$$

$$\alpha_3 = \alpha_4 = \frac{1}{2\Delta x}. \quad (\text{A.10b})$$

For the momentum equation we have

$$\beta_1 = \beta_2 = -\frac{1}{4} c_{j-1/2}^{i-1/2}, \quad (\text{A.11a})$$

$$\beta_3 = \beta_4 = -\frac{1}{4} \Delta_x b_j^i - \frac{1}{2\Delta x} b_{j-1/2}^{i-1/2}, \quad (\text{A.11b})$$

$$\beta_5 = \mu_{j-1/2}^{i-1/2} \left[\frac{1}{2\Delta y} - \frac{m}{4} \mu_{j-1/2}^{i-1/2} e_{j-1/2}^{i-1/2} \right] + \frac{1}{4} a_{j-1/2}^{i-1/2}, \quad (\text{A.11c})$$

$$\beta_6 = \mu_{j-1/2}^{i-1/2} \left[-\frac{1}{2\Delta y} - \frac{m}{4} \mu_{j-1/2}^{i-1/2} e_{j-1/2}^{i-1/2} \right] + \frac{1}{4} a_{j-1/2}^{i-1/2}, \quad (\text{A.11d})$$

$$\beta_7 = \beta_8 = -\frac{m}{4} \left(\mu_{j-1/2}^{i-1/2} \right)^2 \left(\Delta_y c_j^i - 2m \mu_{j-1/2}^{i-1/2} c_{j-1/2}^{i-1/2} e_{j-1/2}^{i-1/2} \right), \quad (\text{A.11e})$$

$$\beta_9 = \beta_{10} = -\frac{m}{4} \left(\mu_{j-1/2}^{i-1/2} \right)^2 c_{j-1/2}^{i-1/2}. \quad (\text{A.11f})$$

Finally, for the energy equation we have

$$\gamma_1 = \gamma_2 = -\frac{1}{4} e_{j-1/2}^{i-1/2}, \quad (\text{A.12a})$$

$$\gamma_3 = \gamma_4 = -\frac{1}{4} \Delta_x d_j^i, \quad (\text{A.12b})$$

$$\gamma_5 = \gamma_6 = \frac{\text{Ec}}{2} \mu_{j-1/2}^{i-1/2} c_{j-1/2}^{i-1/2}, \quad (\text{A.12c})$$

$$\gamma_7 = \gamma_8 = -\frac{1}{2\Delta x} b_{j-1/2}^{i-1/2} - \frac{\text{Ec}}{4} m \left(\mu_{j-1/2}^{i-1/2} c_{j-1/2}^{i-1/2} \right)^2, \quad (\text{A.12d})$$

$$\gamma_9 = \frac{1}{2\text{Pr} \Delta y} - \frac{1}{4} a_{j-1/2}^{i-1/2}, \quad (\text{A.12e})$$

$$\gamma_{10} = -\frac{1}{2\text{Pr} \Delta y} - \frac{1}{4} a_{j-1/2}^{i-1/2}, \quad (\text{A.12f})$$

Where we have used the inverse rather than the exponential viscosity distribution in our derivation of the numerical scheme. However, this could be easily interchanged. Now we write our

system in block tridiagonal form such that

$$\bar{A}\bar{\Delta} = \bar{R} \quad (\text{A.13})$$

$$= \begin{bmatrix} B_1 & C_1 & 0 & \cdots & 0 & 0 & 0 \\ A_2 & B_2 & C_2 & \cdots & 0 & 0 & 0 \\ \vdots & \vdots & \vdots & \ddots & \ddots & \ddots & \vdots \\ 0 & 0 & 0 & \cdots & 0 & A_J & B_J \end{bmatrix} \begin{bmatrix} \Delta_1 \\ \Delta_2 \\ \vdots \\ \Delta_J \end{bmatrix} = \begin{bmatrix} R_1 \\ R_2 \\ \vdots \\ R_J \end{bmatrix}. \quad (\text{A.14})$$

To determine the matrices and vectors in this block system we need only to consider a system with two points in the y direction, from which the full system can be easily derived

$$\begin{bmatrix} 1 & 0 & 0 & 0 & 0 & 0 & 0 & 0 & 0 & 0 \\ 0 & 1 & 0 & 0 & 0 & 0 & 0 & 0 & 0 & 0 \\ 0 & 0 & 0 & 1 & 0 & 0 & 0 & 0 & 0 & 0 \\ 0 & 0 & 0 & -\frac{1}{\Delta y} & -\frac{1}{2} & 0 & 0 & 0 & \frac{1}{\Delta y} & -\frac{1}{2} \\ 0 & -\frac{1}{\Delta y} & -\frac{1}{2} & 0 & 0 & 0 & \frac{1}{\Delta y} & -\frac{1}{2} & 0 & 0 \\ \beta_2 & \beta_4 & \beta_6 & \beta_8 & \beta_{10} & \beta_1 & \beta_3 & \beta_5 & \beta_7 & \beta_9 \\ \alpha_2 & \alpha_4 & 0 & 0 & 0 & \alpha_1 & \alpha_3 & 0 & 0 & 0 \\ \gamma_2 & \gamma_4 & \gamma_6 & \gamma_8 & \gamma_{10} & \gamma_1 & \gamma_3 & \gamma_5 & \gamma_7 & \gamma_9 \\ 0 & 0 & 0 & 0 & 0 & 0 & 1 & 0 & 0 & 0 \\ 0 & 0 & 0 & 0 & 0 & 0 & 0 & 0 & 1 & 0 \end{bmatrix} \begin{bmatrix} \delta a_1 \\ \delta b_1 \\ \delta c_1 \\ \delta d_1 \\ \delta e_1 \\ \delta a_2 \\ \delta b_2 \\ \delta c_2 \\ \delta d_2 \\ \delta e_2 \end{bmatrix} = \begin{bmatrix} -a_1^i \\ x^i - b_1^i \\ 1 - d_1^i \\ 0 \\ 0 \\ r_3 \\ r_1 \\ r_5 \\ -b_2^i \\ -d_2^i \end{bmatrix}. \quad (\text{A.15})$$

Here we have exchanged rows in order to ensure that the main diagonal sub matrix is non singular. This required in order to be able to apply of block version of the TDMA algorithm. Note that the ordering is not unique. At a general, internal point y_j we have

$$A_j = \begin{bmatrix} \beta_1 & \beta_3 & \beta_5 & \beta_7 & \beta_9 \\ \alpha_1 & \alpha_3 & 0 & 0 & 0 \\ \gamma_1 & \gamma_3 & \gamma_5 & \gamma_7 & \gamma_9 \\ 0 & 0 & 0 & 0 & 0 \\ 0 & 0 & 0 & 0 & 0 \end{bmatrix}, \quad B_j = \begin{bmatrix} \beta_2 & \beta_4 & \beta_6 & \beta_8 & \beta_{10} \\ \alpha_2 & \alpha_4 & 0 & 0 & 0 \\ \gamma_2 & \gamma_4 & \gamma_6 & \gamma_8 & \gamma_{10} \\ 0 & 0 & 0 & -\frac{1}{\Delta y} & -\frac{1}{2} \\ 0 & -\frac{1}{\Delta y} & -\frac{1}{2} & 0 & 0 \end{bmatrix}, \quad (\text{A.16})$$

$$C_j = \begin{bmatrix} 0 & 0 & 0 & 0 & 0 \\ 0 & 0 & 0 & 0 & 0 \\ 0 & 0 & 0 & 0 & 0 \\ 0 & 0 & 0 & -\frac{1}{\Delta y} & -\frac{1}{2} \\ 0 & -\frac{1}{\Delta y} & -\frac{1}{2} & 0 & 0 \end{bmatrix}, \quad R_j = \begin{bmatrix} r_3 \\ r_1 \\ r_5 \\ r_4 \\ r_2 \end{bmatrix}, \quad (\text{A.17})$$

with the only changes occurring in B and R at either boundary. On the surface of the sheet we have

$$B_1 = \begin{bmatrix} 1 & 0 & 0 & 0 & 0 \\ 0 & 1 & 0 & 0 & 0 \\ 0 & 0 & 0 & 1 & 0 \\ 0 & 0 & 0 & -\frac{1}{\Delta y} & -\frac{1}{2} \\ 0 & -\frac{1}{\Delta y} & -\frac{1}{2} & 0 & 0 \end{bmatrix}, \quad R_1 = \begin{bmatrix} -a_1^i \\ x^i - b_1^i \\ 1 - d_1^i \\ r_4 \\ r_2 \end{bmatrix}, \quad (\text{A.18})$$

while at the free stream we get

$$B_J = \begin{bmatrix} \beta_2 & \beta_4 & \beta_6 & \beta_8 & \beta_{10} \\ \alpha_2 & \alpha_4 & 0 & 0 & 0 \\ \gamma_2 & \gamma_4 & \gamma_6 & \gamma_8 & \gamma_{10} \\ 0 & 1 & 0 & 0 & 0 \\ 0 & 0 & & 1 & 0 \end{bmatrix}, \quad R_J = \begin{bmatrix} r_2 \\ r_1 \\ r_5 \\ -b_J^i \\ -d_J^i \end{bmatrix}, \quad (\text{A.19})$$

The problem was solved on for $[x, y] \in [0, 0] \times [10, 20]$ with a step size of 0.01 in the x direction. To reduce the computational cost the y coordinate, which was originally linearly spaced, with one quarter the density of the x mesh was transformed using

$$\hat{y} = y \exp\left(\frac{y - Y_{max}}{Y_{max}}\right)$$

to concentrate the density of the mesh near the surface of the sheet.

A.1.3 TDMA Scheme

Here we will provide a brief explanation of the finite difference scheme employed to validate the Keller-Box code in the dissipative regime with constant viscosity. The objective is to construct a linear system $Ax = b$, using the known solutions at x^i to update the solutions at x^{i+1} . Since the momentum and energy equations are uncoupled we consider them separately. The continuity and momentum equations are approximated as follows

$$\frac{1}{\Delta y} [v_j^{i+1} - v_{j-1}^{i+1}] = -\frac{1}{2\Delta x} [u_j^{i+1} - u_j^i + u_{j-1}^{i+1} - u_{j-1}^i], \quad (\text{A.20})$$

$$\frac{u_j^i}{\Delta x} [u_j^{i+1} - u_j^i] + \frac{v_j^i}{2\Delta y} [u_{j+1}^{i+1} - u_{j-1}^{i+1}] = \frac{1}{(\Delta y)^2} [u_{j+1}^{i+1} - 2u_j^{i+1} + u_{j-1}^{i+1}] \quad (\text{A.21})$$

Where the finite difference approximations are chosen to ensure the system is linear in the unknown u_j^{i+1} terms. Since we know the free stream, wall and left boundary conditions we can

use the TDMA algorithm to iteratively solve successive u 's along the x direction and use the continuity equation to update v . The x momentum equation at some fixed x_i may be represented as the linear system $Ax = b$ for $j \in [2, n - 1]$

$$A = \begin{bmatrix} \frac{2}{(\Delta y)^2} + \frac{u_2^i}{\Delta x} & -\frac{1}{(\Delta y)^2} + \frac{v_2^i}{2\Delta y} & \cdots & 0 & 0 \\ -\frac{1}{(\Delta y)^2} - \frac{v_3^i}{2\Delta y} & \frac{2}{(\Delta y)^2} + \frac{u_3^i}{\Delta x} & -\frac{1}{(\Delta y)^2} + \frac{v_3^i}{2\Delta y} & 0 & 0 \\ \vdots & \vdots & \vdots & \ddots & \vdots \\ 0 & 0 & \cdots & -\frac{1}{(\Delta y)^2} - \frac{v_{n-1}^i}{2\Delta y} & \frac{2}{(\Delta y)^2} + \frac{u_{n-1}^i}{\Delta x} \end{bmatrix}$$

$$x = \begin{bmatrix} u_2^{i+1} \\ u_3^{i+1} \\ \vdots \\ u_{n-1}^{i+1} \end{bmatrix}, \quad b = \begin{bmatrix} \frac{(u_2^i)^2}{\Delta x} - \left(-\frac{1}{(\Delta y)^2} - \frac{v_2^i}{2\Delta y}\right)u_1^{i+1} \\ \frac{(u_3^i)^2}{\Delta x} \\ \vdots \\ \frac{(u_{n-1}^i)^2}{\Delta x} - \left(-\frac{1}{(\Delta y)^2} + \frac{v_{n-1}^i}{2\Delta y}\right)u_n^{i+1} \end{bmatrix}.$$

Which is solved using the TDMA algorithm. After updating u and solving for v , the temperature equation is solved using the same approach before marching forward in the x direction.

$$\frac{u_j^i}{\Delta x} [T_j^{i+1} - T_j^i] + \frac{v_j^i}{2\Delta y} [T_{j+1}^{i+1} - T_{j-1}^{i+1}] = \frac{1}{\text{Pr}(\Delta y)^2} [T_{j+1}^{i+1} - 2T_j^{i+1} + T_{j-1}^{i+1}] + \text{Ec} \left(\frac{u_j^{i+1} - u_{j-1}^{i+1}}{(\Delta y)^2} \right)^2. \quad (\text{A.22})$$

Or

$$A = \begin{bmatrix} \frac{2}{\text{Pr}(\Delta y)^2} + \frac{u_2^i}{\Delta x} & -\frac{1}{\text{Pr}(\Delta y)^2} + \frac{v_2^i}{2\Delta y} & \cdots & 0 & 0 \\ -\frac{1}{\text{Pr}(\Delta y)^2} - \frac{v_3^i}{2\Delta y} & \frac{2}{\text{Pr}(\Delta y)^2} + \frac{u_3^i}{\Delta x} & -\frac{1}{\text{Pr}(\Delta y)^2} + \frac{v_3^i}{2\Delta y} & 0 & 0 \\ \vdots & \vdots & \vdots & \ddots & \vdots \\ 0 & 0 & \cdots & -\frac{1}{\text{Pr}(\Delta y)^2} - \frac{v_{n-1}^i}{2\Delta y} & \frac{2}{\text{Pr}(\Delta y)^2} + \frac{u_{n-1}^i}{\Delta x} \end{bmatrix},$$

$$x = \begin{bmatrix} T_2^{i+1} \\ T_3^{i+1} \\ \vdots \\ T_{n-1}^{i+1} \end{bmatrix}, \quad b = \begin{bmatrix} \frac{u_2^i T_2^i}{\Delta x} + \frac{\text{Ec}}{\text{Pr}(\Delta y)^2} (u_2^{i+1} - u_j^1)^2 - \left(-\frac{1}{\text{Pr}(\Delta y)^2} - \frac{v_2^i}{2\Delta y}\right)u_1^{i+1} \\ \frac{u_3^i T_3^i}{\Delta x} + \frac{\text{Ec}}{\text{Pr}(\Delta y)^2} (u_3^{i+1} - u_2^{i+1})^2 \\ \vdots \\ \frac{u_{n-1}^i T_{n-1}^i}{\Delta x} + \frac{\text{Ec}}{\text{Pr}(\Delta y)^2} (u_n^{i+1} - u_{n-1}^{i+1})^2 - \left(-\frac{1}{\text{Pr}(\Delta y)^2} + \frac{v_{n-1}^i}{2\Delta y}\right)u_n^{i+1} \end{bmatrix}.$$

Appendix B

Derivation of Deforming Boundary Layer Solutions

B.1 Self-similar solutions in the limit as $c_i \rightarrow 0$

In the first instance we consider the case when $c_1 = 0$. This is directly equivalent to the case when $\gamma = -2$. From (3.10a) it is immediately apparent that if $c_1 = 0$, then it must be the case that $X_+ = 0$. Solving this resulting ODE we determine that $g = k\sqrt{(\xi U_w)^{-1}\sigma}$, where k is a constant of integration. Thus from (3.10b) it follows that $U_w = -c_2^{-1}k^2\mathcal{I}^{-1}$. Given that we consider only cases where the wall velocity is positive we fix $c_2 = -k^2$. Now, by writing $\hat{f}(Z) = kf(\zeta) = \psi$, where $Z = k\zeta = \sigma^{-1}\eta U_w$, we have that $u_0 = \sigma^{-1}U_w\hat{f}'_Z$, and $v_0 = Z\hat{f}'_Z[\sigma^{-1}\sigma'_\xi - U_w^{-1}(U_w)'_\xi]$. The ODE that governs the flow is then

$$\hat{f}'''_{ZZZ} + (\hat{f}'_Z)^2 = 0,$$

which must be solved subject to

$$\hat{f}(0) = 0, \quad \hat{f}'_Z(0) = 1, \quad \hat{f}'_Z(\infty) = 0.$$

The ODE in question can be integrated to give

$$\frac{1}{2}(\hat{f}''_{ZZ})^2 + \frac{1}{3}(\hat{f}'_Z)^3 = 0.$$

The right-hand side of the above must be equal to zero to ensure that the far-field condition is satisfied. In the limit as $Z \rightarrow 0$ it then follows that

$$\frac{1}{2}[\hat{f}''_{ZZ}(0)]^2 = -\frac{1}{3}.$$

Clearly, this cannot be true and, as such, we determine that no real solutions exist in the case when $\gamma = -2$ ($c_1 = 0$). This result is analogous to that associated with the Falkner-Skan problem in the limit as $m \rightarrow -1$. In that case one is unable to determine the flow in a diverging channel due to the very rapid deceleration of the free-stream velocity. We interpret our result in much the same way, given that U_w is inversely proportional to \mathcal{I} we conclude that the rapid change of the wall velocity to zero is such that a boundary-layer cannot be accommodated by this analysis.

In the second instance we consider the case when $c_2 = 0$. This is directly equivalent to the case when $\gamma \rightarrow \infty$. From (3.10b) it is immediately apparent that if $c_2 = 0$, then it must be the case that $U_w = \text{constant}$. Given this result we determine, from (3.10a), that $g = k\sqrt{\xi^{-1}\mathcal{J}\sigma}$, where k is a constant of integration fixed such that $2c_1 = k^2$, and $\mathcal{J} = C + \mathcal{I}$. Now, by writing $\hat{f}(Z) = kf(\zeta) = \psi/\sqrt{\mathcal{J}U_w}$, where $Z = k\zeta = \sigma^{-1}\eta\sqrt{\mathcal{J}^{-1}U_w}$ we have that $u_0 = \sigma^{-1}U_w\hat{f}'_Z$, and

$$v_0 = \frac{\sigma}{2}\sqrt{\frac{U_w}{\mathcal{J}}}\left\{\left[\frac{2\mathcal{J}\sigma'_\xi}{\sigma^2} + 1\right]Z\hat{f}'_Z - \hat{f}\right\}.$$

The ODE that governs the flow is then

$$\hat{f}'''_{ZZZ} + \frac{\hat{f}\hat{f}''_{ZZ}}{2} = 0,$$

which must be solved subject to

$$\hat{f}(0) = 0, \quad \hat{f}'_Z(0) = 1, \quad \hat{f}'_Z(\infty) = 0.$$

The above ODE and boundary conditions are identical to those presented by Tsou *et al.* [112] who considered purely the case when $s(\xi) = 0$. Thus, in all cases when the wall velocity is constant, the boundary-layer flow over non-flat surfaces can be determined from the solutions associated with the flow over a flat smooth boundary.

There is a special case to consider when $\sigma/\sqrt{\mathcal{J}} = d_1 = \text{constant}$. In this case v_0 is a function of Z only. It follows that

$$\sigma = \frac{d_1}{2}(d_2 + d_1\xi),$$

where $C = d_2^2/4$. Stipulating that $s_0 = 0$, and fixing $d_1/2 = d_2 = 1$, gives

$$s(\xi) = \frac{\sigma\sqrt{\mathcal{I}}}{2} - \frac{1}{2} \ln\left(\sqrt{\frac{\sigma-1}{2}} + \sqrt{\frac{\sigma+1}{2}}\right).$$

Then $\sigma u_0/U_w = \hat{f}'_Z$, and $v_0/\sqrt{U_w} = (2Z\hat{f}'_Z - \hat{f})$.

B.2 Derivation of the exact solutions

Consider equation (3.17). For convenience we define $q = 2/(2+\gamma)$ so that now we seek solutions to

$$\hat{f}'''_{ZZZ} + \hat{f}\hat{f}''_{ZZ} - q(\hat{f}'_Z)^2 = 0,$$

subject to

$$\hat{f}(0) = 0, \quad \hat{f}'_Z(0) = 1, \quad \hat{f}'_Z(\infty) = 0.$$

Following the same approach as Sachdev *et al.* [93] we suppose that

$$\hat{f}(Z) = b + b \sum_{n=1}^{\infty} A^n \hat{a}_n e^{-bnZ} \quad \text{where} \quad A = \frac{a_1}{b} \quad \text{and} \quad \hat{a}_1 = 1. \quad (\text{B.1})$$

The constants a_1 , \hat{a}_n and b need to be determined. Note $\hat{f}'_Z(\infty) = 0$ is already satisfied. Substituting this expression for \hat{f} into the ODE gives

$$\sum_{n=2}^{\infty} A^n e^{-bnZ} \left(-\hat{a}_n n^2 (n-1) + \sum_{j=1}^{n-1} \hat{a}_j \hat{a}_{n-j} (n-j)[n - (q+1)j] \right) = 0.$$

To satisfy this we require that

$$\hat{a}_n = \frac{1}{n^2(n-1)} \sum_{j=1}^{n-1} \hat{a}_j \hat{a}_{n-j} (n-j)[n - (q+1)j] \quad \text{for} \quad n \geq 2. \quad (\text{B.2})$$

The first few values are given by

$$\begin{aligned} \hat{a}_2 &= \frac{1-q}{4}, & \hat{a}_3 &= \frac{1-q}{72}(5-4q), & \hat{a}_4 &= \frac{1-q}{1728}(34-53q+21q^2), \\ \hat{a}_5 &= \frac{1-q}{172800}(968-2235q+1741q^2-456q^3), & & \dots & & \end{aligned}$$

Using $\hat{f}(0) = 0$ we obtain

$$\sum_{n=1}^{\infty} A^n \hat{a}_n = -1, \quad (\text{B.3})$$

which is a polynomial in the unknown A . By truncating this to a finite series we can numerically obtain the value of A . The condition $\hat{f}'_Z(0) = 1$ yields

$$b = \frac{1}{\sqrt{-\sum_{n=1}^{\infty} n\hat{a}_n A^n}}. \quad (\text{B.4})$$

With A and b known, we can determine a_1 using $a_1 = Ab$.

Special case: $q = 1$

If $q = 1$, then $\hat{a}_n = 0$ for $n \geq 2$ and therefore

$$\hat{f}(Z) = b + a_1 e^{-bZ}.$$

Applying our boundary conditions yields $a_1 = b = 1$. Hence

$$\hat{f}(Z) = 1 + e^{-Z}.$$

Special case: $q = -1$

If $q = -1$, then equation (B.2) reduces to

$$\hat{a}_n = \frac{1}{n(n-1)} \sum_{j=1}^{n-1} \hat{a}_j \hat{a}_{n-j} (n-j) \quad \text{for } n \geq 2.$$

With $\hat{a}_1 = 1$, the solution is given by $\hat{a}_n = 2^{1-n}$. Thus one finds that

$$\hat{f}(Z) = b + 2b \sum_{n=1}^{\infty} \left(\frac{A}{2} e^{-bZ}\right)^n = b \frac{2 + Ae^{-bZ}}{2 - Ae^{-bZ}}.$$

Substituting this solution into $\hat{f}(0) = 0$ gives $A = -2$. Further $\hat{f}'_Z(0) = 1$ gives $b^2 = 2$, hence

$$\hat{f}(Z) = \sqrt{2} \frac{1 - e^{-\sqrt{2}Z}}{1 + e^{-\sqrt{2}Z}} = \sqrt{2} \tanh\left(\frac{Z}{\sqrt{2}}\right).$$

Appendix C

Numerical Solution of Linear Disturbance Equation

C.1 Chebychev Spectral Scheme

All of the stability calculations performed in this thesis have implemented a Chebychev spectral scheme to discretise the linear disturbance equations. In contrast to the finite difference based methods used to calculate the basic flows outlined in Appendix A, spectral schemes are global since flow quantities are expanded as a linear combination of basis functions which span the entire domain. This means that the derivative of a function depends on all its values across the entire flow domain, and not just on neighbouring nodes. Such schemes are commonly employed in the literature, since they provide the greatest resolution for a given number of nodes. However, the global nature of the approximations made means that the resulting linear system is dense, rather than sparse. The trade-off between storage requirements and accuracy poses a challenge for naively applying spectral schemes for two and three dimensional problems. However, for the one-dimensional problems considered here, storage requirements are modest, and global spectral schemes can be readily applied.

Numerical discretisation is performed at the Chebychev-Gauss-Lobatto (CGL) points

$$\hat{y}_j = \cos(j\pi/N), \quad j = 0, 1, \dots, N.$$

This choice of collocation points, clusters grid points near the boundaries and minimises errors in the form of oscillations near the endpoints observed when interpolating high order polynomials over an equispaced grid. The CGL points are defined over the interval $\hat{y} \in [-1, 1]$, however we are interested in applying the scheme to solve boundary layer problems defined for $y \in [0, \infty)$,

where the semi-infinite domain is truncated at $y = y_{\max}$, to facilitate numerical computation. As such we choose the following mapping to map our computational domain, to the physical domain [97]

$$y = a \frac{1 + \hat{y}}{b - \hat{y}},$$

where

$$a = \frac{y_i y_{\max}}{y_{\max} - 2y_i}, \quad b = 1 + \frac{2a}{y_{\max}}.$$

This choice of mapping clusters half of the collocation points in the interval $[0, y_i]$, to ensure accurate resolution in the near wall boundary layer. For all computations in the thesis the following choice of parameter values

$$N = 100, \quad y_{\max} = 40, \quad \text{and } y_i = 4,$$

was found to provide fully converged numerical solutions. An arbitrary function $f(y)$, defined on the CGL points is expressed as the weighted sum of the first N Chebychev polynomials $\mathcal{T}_n = \cos(n \arccos(y))$ such that

$$f(\hat{y}) = \sum_{n=0}^N a_n \mathcal{T}_n(\hat{y}).$$

Differentiation is performed by multiplication of the derivative matrix \mathcal{D} , which is defined as follows [109]

$$\begin{aligned} \mathcal{D}_{0,0} &= \frac{2N^2 + 1}{6}, & \mathcal{D}_{N,N} &= -\frac{2N^2 + 1}{6}, \\ \mathcal{D}_{j,j} &= -\frac{\hat{y}_j}{2(1 - \hat{y}_j)^2}, & j &= 1, \dots, N-1, \\ \mathcal{D}_{i,j} &= \frac{c_i}{c_j} \frac{(-1)^{i+j}}{(\hat{y}_i - \hat{y}_j)^2}, & i \neq j, \quad i, j &= 1, \dots, N-1, \end{aligned}$$

where

$$c_i = \begin{cases} 2, & \text{if } i = 0 \text{ or } N \\ 1, & \text{otherwise.} \end{cases}$$

Higher order derivatives are obtained by repeated matrix multiplication. Due to our boundary layer mapping, these derivatives have to be transformed using the chain rule

$$\begin{aligned} \frac{d}{dy} &= \frac{d\hat{y}}{dy} \frac{d}{d\hat{y}} = \frac{a(b+1)}{a+y} \frac{d}{d\hat{y}}, \\ \frac{d^2}{dy^2} &= \left(\frac{d\hat{y}}{dy} \right)^2 \frac{d^2}{d\hat{y}^2} + \frac{d^2\hat{y}}{dy^2} \frac{d}{d\hat{y}} = \left(\frac{a(b+1)}{a+y} \right)^2 \frac{d^2}{d\hat{y}^2} - 2a \frac{1+b}{(a+y)^3} \frac{d}{d\hat{y}}, \end{aligned}$$

and likewise for the higher order derivatives in the Orr-Sommerfeld formulation.

Similarly, we can derive a spectrally accurate Chebychev integration matrix to evaluate the perturbation kinetic energy. This is defined as follows

$$\int_{-1}^1 f(\hat{y}) d\hat{y} = \sum_{j=0}^N f(y_j) \mathcal{W}(y_j),$$

here $\mathcal{W}(y_j)$ is the Chebychev integration matrix. This may be derived by considering

$$f(\hat{y}) = \sum_{n=0}^N a_n \mathcal{T}_n(\hat{y}) = \sum_{n=0}^N c_n \mathcal{T}_n(\hat{y}) \sum_{i=0}^N \frac{b_i}{N} \mathcal{T}_n(\hat{y}_i), \quad (\text{C.1})$$

where we have used the discrete orthogonality conditions to determine the expansion coefficients a_n such that

$$a_n = \frac{c_n}{N} \sum_{i=0}^N b_i f(\hat{y}_i) \mathcal{T}_n(\hat{y}_i),$$

where $b_0 = b_N = 1/2$, $b_i = 1$, and $c_0 = c_N = 1$, $c_n = 2$. Integrating (C.1) with respect to \hat{y} we have

$$\int_{-1}^1 f(\hat{y}) d\hat{y} = \frac{1}{N} \sum_{j=0}^N b_j f(\hat{y}_j) \sum_{n=0}^N c_n \mathcal{T}_n(\hat{y}_j) \int_{-1}^1 \mathcal{T}_n(\hat{y}) d\hat{y}.$$

Now

$$\int_{-1}^1 \mathcal{T}_n(\hat{y}) d\hat{y} = \begin{cases} 0, & \text{if } n \text{ is odd,} \\ \frac{2}{1-n^2}, & \text{if } n \text{ is even.} \end{cases}$$

Therefore we have

$$\mathcal{W}(\hat{y}_j) = \frac{b_j}{N} \left[2 + \sum_{n=2}^N c_n \frac{1 + (-1)^n}{1 - n^2} \cos\left(\frac{j\pi}{n}\right) \right],$$

where again we need to account for our boundary layer mapping in our integral such that

$$\mathcal{W}(y_j) = \frac{b_j}{N} \sum_{n=0}^N c_n \cos\left(\frac{j\pi}{n}\right) \int_{-1}^1 T_n(\hat{y}) \frac{dy}{d\hat{y}} d\hat{y},$$

Appendix D

PSE

Here we present our formulation used for the preliminary analysis of non-parallel effects for Crane's flow using the PSE in Chapter 8, Section 8.1.2. We restrict our attention to the two-dimensional development of disturbances although our scheme could be easily generalised to account for a third homogenous spatial dimension. The beginning of our formulation follows the derivation of the corresponding Orr-Sommerfeld-Squire system in Chapter 6 but is presented here in full for clarity.

Starting with the dimensional continuity and Navier-Stokes equations we have

$$\nabla \cdot \mathbf{u}^* = 0, \quad (\text{D.1a})$$

$$\rho^* \frac{D\mathbf{u}^*}{Dt^*} = -\frac{1}{\rho^*} p^* + \nu^* \nabla^2 \mathbf{u}^*. \quad (\text{D.1b})$$

The velocity, pressure and time scales are $a^* x_s^*$, $\rho^* (a^* x_s^*)^2$ and $L^*/a^* x_s^*$, where $L^* = \sqrt{\nu^*/a^*}$ is the non-dimensionalising length scale. To initialise our PSE scheme, local solutions are obtained at a dimensional location x_s^* . This leads to the definition of a local Reynolds $R = x_s^* a^* L^*/\nu^* = x_s^*/L^* = x_s$ and is equivalent to the dimensionless streamwise location. Thus the scheme is initialised at a local x location where the variable x is replaced by the Reynolds number as for the temperature dependent problem. Both of these quantities are identical to those defined in Chapter 6 for the isothermal, non-modal analysis. As before, the mean flow quantities are

perturbed as follows

$$u = \frac{x}{R}U(y) + \tilde{u}, \quad (\text{D.1c})$$

$$v = \frac{1}{R}V(y) + \tilde{v}, \quad (\text{D.1d})$$

$$p = \frac{1}{R^2}P(y) + \tilde{p}, \quad (\text{D.1e})$$

where the basic flow terms are exact solutions to the Navier-Stokes equations and are given by

$$U = e^{-y}, \quad V = e^{-y} - 1, \quad P = P_0 + \frac{1 - e^{-2y}}{2}.$$

It is from here that our analysis diverges from the local analysis of Chapters 4 and 6. Since we seek to evaluate the non-parallel growth of the disturbances we proceed by expanding our perturbation variables as follows

$$\tilde{\mathbf{q}}(x, y, t) = \hat{\mathbf{q}}(x, y) \exp \left[i \int_{x_s}^x \alpha(\xi) d\xi - i\omega t \right],$$

where $\tilde{\mathbf{q}} = (\tilde{u}, \tilde{v}, \tilde{p})$. In order to parabolise the linearised Navier-Stokes equations, it is assumed that the flow varies slowly in the streamwise direction. This assumption implies that

$$\frac{\partial}{\partial x}, V \sim \mathcal{O}(R^{-1}).$$

As a result, second order derivative terms in x are of $\mathcal{O}(R^{-2})$ and are neglected. First order derivatives of the perturbations are expressed as follows

$$\frac{\partial \tilde{\mathbf{q}}}{\partial x} = \left(i\alpha \hat{\mathbf{q}} + \frac{\partial \hat{\mathbf{q}}}{\partial x} \right) \exp \left[i \int_{x_s}^x \alpha(\xi) d\xi - i\omega t \right].$$

Substituting this into the Navier-Stokes equations we attain

$$\frac{\partial \hat{u}}{\partial x} + i\alpha \hat{u} + \frac{\partial \hat{v}}{\partial y} = 0, \quad (\text{D.2a})$$

$$\begin{aligned} & -i\omega \hat{u} + \frac{x}{R} \left(U \frac{\partial \hat{u}}{\partial x} + i\alpha U \hat{u} + \frac{\partial U}{\partial y} \hat{v} \right) + \frac{1}{R} \left(U \hat{u} + V \frac{\partial \hat{u}}{\partial y} \right) = \\ & - \frac{\partial \hat{p}}{\partial x} - i\alpha \hat{p} + \frac{1}{R} \left(\frac{\partial^2 \hat{u}}{\partial y^2} - \alpha^2 \hat{u} \right), \end{aligned} \quad (\text{D.2b})$$

$$\begin{aligned} & -i\omega \hat{v} + \frac{xU}{R} \left(\frac{\partial \hat{v}}{\partial x} + i\alpha \hat{v} \right) + \frac{1}{R} \left(V \frac{\partial \hat{v}}{\partial y} + \frac{\partial V}{\partial y} \hat{v} \right) = \\ & - \frac{\partial \hat{p}}{\partial y} + \frac{1}{R} \left(\frac{\partial^2 \hat{v}}{\partial y^2} - \alpha^2 \hat{v} \right). \end{aligned} \quad (\text{D.2c})$$

The system is closed subject to the boundary conditions

$$\hat{u} = \hat{v} = 0 \quad \text{at } y = 0, \infty. \quad (\text{D.2d})$$

For convenient numerical discretisation, the above system may be written in the equivalent form

$$\mathcal{A}\hat{\mathbf{q}} + \mathcal{B}\frac{\partial\hat{\mathbf{q}}}{\partial y} + \mathcal{C}\frac{\partial\hat{\mathbf{q}}}{\partial y} + \mathcal{D}\frac{\partial\hat{\mathbf{q}}}{\partial x} = 0,$$

where the entries of the matrices are defined as follows [57]

$$\mathcal{A} = \begin{bmatrix} i\alpha & 0 & 0 \\ \zeta + \frac{U}{R} & \frac{x}{R}\frac{\partial U}{\partial y} & i\alpha \\ 0 & \zeta + \frac{1}{R}\frac{\partial V}{\partial y} & 0 \end{bmatrix}, \quad \mathcal{B} = \begin{bmatrix} 0 & 1 & 0 \\ \frac{V}{R} & 0 & 0 \\ 0 & \frac{V}{R} & 1 \end{bmatrix},$$

$$\mathcal{C} = \begin{bmatrix} 0 & 0 & 0 \\ -\frac{1}{R} & 0 & 0 \\ 0 & -\frac{1}{R} & 0 \end{bmatrix}, \quad \mathcal{D} = \begin{bmatrix} 1 & 0 & 0 \\ \frac{xU}{R} & 0 & 1 \\ 0 & \frac{xU}{R} & 0 \end{bmatrix},$$

where

$$\zeta = -i\omega + \frac{1}{R}(i\alpha xU + \alpha^2).$$

Discretisation in the wall normal direction is performed using the Chebychev spectral scheme outlined in Appendix C. Starting with a local solution obtained by solving the corresponding quadratic eigenvalue problem for a given (R, ω) , solutions are marched downstream using a first order backwards Euler scheme. Given that both the phase and amplitude of the perturbation evolve in the streamwise direction, at each step of the marching scheme the value of α is iterated to satisfy the so-called auxiliary condition. While there are many ways this quantity can be defined, here we choose

$$\int_0^\infty \hat{\mathbf{q}}^\dagger \frac{\partial\hat{\mathbf{q}}}{\partial x} dy = 0.$$

This condition ensures that the majority of the perturbations streamwise variation is attributed to the phase function, thereby justifying the small scaling of the streamwise derivative terms. Finally, the growth rate σ is defined in terms of the disturbance kinetic energy $E = \int_0^\infty (|\hat{u}|^2 + |\hat{v}|^2) dy$, following Juniper *et al.* [57]

$$\sigma = -\alpha_i + \frac{\partial}{\partial x} \ln(\sqrt{E}).$$